

The Geology of the Sideling Range

David Thompson B.Sc



UNIVERSITY OF TASMANIA

A research thesis submitted in partial fulfilment of the requirements for
the degree of Bachelor of Science with Honours.

**School of Earth Sciences
University of Tasmania
November 2000.**

Abstract

The Sideling Range is comprised of Mathinna Group sediments on the western margin of the Scottsdale Batholith. The Sideling Range is situated close to an informally proposed stratigraphic transition within the Mathinna Group that has been documented but not comprehensively mapped or defined. The Sideling Sandstone has been informally proposed as a distinct unit from the underlying Bellingham Formation.

Recent prospecting around the Sideling Range has also revealed a small area of gold mineralisation within a contact aureole, opening the possibility that the gold is related to granite intrusion rather than a typical turbidite hosted mesothermal gold vein style.

This thesis studies the structure and sedimentology of the Sideling Range. It defines the Sideling Sandstone and discusses the proposed stratigraphic transition. It also investigates the nature of the gold mineralising fluid.

The Sideling Range consists of first generation NNW trending folds that conform to the regional structure of the Mathinna Group. Faulting within the Sideling Range is rare and small-scale and post D1 deformation is mainly only evident within the contact aureole.

The Sideling Sandstone unit is approximately 1500 metres thick. It is a fine to medium-grained sandstone that is dominated by thick and massively bedded sandstones that are interlayered with thinner bedded classical turbidites as well as siltstone. The Sideling Sandstone is more thickly bedded than the Bellingham Formation and is from a more proximal environment on the submarine fan. The Sideling Sandstone was deposited in an ancient channel environment.

The study of sulphides within the gold mineralised veins revealed that the fluid, which formed the veins, had a magmatic component.

Acknowledgements

I am greatly appreciative of the support of my supervisor Ron Berry. Thanks Uncle Ron! Thanks also to Russell Fulton for his kind hospitality and help. Life on the farm was unforgettable. I will always remember the lazy call of the crow.

CONTENTS

ABSTRACT	i
ACKNOWLEDGEMENTS	ii
TABLE OF CONTENTS	iii
LIST OF FIGURES	vi
LIST OF PLATES	viii
LIST OF TABLES	viii
LIST OF APPENDICES	viii
 CHAPTER 1: INTRODUCTION	 1
1.0: Initial statement	1
1.1: Aims	3
1.2: Location	3
1.3: Access and exposure	3
1.4: Methods of investigation	4
1.5: Previous studies	4
 CHAPTER 2: REGIONAL GEOLOGY	 5
2.0: Introduction	5
2.1: The Mathinna Group	5
2.2: Granitoid bodies	7
2.3: Structure	9
2.4: Gold mineralisation	10
 CHAPTER 3: STRUCTURAL GEOLOGY	 14
3.0: Structural overview	14
3.1: Methodology	14
3.2: The Sideling Range structural data	17

3.3:	Cross section A-A'	17
3.3.1:	Bedding	17
3.3.2:	Cleavage	17
3.3.3:	Folds	22
3.3.4:	Faults	24
3.4:	Cross section B-B'	26
3.4.1:	Bedding	26
3.4.2:	Cleavage	29
3.4.3:	Folds	29
3.4.4:	Faults	29
3.5:	Cross section C-C'	29
3.5.1:	Bedding	31
3.5.2:	Cleavage	31
3.5.3:	Folds	31
3.6:	Summary of the structure	31
3.7:	Regional correlation of the structure of the Sideling Range	33

CHAPTER 4: MATHINNA GROUP ROCKS OF THE SIDELING RANGE 35

4.0:	Sedimentary overview	35
4.1:	Overview of the present study	35
4.2:	Siltstone	36
4.3:	Siltstone petrology	36
4.4:	The sandstone	39
4.4.1:	Sandstone petrography	39
4.4.2:	Sandstone facies	39
4.4.3:	Sandstone facies 1	41
4.4.4:	Sandstone facies 2	41
4.4.5:	Sandstone facies 3	43
4.5:	Stratigraphy	43
4.6:	Discussion	46
4.7:	Regional comparisons with the Bellingham Formation	48

CHAPTER 5: GOLD MINERALISATION	52
5.0: Previous work	52
5.1: Lithology of the mineralised area	52
5.2: Structure of the mineralised area	52
5.3: Veins	54
5.3.1: Quartz-comb and related intra-vein cross-cutting quartz-sulfide networks	56
5.3.2: Laminated quartz veins	56
5.3.3: Quartz breccia veins	58
5.3.4: Blocky white quartz veins	58
5.4: Paragenesis of the quartz veining and relationship to gold mineralisation	58
5.5: Sulphide chemistry	58
5.6: Summary	62
CHAPTER 6: CONCLUSION	62
REFERENCES	65

LIST OF FIGURES

	Page
Figure 1.1: A geological map of Tasmania	2
Figure 2.0: Generalised geology of NE Tasmania	6
Figure 2.1: The division of Mathinna Group in NE Tasmania	8
Figure 2.2: The proposed stratigraphy of the Mathinna Group of NE Tasmania	8
Figure 2.3: Thrust ramp model for junction between eastern and western Tasmanian terranes	11
Figure 3.0: Regional structural map of the Mathinna Group west of the Scottsdale Batholith	15
Figure 3.1: The Sideling Range surface map	16
Figure 3.2: The Sideling Range structural surface map	18
Figure 3.3 a-f: Stereonet data for the Sideling Range	19
Figure 3.4: Structural cross section A-A'	20
Figure 3.5 a-b: Stereonet data for cross section A-A'	21
Figure 3.6a: Sketch diagram of high angle reverse fault	25
Figure 3.6b: Cross section sketch of anomalous bedding and cleavage zone	25
Figure 3.7: Structural cross section B-B'	27
Figure 3.8 a-f: Stereonet data for cross sections B-B' and C-C'	28
Figure 3.9: Structural cross section C-C'	30
Figure 3.10: Fence diagram combining cross sections A-A', B-B' and C-C'	32

Figure 3.11:	Regional structural map of the Mathinna Group, west of the Scottsdale Batholith	34
Figure 4.0:	Bioturbated siltstone	37
Figure 4.1:	Finely laminated siltstone	37
Figure 4.2a:	Sandstone facies 1b	42
Figure 4.2b:	Sandstone facies 2a	42
Figure 4.2c:	Sandstone facies 2b	42
Figure 4.2d:	Sandstone facies 3	42
Figure 4.3:	A generalised stratigraphy for the Sideling Range	44
Figure 4.4:	A-A' sedimentological cross section	45
Figure 4.6:	A modified regional sedimentological map of the Mathinna Group west of the Scottsdale Batholith	51
Figure 5.0:	Surface map for the gold mineralisation area	53
Figure 5.1a-c:	Stereonet for the gold mineralisation area	55
Figure 5.2:	A cross section for the gold mineralisation area	55
Figure 5.3:	Sketch diagram of a sulphide bearing comb quartz vein	57

LIST OF PLATES

PLATE 1: Photomicrograph of a disjunctive S1 foliation in a fine-grained sandstone	23
PLATE 2: Photomicrograph of cross laminated siltstone	38
PLATE 3: Photomicrograph of bioturbated siltstone	38
PLATE 4: Photomicrograph of sandstone	40
PLATE 5: Photomicrograph of sandstone	40
PLATE 6: Photomicrograph of subhedral pyrite	59
PLATE 7: Photomicrograph of acicular shaped pyrite	59
PLATE 8: Photomicrograph of pyrite and arsenopyrite	59

LIST OF TABLES

TABLE 1: Average trace element composition of pyrite	61
TABLE 2: Average trace element composition of arsenopyrite	61

LIST OF APPENDICES

APPENDIX 1: Literature review: Deep-sea systems: Models, Concepts and Turbidites	
APPENDIX 2: Fact Map of the Sideling Range	
APPENDIX 3: Rock catalogue	

Chapter 1 Introduction

1.0 Initial statement

The northeastern Tasmania terrane consists mainly of the turbiditic Mathinna Group and granitoid intrusive bodies. The Sideling Range is located within this terrane immediately west of the Scottsdale Batholith (Figure 1).

Powell *et al.*, (1993) identified the turbidite units west of the Scottsdale Batholith as part of a northeast prograding submarine fan that developed between the Late Silurian and the Early Devonian. Three distinct and conformable units were proposed, and an upper and fourth unit called the Sideling sandstone was tentatively proposed. It was a tentative proposal because it was based on the study of a small area approximately 10 km southwest of the range, and was difficult to distinguish from the underlying Bellingham Formation. This study of the Mathinna Group closer to the Sideling Range will test the tentative proposal of the Sideling sandstone and provide a more comprehensive definition of the unit.

Marshall (1969) structurally mapped sections of the Sideling Range but a lack of continuous outcrop limited recognition of regional structural elements. Powell and Baillie (1992) identified an upright regional syncline approximately 10 km SW of the range. A northeast traverse and construction of a regional scale cross section up to the Scottsdale Batholith carried out here extends the regional structural information for this area of the Mathinna Group.

Quartz-vein-hosted gold in turbidite deposits is abundant in northeast Tasmania. Recent prospecting around the Sideling Range has uncovered gold bearing veins within the contact aureole adjacent to the western margin of the Scottsdale Batholith, providing an opportunity to study the structural and sedimentological controls of this style of mineralisation, as well as the nature of the mineralising fluid.

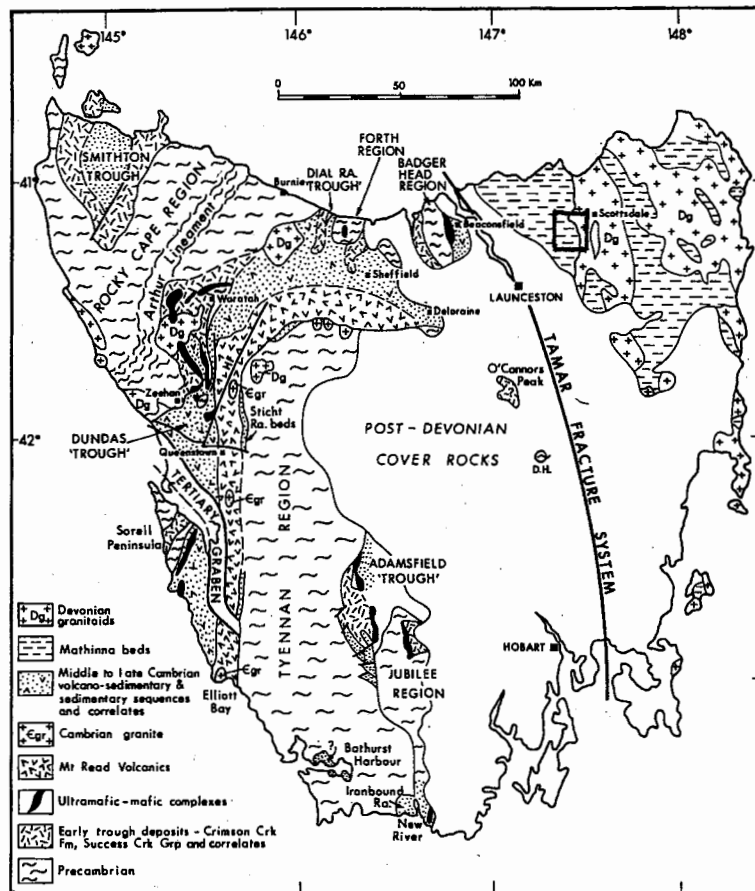


Figure 1. A geological map of Tasmania and the location of the northeastern Tasmanian terrane. The location of the Sideling Range is shown highlighted by the box.

1.1 Aims

The aims of this project were to:

- 1) Map the Sideling Range in order to carry out a structural and sedimentary analysis of the Mathinna Group rocks of the Sideling Range.
- 2) Extend the regional structural information of the Mathinna Group to the Scottsdale Batholith boundary.
- 3) Interpret an environment of deposition and to compare the interpretation with regional studies.
- 4) Carry out a structural and sedimentological analysis of the area of gold mineralisation and correlate this data with vein development and paragenesis.
- 5) Analyse the gold and sulphide bearing veins to determine a likely origin of the gold mineralising fluids.

1.2 Location

The study area is located on the Sideling Range approximately 60 km northeast of Launceston and 10 km west of Scottsdale (Figure 1).

1.3 Access and Exposure

A large area of the Sideling Range has recently been converted from old growth forests into Forestry Tasmania plantations. Access and exposure of outcrop at the Sideling Range is enhanced by the recent creation of new roads to support the expansion of the plantations. The most significant exposure of outcrop occurs along the forestry and farm roads. Creeks in areas of high relief are difficult to access but some have excellent exposure, especially Carins Creek. The plantations and farms rarely have any outcrop.

1.4 Methods of Investigation

The Sideling Range was mapped during 6 weeks of fieldwork. Structural data was written onto enlarged photocopies of the Lisle and Nabowla 1:25000 topographic map. All compass measurements were taken relative to true north.

Thin section analysis was carried out on specimens of different facies and for different parts of each facies sequence. This was carried out in order to identify the mineralogy of the facies as well as to distinguish between siltstone and fine-grained sandstone.

The study of the gold vein deposits was supported by petrographic study and microanalysis of the sulphide phases using the CAMECA 5 x 50 from the CSL, University of Tasmania. These analyses were carried out under the supervision of Dr. David Steele.

1.5 Previous Studies

Banks (1962) categorized the sedimentary rocks of the Sideling Range into an arenite-lutite association. Previous mapping of the Sideling Range was carried out by Marshall (1969) and reported in the Pipers River inch to mile geological survey for the Tasmania Department of Mines.

Gold exploration was previously carried out by Mr. Russell Fulton and Mr. Frank Bardenhagen and is contained in closed file reports at Mineral Resources Tasmania.

Chapter 2 Regional Geology

2.0 Introduction

The northeastern Tasmania terrane consists largely of Mathinna Group sediments underlain by Devonian intrusive and eruptive rocks (Goscombe *et al.*, 1992). These are unconformably overlain by the late Carboniferous to Triassic Parmeener Supergroup which are intruded by thick sheets of Jurassic dolerite (Turner *et al.*, 1986). Areas of Tertiary basalt are scattered throughout the northeast and Tertiary sediments are widespread in lower relief areas. Quaternary alluvium occurs in the river valleys, and on the coastal plains. Major zones of scree occur around the Sideling Range (Marshall 1969; see also Figure 2.0).

2.1 The Mathinna Group

The Mathinna Group is a succession of turbiditic sandstones and mudstones that form the pre-Carboniferous basement to the east of the Tamar Valley, including the Furneaux Group Islands.

Banks (1962) first categorised the Mathinna into two mappable units. These two units were described as a shale with minor sandstone unit and a younger mixed sandstone unit. The boundary of the two units occurs near Golconda, where the mixed sandstone unit outcrops to the east and the older unit to the west.

The age of The Mathinna Group has been constrained by graptolite fossils and fragments of the vascular land plant *Hostimella*. In the Lefroy-Pipers River area, a graptolite suggestive of Early Ordovician age was reported by Banks and Smith (1968), and in several localities within the eastern mixed sandstone unit (Sideling Range and Scamander), fragments of *Hostimella*, indicative of Early Devonian age were found (Cookson 1937 from Burrett and Martin 1989; Banks 1962). Rickards and Banks (1979) discovered a graptolite of Early Devonian age on the east coast at Scamander.

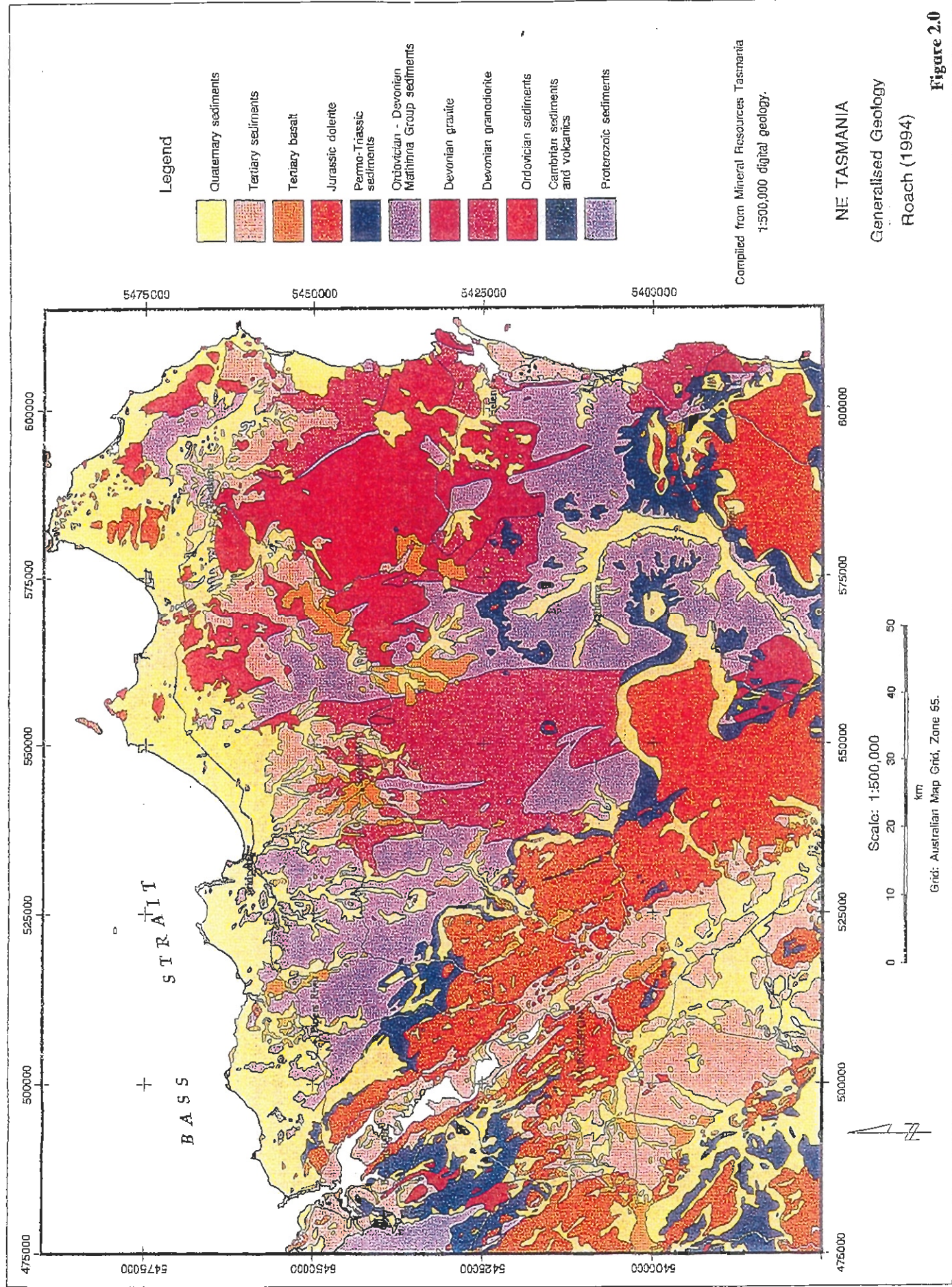


Figure 2.0

Grid: Australian Map Grid, Zone 55.

The lack of Silurian rocks and structural evidence suggested the possibility of an angular unconformity between the two units (Corbett and Martin 1989). Turner (1980) proposed a fault between the Ordovician and Siluro-Devonian age units.

Powell and Baillie (1992) mapped a structural profile between Bridport and Georgetown and the conformity of structure and the transitional nature of the sedimentological units lead them to conclude that the succession was conformable (Powell *et al.*, 1993). This meant that the Mathinna Group was probably the result of 100 million years of deposition via turbidity currents from the western margin of the eastern Tasmania terrane (Powell *et al.*, 1993).

Powell *et al.*, (1993) divided the Mathinna Group west of the Scottsdale batholith into four units (Figure 2.1). The basal unit is the Stony Head Sandstone, estimated to be 1 km thick, consisting of medium to fine grained quartzose sandstone with minor pelite. This unit is overlain by the Turquoise Bluff Slate, a massive black pelite with small proportions of fine sandstone towards the top. The next unit in the stratigraphy is the Bellingham Formation, a mixed pelite dominated unit which comprises classical turbidites of proximal and distal aspect. The fourth unit is the Sideling Sandstone, tentatively delineated by Powell *et al.*, (1993) from the Bellingham Formation by virtue of its greater proportions of sandstone to siltstone. They recognised Facies C and D type turbidites in this area (Figure 2.2).

The Mathinna Group rocks have been regionally metamorphosed to Prehnite-pumpellyite grade except around the contact aureoles created by Devonian granitoid intrusion where the grade is higher (Pattison *et al.*, in press 2000).

2.2 Granitoid Bodies

In Eastern Tasmania during the Late Devonian (398–356Ma), numerous granite-granodiorite batholiths were intruded and at the same time the St. Marys porphyrite was extruded (Goscombe *et al.*, 1992). The granitoid bodies occupy an area of 2500 km² and form the Scottsdale, Blue Tier and Eddystone Batholiths with a number of disconnected lesser bodies to the south (Mc Clenaghan 1989). Thin contact aureoles, typically 1-2 km wide were developed within the Mathinna Group and are mapped as

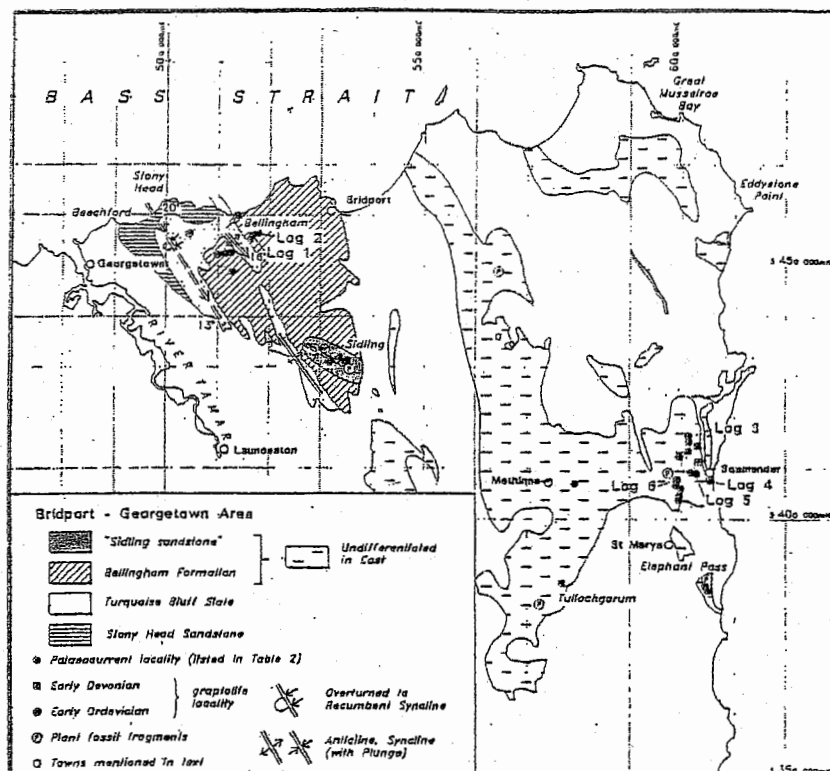


Figure 2.1. The division of the Mathinna Group of NE Tasmania into 4 units by Powell *et al.* (1993)

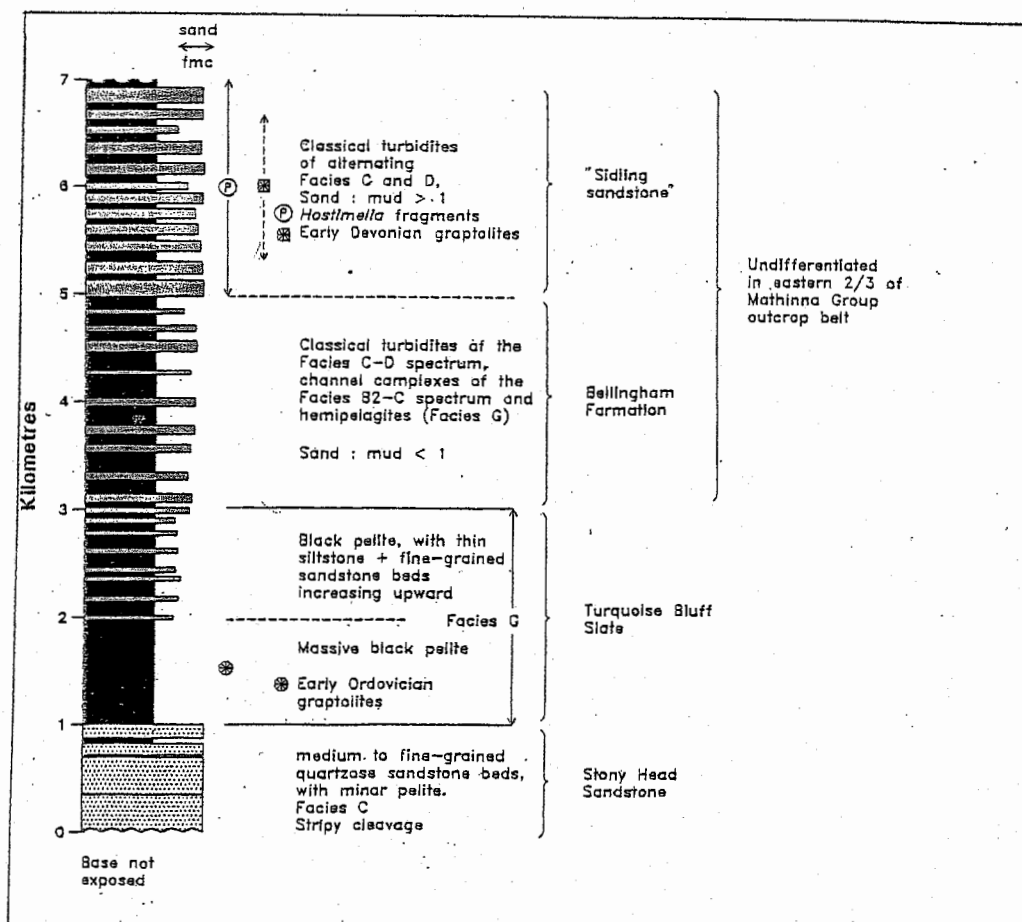


Figure 2.2. The proposed stratigraphy of the Mathinna Group of NE Tasmania by Powell *et al.* (1993).

the limit of spotting within the pelitic units (Goscombe *et. al.*, 1992). Typical assemblages in the aureoles are cordierite-muscovite-biotite quartz-K-feldspar-ilmenite-rutile \pm plagioclase \pm andalusite (Goscombe *et. al.*, 1993).

The granitoids are divided into four main types: granodiorite, biotite adamellite/granite, alkali feldspar granite and biotite-garnet cordierite adamellite (Mc Clenaghan 1989).

Emplacement of the granitoids generally took place at shallow crustal levels (3.15-4.55 km; Scottsdale Batholith) although variability in emplacement depth has been documented with the Pyengana Granodiorite estimated to have been emplaced between 13 \pm 2 kms depth (Varne and Fulton 1994).

Evidence suggests that the granitoid bodies have been emplaced by passive rather than forceful intrusion (Gee and Groves 1971). Some local folding is associated with the Blue Tier Batholith and intrusion of the Scottsdale Batholith at Bridport (Drown 1984). Regional doming of the Mathinna Group is indicated by near vertical axial surface of the folds near the western margin of the Scottsdale batholith (Gee and Groves 1971).

2.3 Structure

The Mathinna Group has been deformed by one main generation of generally NNW trending folds attributed to the Tabberabberan Orogeny (Powell and Baillie 1992).

The age of the folding is constrained to the Early Devonian by the St Marys porphyrite, which postdates the F₁ folds and is dated to be 388 \pm 1 Ma (Turner *et al.*, 1986), and an Early Devonian graptolite found at Scamander (Rickards and Banks 1979).

The F₁ generation of folding is tight to close in profile (Powell and Baillie 1992), generally asymmetric with long planar limbs, tight closures and steeply southwest dipping axial surfaces that imply vergence to the northeast (Williams *et. al.*, 1989). The F₁ folding created a penetrative axial planar cleavage in the pelites and a variably

developed spaced cleavage in the psammites that is evident throughout northeast Tasmania (Powell and Baillie 1992). Crustal shortening during D_1 was in the order of 30-50% (Goscombe *et. al.*, 1993)

A second regional deformation event in NE Tasmania (D_2), that postdates the granodiorite intrusion has been recognised in the Lefroy-Pipers River area by Powell and Baillie (1992) and also Reed (1998). In this area the first generation folds have a recumbent orientation. Powell and Baillie (1992) concluded that the F_1 folds had been reorientated to their recumbent attitude by a regional WSW-directed thrusting event (D_2) that had rotated the Pipers River region over a thrust ramp of Precambrian basement during the Middle Devonian age (Figure 2.3).

Reed (1998) disagrees and suggests that the recumbent folds are a result of a locally emergent D_1 thrust zone and that the D_2 deformation produced only a tightening of the F_1 folds. Reed (1998) suggests that the D_2 event is responsible for the majority of thrust faulting within the Eastern Tasmania terrane.

A regional D_3 mega kinking event has been identified from the analysis of the S_1 cleavage trends in the Mathinna Group by Goscombe *et. al.* (1993). They identified mega-scale kink-bands and kink folds where the strike of bedding changes orientation over a series of defined domains. The kink bands overprint minerals in the contact aureole of the Scottsdale Batholith and pre-date deposition of the Parmeener Supergroup.

2.4 Gold mineralisation

Lode-style mesothermal gold mineralisation in northeastern Tasmania occurs predominantly in quartz-sulphide veins (Keele 1994). In most cases the mineralisation is hosted by a cyclic mixed sandstone and shale succession transitional between sandstone dominated and shale dominated rocks (Reed 1998). The majority of the deposits are largely confined to the 80 km long and 2 km wide Mathinna-Alberton "gold corridor" between the Scottsdale and Blue Tier Batholiths (Keele 1994; see also Figure 2.4).

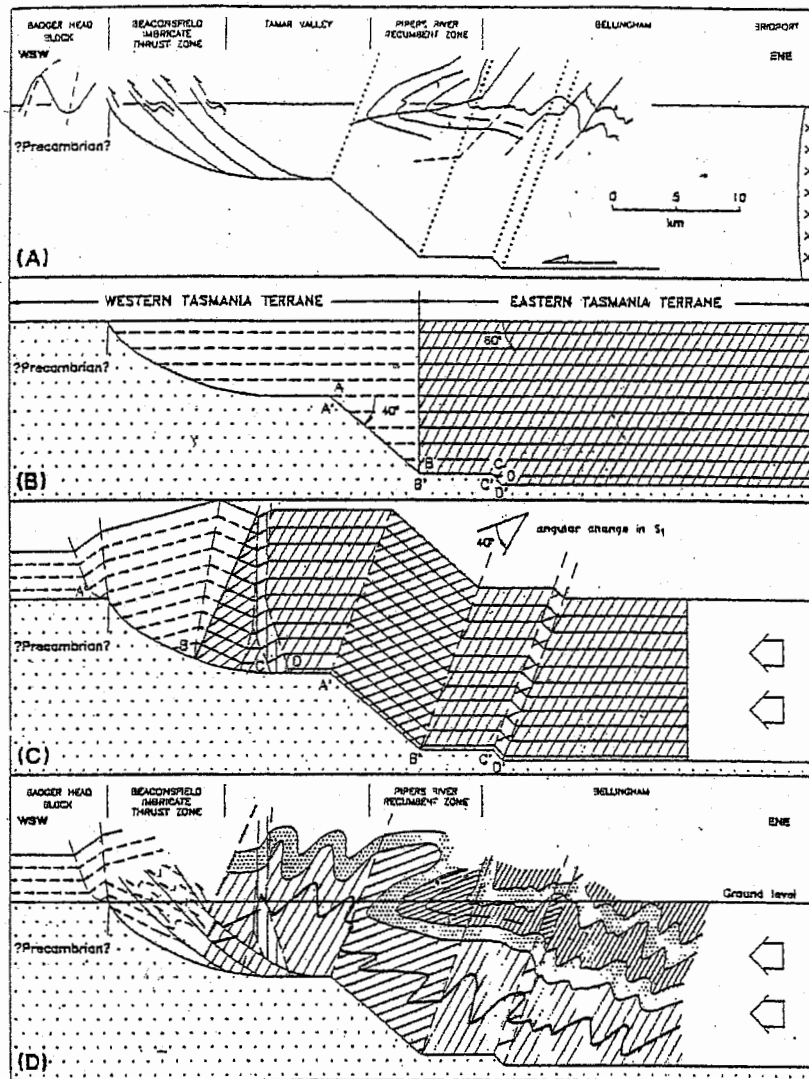


Figure 2.3. Thrust ramp model for the junction between the Eastern and western tasmania terranes (from Powell and Baillie, 1992). (A) Surface constraints on model. (B) Simplified geometry prior to movement. Lines inclined at 60° represent the pre-D₂ thrusting attitude of F₁ axial surfaces in the Eastern Tasmania terrane. (C) Geometry after 25 km of southwestward thrusting, assuming fault-bend folding above the sole thrust. (D) Structure of the Mathinna group based on the model. (from Tectonics, Structure and Ore Deposits, 1998).

Close folding, faulting, a strongly developed cleavage and several generations of quartz veining are associated with the zone of mineralisation (Roach 1994), suggesting it is structurally controlled. Taheri and Findlay (1992) associated the lodes of the gold corridor with a series of NNW trending dextral strike-slip faults and Reed (1998) concluded that the gold mineralisation occupies D₂ structures that are predominantly thrust faults.

Gold has also been found as quartz veins within the roof of the Lisle granodiorite around Lisle, Golconda and Panama and as veins and disseminations within the surrounding contact metamorphosed sediments (Marshall 1969).

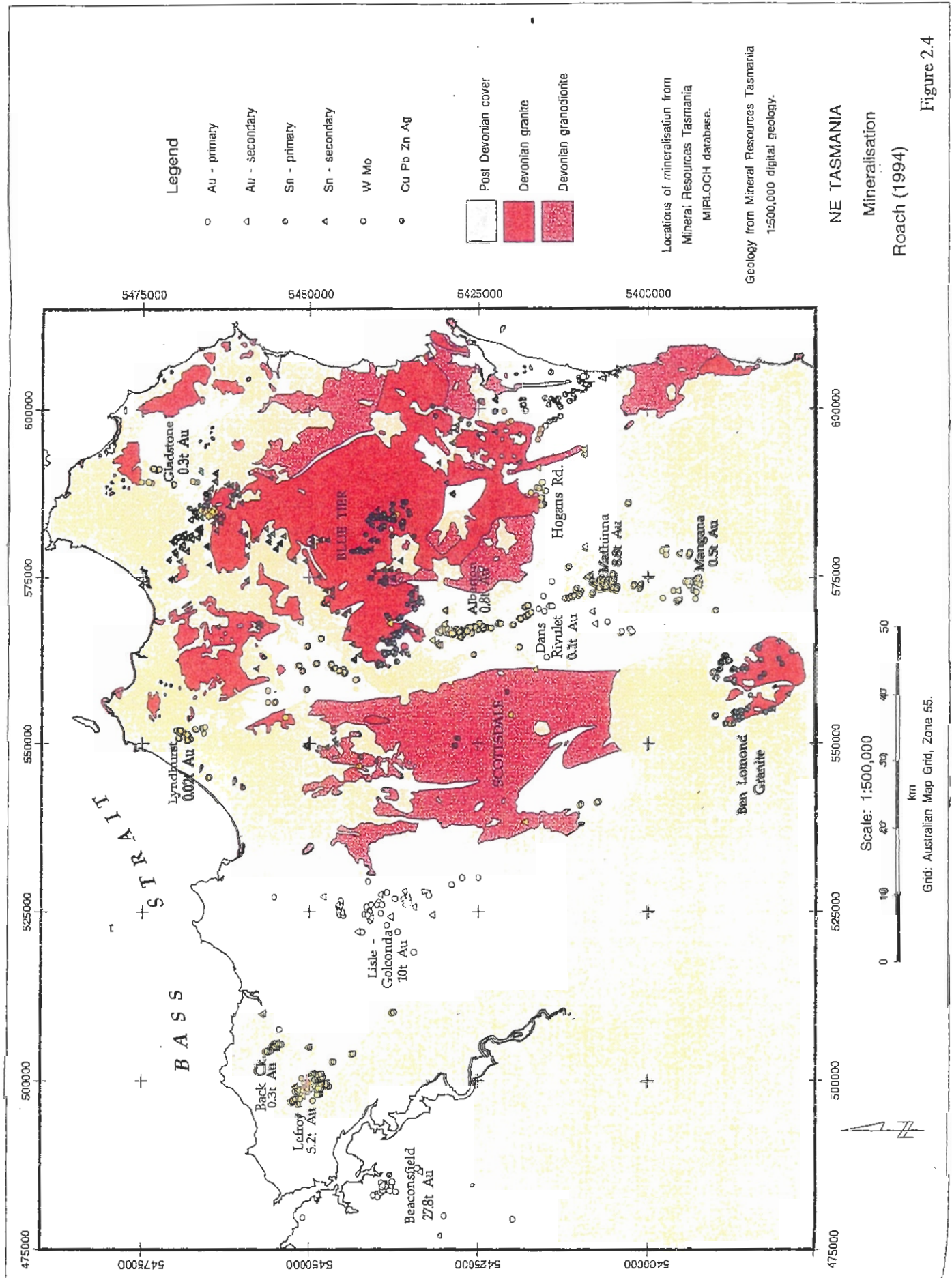


Figure 2.4

Chapter 3 Structural Geology

3.0 Structural Overview

In the Lefroy-Pipers River area, 30 kilometres to the west of the Sideling Range, first generation folds are recumbent or overturned with very gentle axial surface dips. Further to the east, away from the recumbent zone the folds become more upright (Powell and Baillie 1992). Immediately to the southwest of the range is a horizontally plunging and upright regional syncline composed of the Sideling sandstone with a poorly developed cleavage (Powell and Baillie 1992; Figure 3.0).

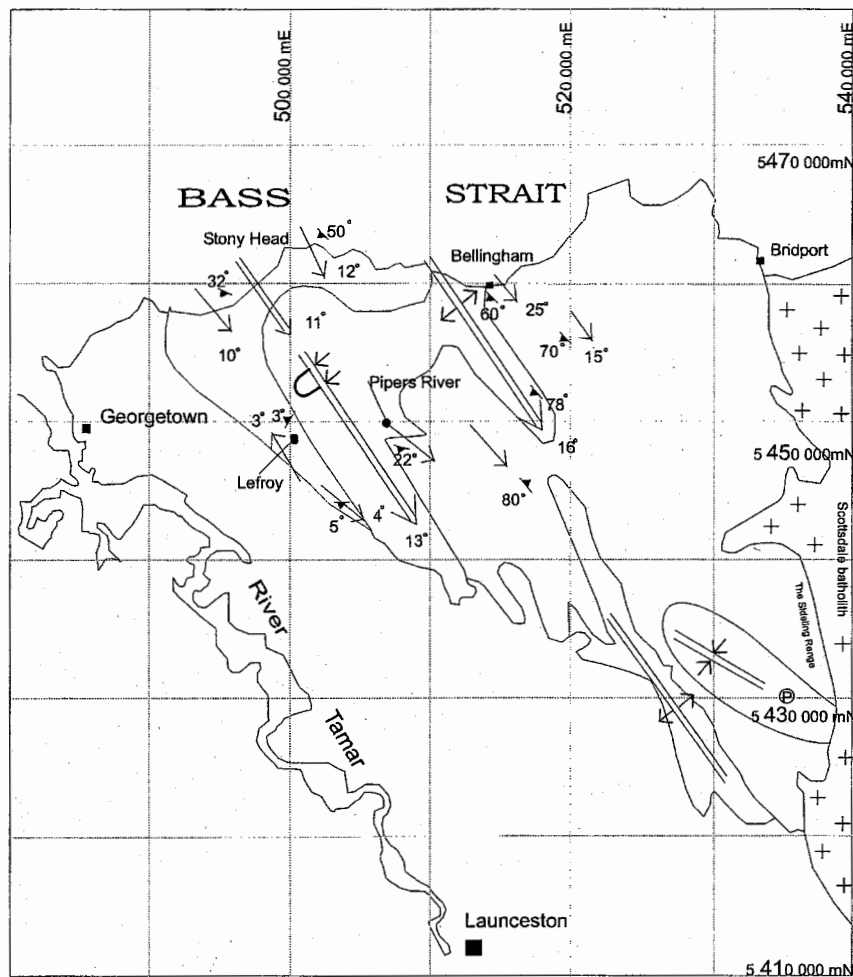
The Sideling Range consists of NNW trending folds composed of Mathinna Group sediments and a granite batholith that envelopes the range on two sides and outcrops along its eastern and northern boundaries (Figure 3.1). A contact aureole defined by spotted Mathinna Group sediments lies to the west of the granite. The aureole has a maximum width of 3 kilometres.

3.1 Methodology

Structural data has been collected to reconstruct cross sections of the Sideling Range. The data has been compiled from road cuttings as well as gully and creek traverses. Two limitations were apparent during the mapping. Only one fold closure was recognised directly in the outcrop and repetition of similar sedimentary units without any recognisable marker beds or sequences made structural correlation difficult. Therefore the folding style has been inferred from changes in the dip of bedding, cleavage orientations and vergence and sedimentary facing indicators.

Three cross sections have been constructed perpendicular to the regional NW-SE trend of the folds. The cross sections were constructed using down-plunge projections where data points were projected along the fold axis to the cross section from their topographic location and most data was projected less than 1500 metres to the relevant section.

Structural geology of the Mathinna Group West of the Scottsdale Batholith.



(Powell and Baillie 1992)

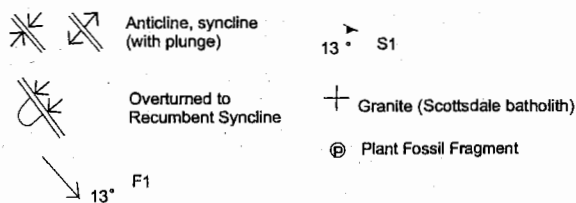
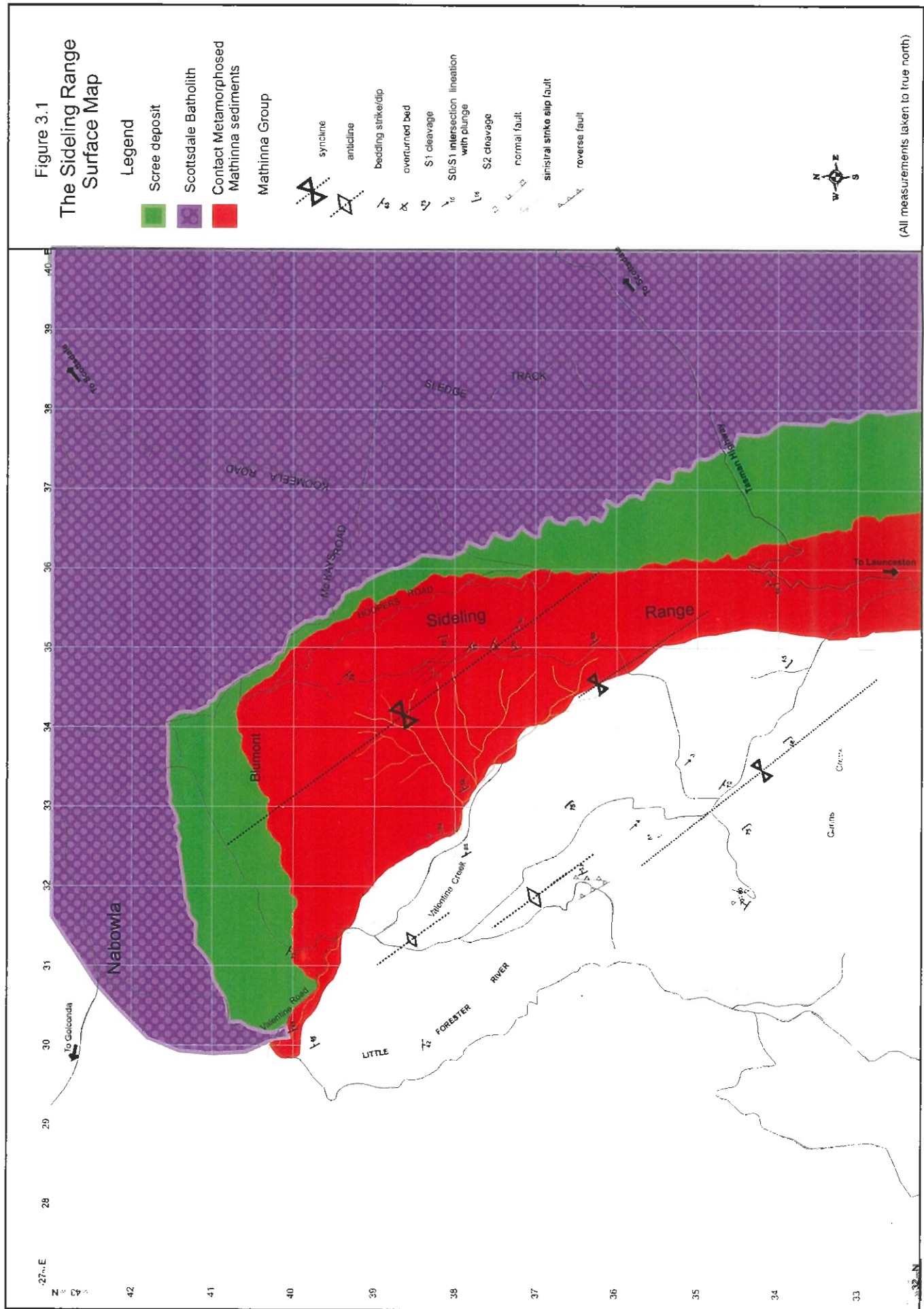


Figure 3.0: Regional structural map of the Mathinna Group, west of the Scottsdale Batholith. Compiled from various sources including Gee and Legge (1974), Jennings (1967), Longman et al. (1964), Longman (1966), Marshall et al. (1965), Marshall (1969), Williams (1976) and Powell and Baillie (1992).



3.2 The Sideling Range Structural Data

The structural surface map indicates that the Sideling Range is dominated by one main generation of F_1 folds that plunge gently NNW or SSE (Figure 3.2 & Figure 3.3 e). The folds are close to open in profile and the average orientation of bedding on the limbs is $131/62^\circ$ SW and $328/56^\circ$ NE (Figures 3.3 a. & b). The F_1 folds have a fine and continuous axial planar cleavage that is evident throughout the siltstone and a spaced and disjunctive cleavage that is rarely found within the sandstone (Figure 3.3 c). A second generation of deformation is only weakly evident, expressed by rare and small-scale faulting that strikes subparallel to the fold trend (Figure 3.3 f), and an S_2 crenulating cleavage observed only within the contact aureole (Figure 3.3 d).

3.3 Cross Section A-A'

Cross section A-A' cuts through the heart of the Sideling Range with the most continuous outcrop along a seven kilometre transect across the regional folding trend (Figure 3.4). Outcrop along A-A' ranges from interbedded sandstone and siltstone in the south-west to spotted hornfels in the contact aureole to the north-east.

3.3.1 Bedding

Bedding is easily recognised within the sandstone units, and sedimentary structures also preserved within the spotted hornfels provide stratigraphic facing of the units. Grading, cross laminations and tool marks were the typical sedimentary structures from which facing could be inferred. The average orientation of bedding on the limbs outside the contact aureole is $131/61^\circ$ SW and $326/62^\circ$ NE (Figure 3.5 a). Within the aureole the average limb orientation is $139/69^\circ$ SW and $325/73^\circ$ NE indicating tightening of the folds and a small rotation in fold trend (Figure 3.5 b).

3.3.2 Cleavage

A fine continuous S_1 foliation is developed within the siltstone beds and in the silty tops of the sandstone beds (using the classification scheme of Twiss and Moore 1992;

Figure 3.2
The Sideling Range
Structural Surface Map

Legend

- Scottsdale Batholith
- Mathinna Group
- Contact aureole boundary

- synclines (large, small)
- anticlines (large, small)
- bedding strike/dip
- overturned bed
- S1 cleavage
- S0/S1 intersection lineation with plunge
- S2 cleavage
- normal fault
- sinistral strike slip fault
- sinistral strike slip shear zone
- reversel fault
- Cross Section



(All measurements taken to true north)



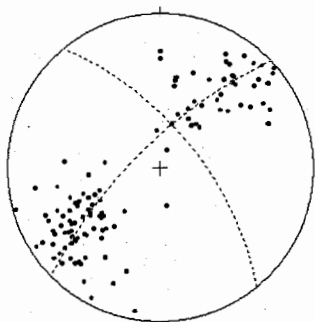


Figure 3.3 a. Poles to bedding orientations;
Sideling Range.

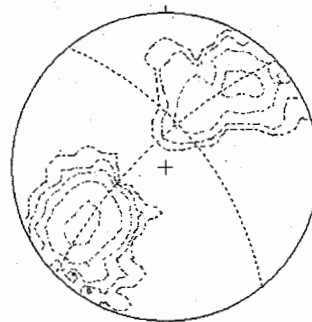


Figure 3.3 b. Density plot for poles to
bedding orientations; Sideling Range.

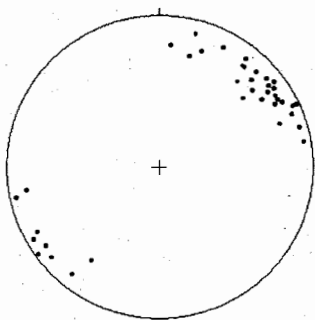


Figure 3.3 c. Poles to S1 cleavage orientations;
Sideling Range.

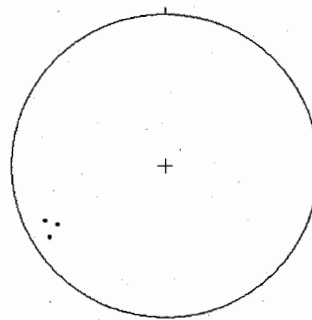


Figure 3.3 d. Poles to S2 cleavage
orientations; Sideling Range.

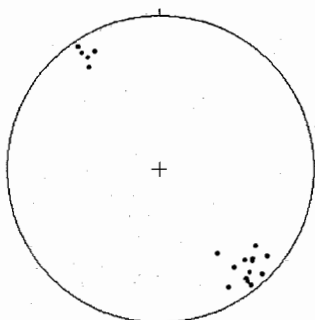


Figure 3.3 e. S0/S1 intersection lineations;
Sideling Range.

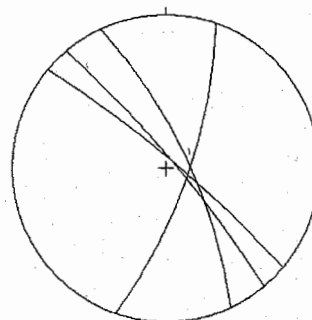


Figure 3.3 f. Planes of reverse dip-slip
faults.; Sideling Range.

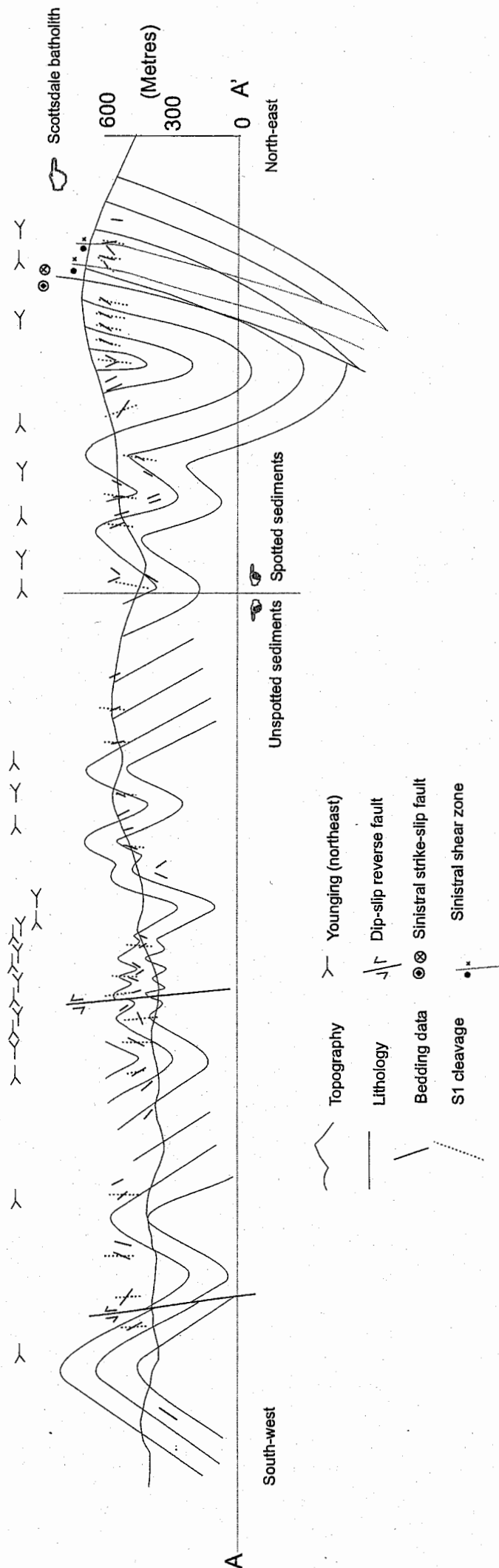


Figure 3.4: Structural Cross Section A-A'. A south-west to north-east trending cross section constructed perpendicular to the regional fold axis and without vertical exaggeration. Cross Section A-A' cuts through the heart of the Siding Range and outcrop ranges from interbedded sands and silts in the south-west to spotted hornfels in the contact aureole to the north-east. The Scottsdale batholith outcrops outside the northeastern boundary of the cross section.

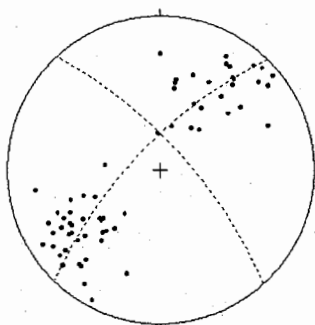


Figure 3.5a: Poles to bedding orientations *outside* contact aureole of Cross Section A-A'.

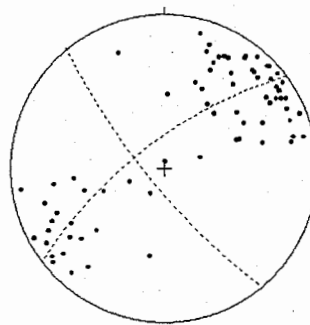


Figure 3.5b: Poles to bedding orientations *inside* contact aureole; Cross Section A-A'.

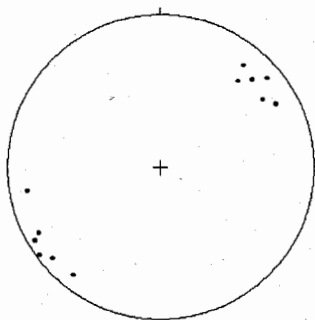


Figure 3.5c: Poles to S1 cleavage orientations Contact aureole of Cross Section A-A'.

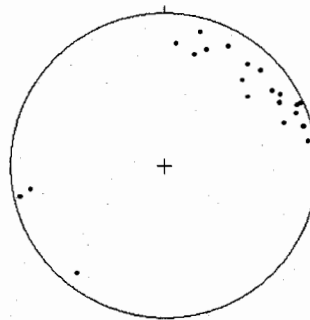


Figure 3.5d : Poles to S1 cleavage *outside* orientations *inside* contact aureole of A-A'.

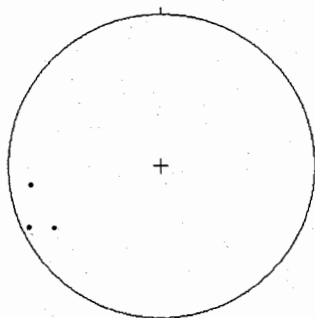


Figure 3.5e : Poles to S2 cleavage orientations; Cross Section A-A'

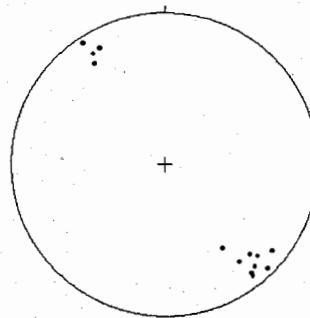


Figure 3.5f : S_0/S_1 intersection lineations; Cross Section A-A'.

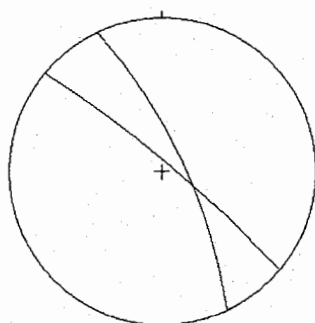


Figure 3.5g: Dip slip reverse fault planes; Cross Section A-A'

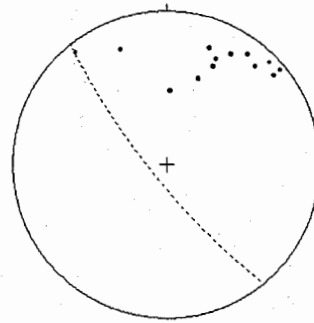


Figure 3.5h : Anomalous zone poles to S_0 orientations and sinistral strike-slip fault. Plane with quartz lineation $6 \rightarrow 321^\circ$.

Figure 3.5 c). No cleavage within the coarser grained sandstone was evident in outcrop although a spaced disjunctive foliation was visible under the microscope (Plate 1). The cleavage strikes SE and is subvertical to NE and SW dipping (Figure 3.5 c). The orientation of S1 cleavage is more variable within the aureole (Figure 3.5 d). Refraction of cleavage displaying increasing divergence towards the top of the beds is common. Bedding and cleavage intersection lineations are subparallel to the calculated regional fold axis suggesting that the cleavage is axial planar to the folds.

A second spaced foliation (S2) that crenulates the S1 cleavage was recorded in the contact aureole in three locations where the outcrop was fresh. The crenulation cleavage dips steeply to the north-east (3.5 e).

3.3.3 Folds

Only one fold closure within the area covered by A-A' is exposed. It is an open syncline consisting of thickly bedded sandstone. Bedding-cleavage intersection lineations on the north-east-facing limb of the fold plunge gently to the north-west whereas intersection lineations on the opposite limb plunge gently to the south-east. Subsequent readings revealed that the majority of bedding-cleavage readings on the majority of the limbs plunge gently to the south-east (Figure 3.5 f).

Outside of the aureole the interlimb angle of the folds has a range between 70° and 110°, whereas inside the aureole the folds are tighter with angles between 46° and 80° (Figures 3.5 a & 3.5 b). The statistically defined axial plunge of the regional fold outside the aureole has a horizontal to gentle plunge of 0°–14° towards 134° (Figure 3.5 a). Within the aureole the regional plunge is 15° towards 144° (Figure 3.5 b). This data indicates a strain difference between the folds inside and outside the contact aureole. However this strain variation has not been identified in the cleavage data.

Although only one fold closure within the area covered by A-A' is exposed, the bedding and cleavage data is consistent and enables accurate classification and description of the folds. The folds in the area covered by A-A' can be classified as cylindrical to slightly non-cylindrical, close to open and upright with similar,

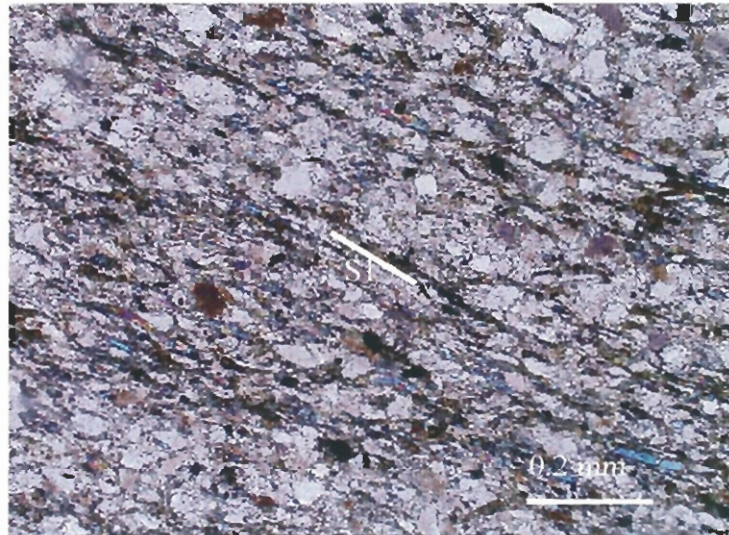


Plate 1. A spaced disjunctive S1 foliation in a fine-grained sandstone. White mica and oxides define the cleavage. Sample D.T 14. with X-Nicols

symmetrical to slightly asymmetrical fold profiles (using the classification schemes of Parks 1983). The folds have planar limbs and rounded hinges. (Figure 3.4).

3.3.4 Faults

A lack of good marker beds made recognition of faults and measurement of fault displacement very difficult.

Two high angle north-east-facing reverse dip slip fault zones were recorded on this section of the Sideling Range. Both fault zones consisted of an array of fault splays within which the bedding and cleavage had experienced a significant amount of deflection. Sense of shear was determined from the drag of the cleavage. One fault occurred on the north-east-facing limb of a syncline striking 310° and dipping 85° NE (Figure 3.5 g & 3.6 a). Displacement was probably not large because there is no significant lithological change across the fault. The second reverse dip slip fault was on the south-west-facing limb of a syncline striking 335° and dipping 75° NE (Figure 3.5 g). Near both of these faults the dip of the cleavage changed from its usually steep south-west dip to a steep north-east dip.

A strike slip fault with quartz slickenfibres consistent with a sinistral displacement occurs within the hornfels unit on the south-west-facing limb of the large eastern syncline. The fault is parallel to bedding along the plane $321/81^\circ$ SW and the striations plunge $6 \rightarrow 321^\circ$ (Figure 3.5 h). This provides some evidence that bedding planes were reactivated as slip surfaces in some areas.

Ten metres north of this fault, bedding and S1 cleavages are anomalous to the typical strike and dip of the beds on the limb. Anti-clockwise strike rotations of between 30° – 90° and slightly shallower bedding dips to the south and south-west occur for approximately 15 metres (Figure 3.5 h). The bedding orientation then returns to its typical NW strike and dips steeply and slightly overturns for approximately forty metres before a recurrence of the anomalous beds for approximately ten metres (Figure 3.6 b).

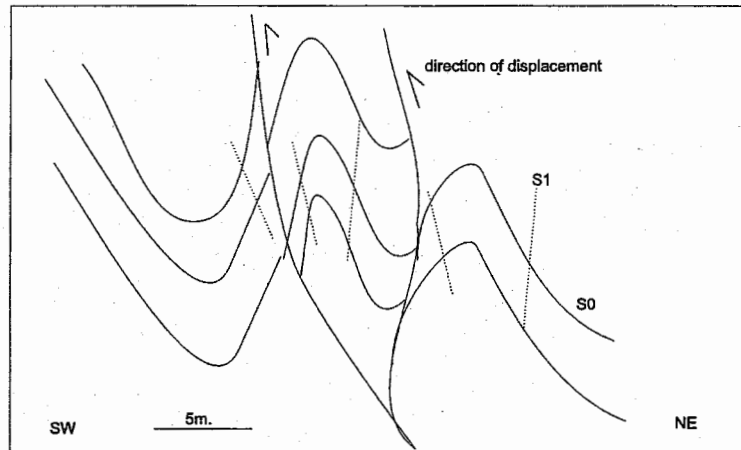


Figure 3.6a: Sketch diagram of high angle reverse fault within the northeast facing limb of a syncline. Bedding and cleavage displacement occurs around discrete and anastomosing fractures within the sandstone.

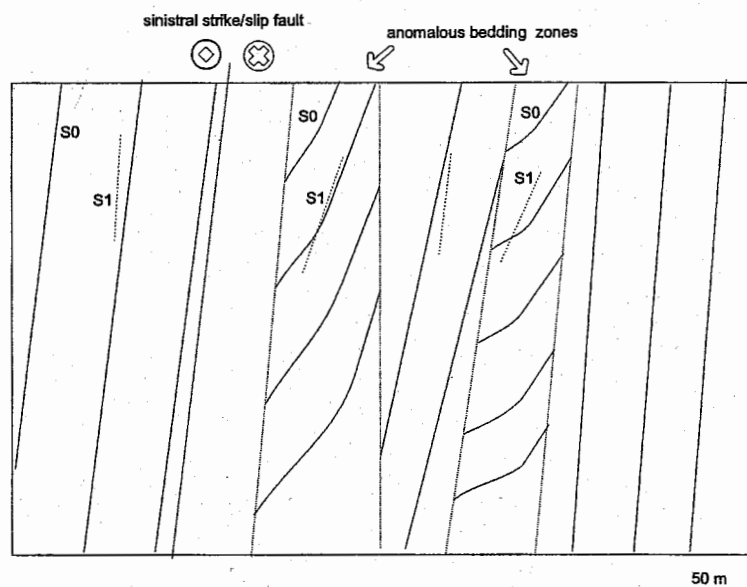


Figure 3.6 b. Cross Section sketch of sinistral strike/slip and anomalous bedding and S1 cleavage zone.

3.4 Cross Section B-B'

Cross section B-B' incorporates data from the northwestern section of the Sideling Range where the topography is lower and outcrop is limited to the side of the range (Figure 3.7).

3.4.1 Bedding

Bedding along the section covered by B-B' consists mainly of homogenous fine-grained grey siltstone interlayered with thin beds of laminated siltstone and sandstone. The thickness and dip direction of the bedding is very difficult to define from the siltstone, and only very close inspection of the rock-face and identification of small-scale sedimentary features enabled dip directions and sedimentary facing to be determined. The facing indicators used were small-scale slumps in the siltstone, cross laminations and grading within the sandstone beds.

The average orientation of the regional limbs is 330/48° NE and 125/51° SW (Figure 3.8 a) corresponding to an average interlimb angle of 84°. The north-east facing limbs are dominant as shown by the poles to bedding distribution with the south-west facing limbs having a shorter length and cropping out over a smaller area.

3.4.2 Cleavage

A fine continuous S1 foliation is developed within the siltstone but was not so well developed within the sandstone and parallel laminated siltstone beds. Cleavage generally dips steeply southwest with an average orientation of 140/77° SW (Figure 3.8 b). The only north-east dipping cleavages recorded were within close proximity to a fault zone. Bedding and cleavage intersection lineations are sub-parallel to the calculated regional fold axis suggesting that the cleavage is axial planar to the folds (Figure 3.8 c).

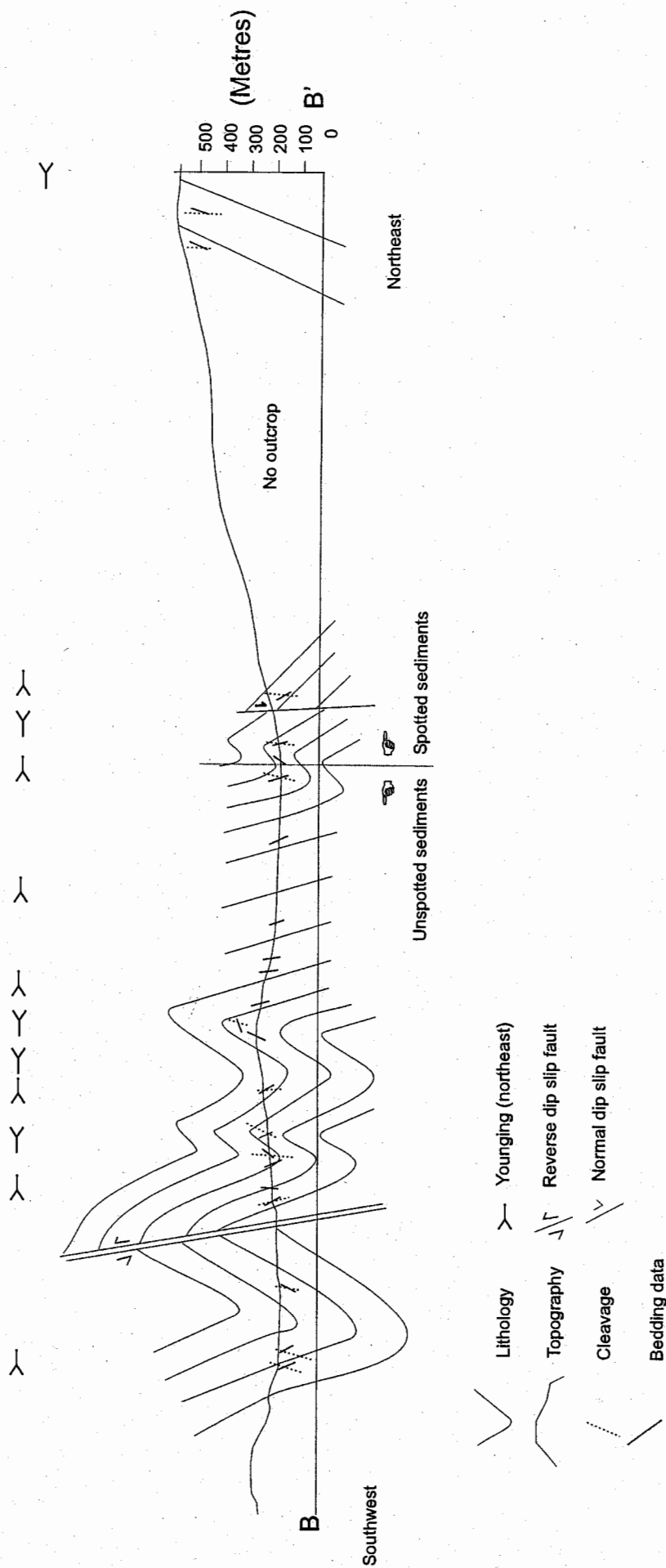


Figure 3.7: Structural Cross Section B-B'. A south-west to north-east trending cross section constructed perpendicular to the regional fold axis without vertical exaggeration. Cross Section B-B' runs from the lower relief southwestern side of the range and into Blumont Mountain. Outcrop along B-B' consists largely of siltstone in the south-east, and spotted hornfels to the north-east.

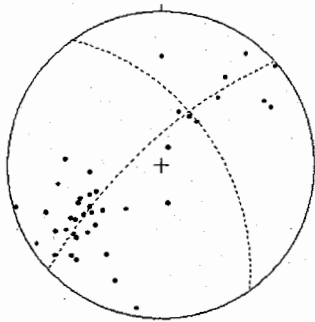


Figure 3.8a: Poles to bedding orientations;
Cross Section B-B'.

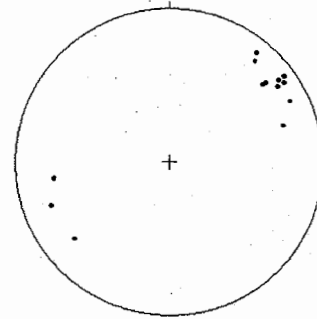


Figure 3.8b: Poles to cleavage orientation;
Cross Section B-B'.

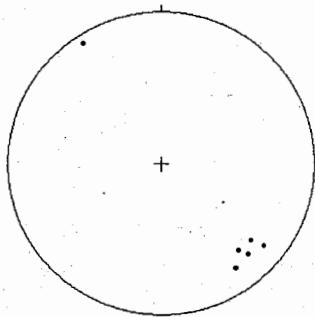


Figure 3.8c: S_0/S_1 intersection lineations;
Cross Section B-B'.

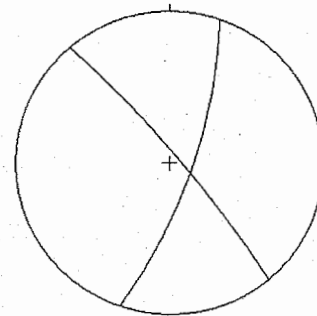


Figure 3.8d: Reverse dip-slip fault
planes on Cross Section B-B'.

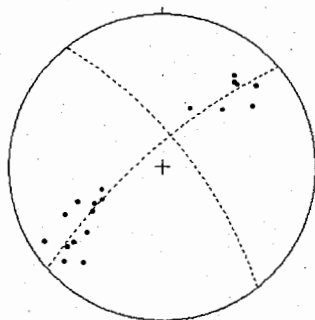


Figure 3.8e: Poles to bedding orientations;
Cross Section C-C'.

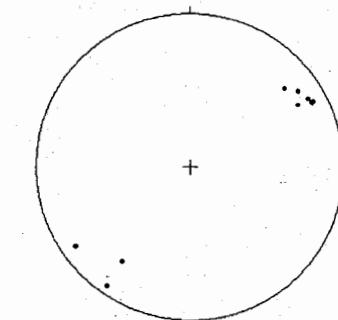


Figure 3.8f: Poles to cleavage orientations;
Cross Section C-C'.

A spaced and disjunctive north-east dipping crenulation cleavage is developed locally within the spotted hornfels.

3.4.3 Folds

Folds within the B-B' cross section are open, upright and cylindrical with a similar fold profile and long planar limbs. No fold closures were exposed, but bedding cleavage lineations have a consistent south-east plunge parallel to the statistically defined plunge of the regional fold axis (13→137; Figure 3.8a & 3.8c). The average fold wavelength is two to three hundred metres.

3.4.4 Faults

One normal dip slip fault and two high angle reverse dip slip faults were identified. The two reverse faults were 40 metres across strike from each other, sub-parallel to the NW–SE striking bedding, and steeply east dipping (Figure 3.8 d). The array of fault splays and bedding and S1 cleavage drag on either side of the fault planes indicated a reverse sense of movement. The amount of displacement on each of these faults was probably not significant as no noticeable change in lithology on either side of the faults occurred.

The normal dip slip fault is located on the western edge of the contact aureole striking parallel to the bedding and dipping 85° to the east. The displacement direction was inferred from the drag on bedding but is unlikely to be large.

3.5 Cross Section C-C'

Outcrop along the C-C' line was not continuous and therefore the northeastern half of the reconstruction has been largely extrapolated from data used for the A-A' cross section (Figure 3.9).

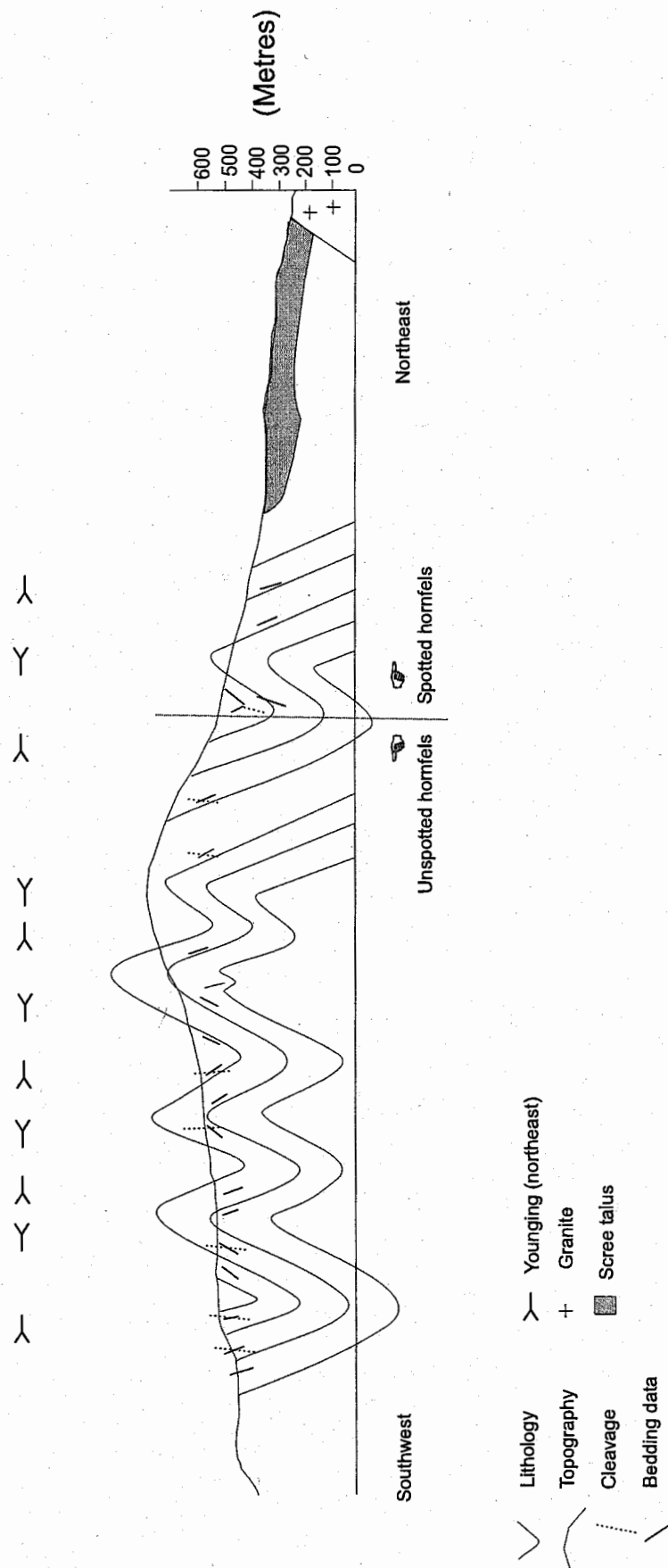


Figure 3.9: Structural Cross Section C-C'. A south-west to north-east trending cross section constructed perpendicular to the regional fold axis and without vertical exaggeration. Cross Section C-C' displays folds from the high relief southeastern side of the study area. Lithologies consist of sandstones fining upwards to siltstones. Spotted hornfels occur to the north-east of the section. A wide talus scree apron covers the granite-sediment contact to the north-east.

3.5.1 Bedding

Outcrop was well exposed along Carins Creek. The north-east-facing limb of the first syncline found from the left in the cross section revealed clear evidence of beds thinning and fining upwards. The beds were two – four metre Facies 1a sandstones that thinned gradually into 10 cm mud and silt beds. Stratigraphic facing was determined by fining upwards of individual beds

3.5.2 Cleavage

Cleavage was evident in the siltstone beds as a fine and continuous foliation consistently striking NW–SE and variably dipping steeply southwest or northeast (Figure 3.8 f).

3.5.3 Folds

The folds have an average wavelength of two hundred metres, average limb orientations are 330/50° NE and 325/46° SW, and a southeast plunging fold axis 12°→139° (Figure 3.8e). Folds are open and similar in style, with symmetric planar limbs and rounded hinges.

3.6 Summary of the Structure

The folds of the Sideling Range trend NNW and are slightly non-cylindrical, although a gentle south-east plunge is predominant. The folds are dominantly SW verging away from a large syncline that is evident close to the granite-sediment boundary.

The positions of major folds appear to correlate between cross sections indicating lateral continuity over six kilometres parallel to the regional folding trend. Smaller folds less than 50 metres wavelength die out over short distances (Figure 3.10).

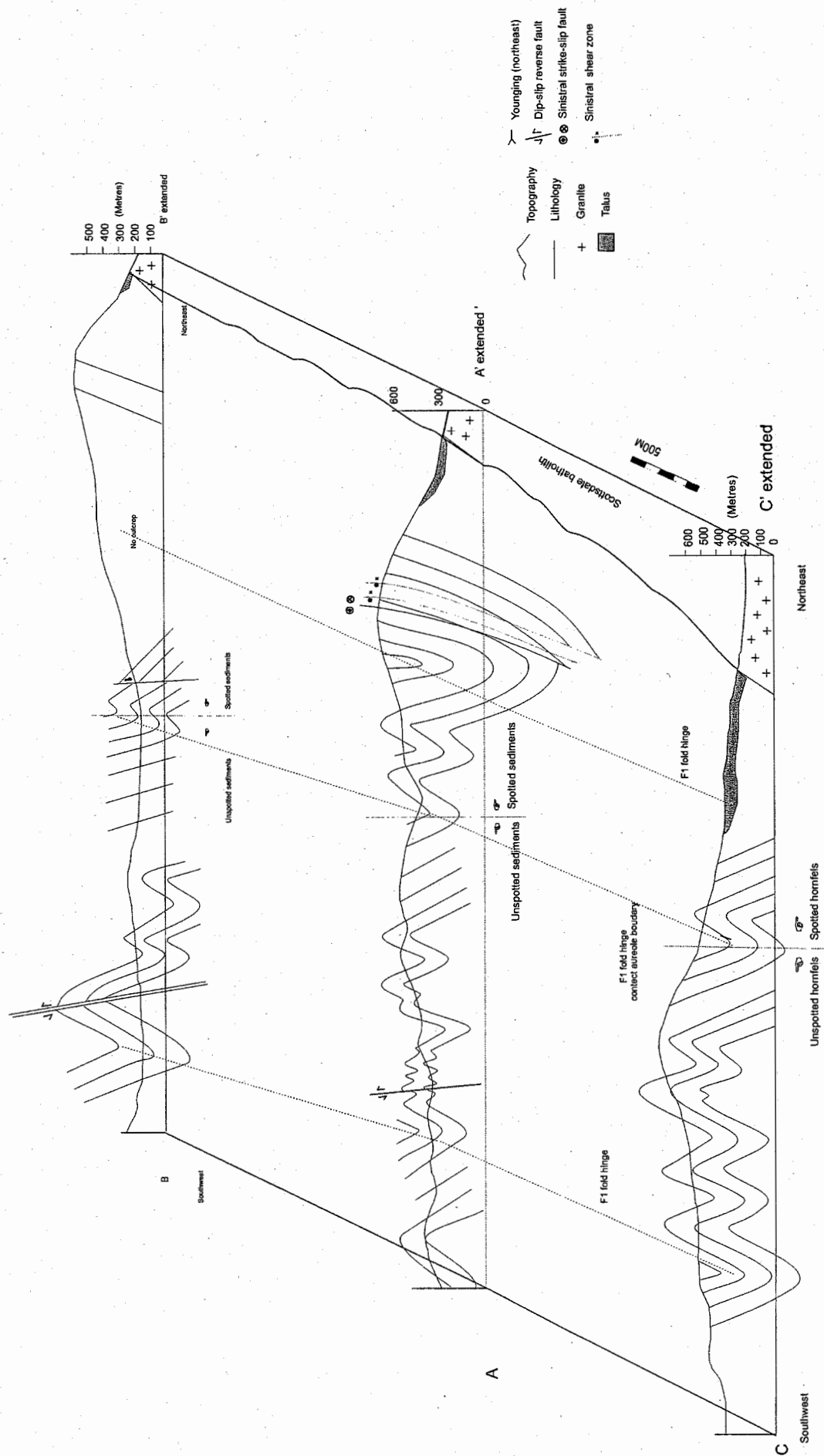


Figure 3.10: A fence diagram combining the structure of the three cross sections up to and across the Scottsdale Batholith boundary. The diagram illustrates the continuity of the folds along the regional folding trend.

A fine and continuous S1 axial planar cleavage is present within the finer grained siltstone but largely absent from the majority of the sandstone, and a second crenulating cleavage was evident in a few locations within the aureole.

Bedding within the contact aureole is slightly steeper and the strike of bedding appears rotated 10° clockwise in comparison to bedding outside of the aureole. Folds within the aureole are also tighter. The spatial evidence suggests that the tightening and rotation could be due to the granite intrusion. A sinistral strike-slip fault and associated shear zone within the aureole provide some evidence of a post D1 deformation that has caused brittle as well as ductile deformation.

Faulting is small scale, mainly reverse dip-slip and occurs close to the fold hinges and striking sub-parallel to the strike of bedding. The deflection of the bedding and cleavage within the fault zones also provides some evidence of post-D1 deformation outside of the aureole, although this is very tentative.

3.7 Regional Correlation of the Structure of the Sideling Range

Bedding and folding trends for the Sideling Range trend NNW and are conformable with bedding and folding data for the Mathinna Group to the west and south-west of the study area (McClenaghan, Calver 1994). Powell and Baillie (1992) mapped a regional syncline with an anomalous fold trend of 120° between the Sideling Range and the southwestern margin of the Mathinna Group (Figure 3.0). Further investigation of previous mapping from Longman et al., (1964) and McClenaghan and Calver (1994) indicate that this fold is unlikely.

Figure 3.11 shows a representation of the compiled regional bedding and cleavage information (McClenaghan and Calver 1994) including measurements compiled from this study. Small scale folding is apparent and the majority of the bedding readings dip to the north-east with no anomalous bedding strikes apparent.

This data along with a general younging direction to the north-east indicates that the large scale structure across the area may be the NE dipping regional scale limb of a syncline. I have tentatively recognised the large syncline identified in this study as

the hinge of the regional syncline. Further work to the north of the Sideling Range however is needed to further define the regional scale folding.

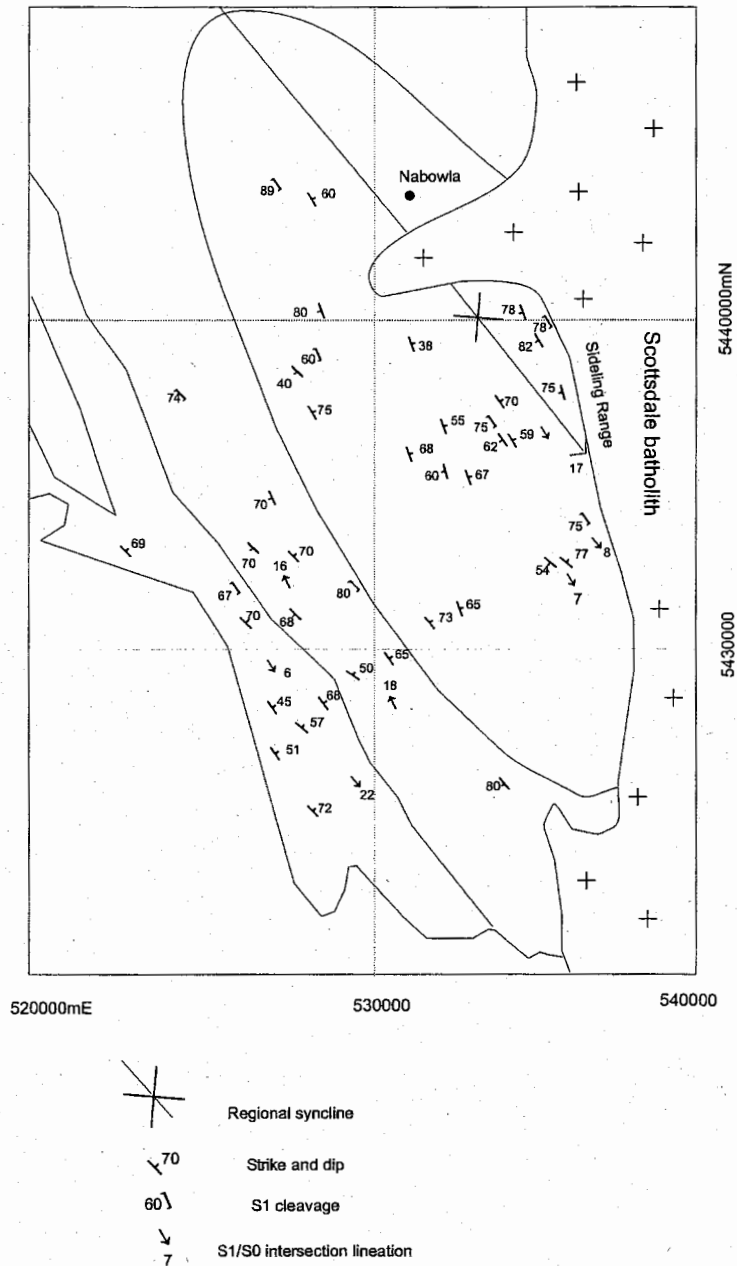


Figure 3.11: Regional structural map of the Mathinna Group, west of the Scottsdale Batholith. Compiled by McClenaghan and Calver (1994) from sources including Gee and Legge (1974), Jennings (1967), Longman et al. (1964), Longman (1966), Marshall et al. (1965), Marshall (1969), Williams (1976) with additions from Thompson (2000).

Chapter 4 Mathinna Group Rocks of the Sideling Range

4.0 Sedimentary Overview

Banks (1962) has previously described the Sideling Range sedimentary rocks as a mixed sandstone and shale succession indicative of deep-sea turbidites. Marshall (1969) described the sediments as part of an arenaceous sequence comprising siltstone, impure sandstone with quartzite and minor intercalations of slate.

More recently Powell et al. (1993) mapped the Sideling Range sedimentary rocks into a thin to thick-bedded succession of classical turbidites with a dominant sandstone composition of quartzose sublitharenite. The succession is comprised of a lower section, the Bellingham Formation and an upper section called the Sideling Sandstone. Drown (1984) previously logged a section within the lower succession on the Bellingham coast and found it to comprise thin bedded classical turbidites. Mapping from Powell et al. (1993) slightly to the south-east of Bellingham extended Drown's work and found that the formation also comprises minor amounts of massive thick-bedded sandstones and hemipelagites. Palaeocurrents measured in the Bellingham Formation indicate that the depositional environment consists of lobes on a submarine fan prograding to the north-east (Powell et al. 1993).

The Sideling Sandstone is distinguished from the Bellingham Formation by the increased amounts of massive sandstone (Powell et al. 1993). The map of Powell et al. (1993) includes the Sideling Range as part of the Bellingham Formation (Figure 2.1).

4.1 Overview of the present study

The sedimentary rocks of the Sideling Range comprise interlayered fine-grained sandstone and siltstone and their metamorphic equivalents in the contact aureole. Sandstone and siltstone commonly occur together within the same bed, for example a graded bed with a base comprised of sandstone grades upwards into siltstone. A

bedform such as this is described as sandstone whereas a bedform that has only silt sized particles and no sand sized particles is categorised as a siltstone unit

4.2 Siltstone

The siltstone occurs either as a continuous unit with thin interlayerings of sandstone estimated at one point to be almost two hundred metres thick or as thinner units interlayered within the sandstone and no more than forty metres thick as a unit.

The siltstone is a dark to light grey colour and very hard when fresh. On the weathered surface of the rock it is blue, purple or a yellowish-brown colour. Greater than 60% of the siltstone on the Sideling Range has no discernible sedimentary structures occurring as large undifferentiated sections in which bedding is difficult to define. Bioturbation is apparent in some of the siltstone as dark grey wispy planes and spots hosted by a lighter grey siltstone (Figure 4.0). Small scale slump folds and cross laminations are evident but not very common (Plate 2). A distinguishing feature of the siltstone is the presence of a fine continuous cleavage (terminology as classified by Twiss and Moores 1992).

Finely laminated siltstones with black, green and infrequent white planar and parallel laminations 0.1-0.5 cm thick occur in beds up to ten metres thick either on their own or interlayered with bioturbated siltstone (Figure 4.1).

4.3 Siltstone Petrography

In thin section the siltstone is dominated by a fine-grained micaceous matrix consisting of white mica that has an average grain size of 0.01 mm width (Plate 3). The micas are aligned along a bedding plane and a cleavage plane. The dominant framework mineral is quartz that has a maximum size of approximately 0.02 mm and displays undulose extinction and serrated and irregular grain margins. Clastic muscovite (0.4mm), subhedral feldspar (0.02mm) and prismatic tourmaline (0.1-0.5 mm) also occur as framework grains in very minor proportions. The framework minerals occupy between 5-10% of the siltstone and appear embedded within the

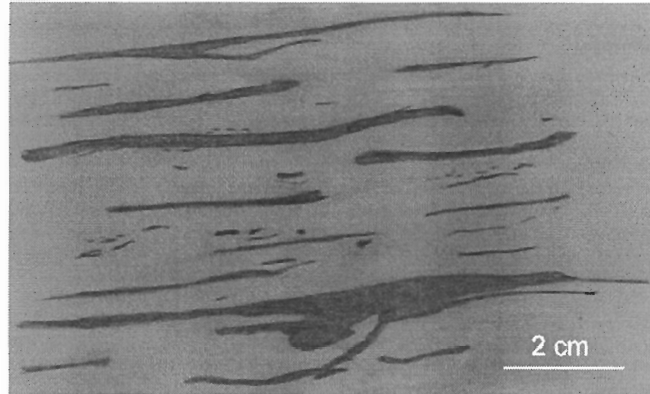


Figure 4.0: Bioturbated siltstone. Dark grey wispy planes of siltstone and spots hosted by a lighter grey siltstone that weathers to a purple or blueish colour. Specimen 2a.

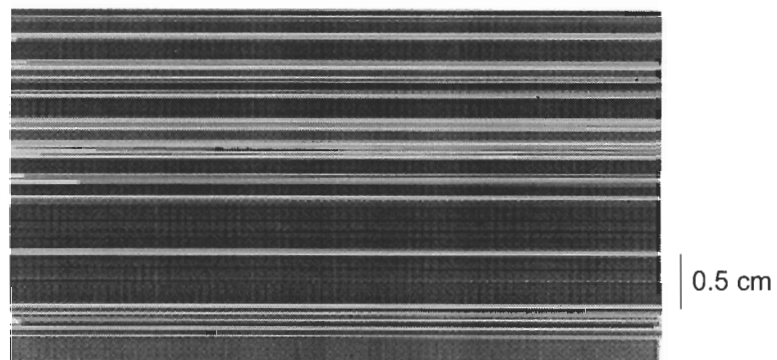


Figure 4.1: Finely laminated siltstone. Consists of black, green and infrequent white planar and parallel laminations 0.1-0.2 cm thick. Specimen D.T 20

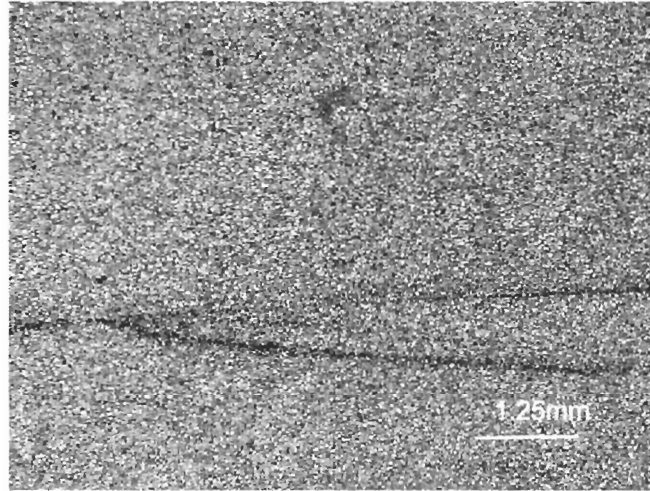


Plate 2: X- nicols photomicrograph of a cross laminated siltstone. Mineralogy consists of a fine-grained matrix of white mica with framework minerals of quartz, feldspar and tourmaline. Accessory minerals of zircon, apatite, and oxides are also preset. Specimen D.T 1.

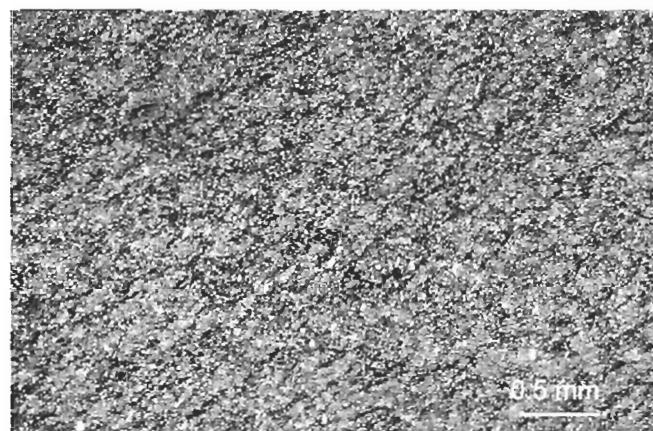


Plate 3: Photomicrograph of bioturbated siltstone. Consists of a strongly aligned and fine-grained micaceous matrix with small proportions of framework minerals of quartz, muscovite, feldspar and tourmaline. Accessory mineralsof zircon, apatite and oxides are also present. Specimen 2b.

micaceous matrix. Accessory minerals of zircon, apatite and opaques also occur within the siltstone.

4.4 The Sandstone

4.4.1 Sandstone Petrography

In thin section the sandstone typically consists of quartz and other framework grains in an argillaceous matrix. The ratio of framework minerals ranges from 70-90% of the sandstone. Poorly sorted angular to subangular quartz is the dominant framework mineral and the majority of the quartz is monocrystalline with small amounts of polycrystalline quartz clasts (chert). Quartz grains can be as fine as 0.05 mm and are usually no coarser than 0.5 mm (Plate 4 and 5). Where grading is defined by quartz grains in thin section the boundary is quite sharp. The quartz displays undulose extinction and pressure solution effects where quartz grain boundaries touch. Highly irregular grain margins of quartz are common against the argillaceous matrix.

Other framework minerals identified in the sandstone which occur in lesser proportions are clastic muscovite (0.08-0.2mm), rectangular shaped plagioclase feldspar (0.01mm), irregular shaped tourmaline (0.6mm) and chlorite (0.05 mm). The abundance of these minerals can vary between sandstones. Clastic muscovite is more prevalent within the finer grained sandstone (10% of the framework minerals), and plagioclase feldspar is more abundant within the coarser grained sandstones (5% of framework minerals). Accessory proportions of iron oxides, zircon (0.2 mm) and rutile are also present.

Therefore the Sideling sandstones can be classified as medium to fine-grained, poorly sorted and texturally immature. They are defined as a quartz greywacke to greywacke after Pettijohns' (1975) classification of sandstones.

4.4.2 Sandstone Facies

The sandstone is divided into three main facies and two sub facies based on the recognition of five distinct units that repeat themselves in cycles throughout the range.

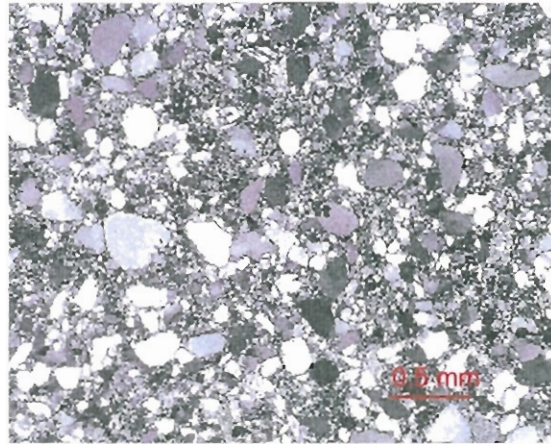


Plate 4: X-nicols photomicrograph of a medium-grained poorly sorted sandstone. The sandstone consists of subangular quartz, clastic muscovite, plagioclase feldspar, chlorite and tourmaline in an argillaceous matrix. Specimen 7 D.T.

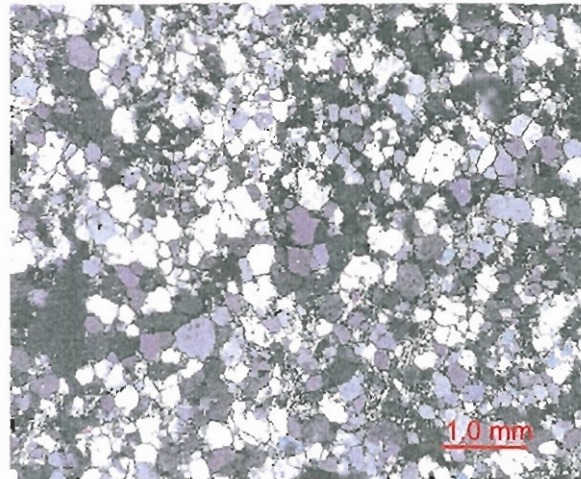


Plate 5: X-nicols photomicrograph of a poorly sorted medium-grained sandstone. The proportion of quartz framework minerals is greater, the sorting more organised and the argillaceous matrix less abundant than specimen 7 D.T of Plate 4. The same minerals are evident as in 7 D.T. Specimen 13 D.T.

The units are distinguished from each other by parameters such as bedding thicknesses, sand to silt ratios and sedimentary structures.

4.4.3 Sandstone Facies 1

The most diagnostic feature of facies 1 is represented by thick, medium to fine grained indurated sandstone beds with barely visible cleavage. They are friable and a yellowish brown colour in the weathered form and a dark to light grey colour when fresh.

Sub-facies 1a consists of 2 -4 metre thick beds of massive and structureless sandstone. It has the coarsest and greatest percentage of quartz grains within the Sideling Range with a maximum quartz grain size of 0.5 mm.

Subfacies 1b (Fig 4.2 a) occurs as 0.3-2 metre thick beds of massive sandstone with thin silty tops (0.5-1 cm.). The contact between the sand and siltstone is sharp and the siltstone has a gently undulating top. The base of the sandstone is also sharp with no visible grading and tool marks are common. The unit has a marked cyclicity with beds thinning upwards and the sand to silt ratio decreasing during each cycle. Each cycle appears to vary in thickness between 150-300 metres.

4.4.4 Sandstone Facies 2

Sandstone Facies 2 corresponds to the classical turbidite as defined by Bouma (1962; See Appendix 1) although it does not contain all the elements of the Bouma sequences. It also corresponds to Facies C as described by Mutti and Ricci Lucchi (1973; See Appendix 1).

Sub-facies 2a (Figure 4.2 b) consists of 0.3-0.4 m thick beds of sandstone and siltstone with Boumas Ta, Tc, Td and Te intervals. The basal unit is a 20-30 cm thick fine-grained sandstone base (Ta) that grades gradually upwards into a 4-5 cm division of fine-grained cross laminations (Tc). This division is truncated by parallel laminations, (Td), of either very fine sand or coarse silt (3-4 cm), overlain by fine dark grey silt that has a gently undulating top. Some beds also contain

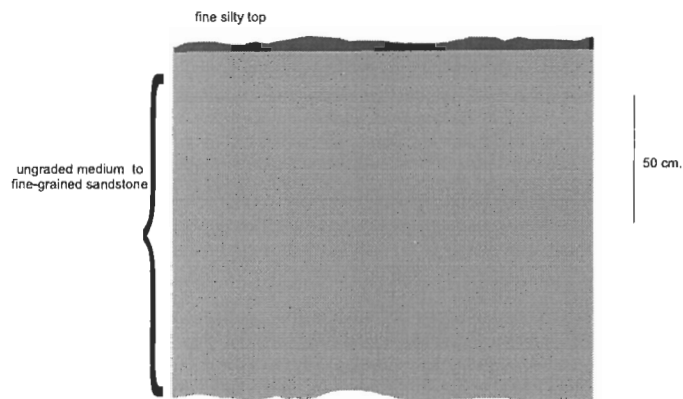


Figure 4.2a : Sandstone Facies 1b.
0.3-2m thick beds of massive sandstone with thin undulating silt tops.

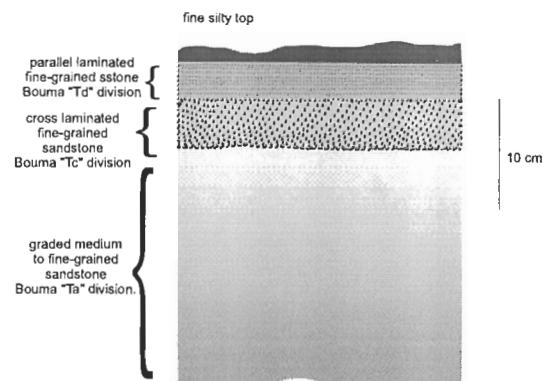


Figure 4.2 b: Sandstone Facies 2a.
0.3-0.4m thick beds of fine to medium grained sandstone (Ta) that grades upwards into 4-5 cm thick cross laminations (Tc) which is truncated by a 3-4 cm division of parallel laminations (Td) and overlain by a thin and gently undulating silt top.

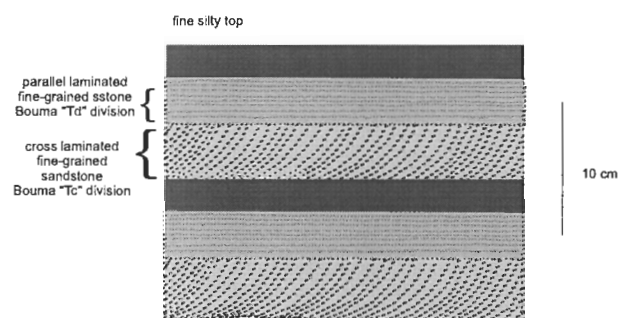


Figure 4.2 c : Sandstone Facies 2b
0.1m thick beds of fine-grained sandstone with cross laminations (4 cm) overlain by a division of planar laminations which is overlain by a dark grey silt top. Note the sharp and planar contacts.

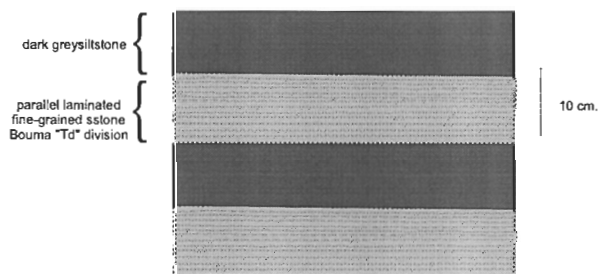


Figure 4.2 d: Sandstone Facies 3.
0.1m thick beds of interlayered fine-grained parallel laminated sandstone and dark grey siltstone.

intraformational rip-up clasts that are flat and elongate bodies probably due to compaction after burial.

Sub-facies 2b (Figure 4.2 c) occurs as 10 cm thick beds of fine-grained sandstone with an average grain size of 0.08 mm and siltstone with Boumas Tc, Td and Te divisions. This facies begins with cross laminations on the base (4 cm) truncated by a layer of fine-grained parallel laminations (4 cm) overlain by a fine dark grey silt top (2 cm). The siltstone has a planar top and contacts between the different layers are sharp.

A marked cyclical pattern of Facies 2 occurs throughout the Sideling Range. The commencement of Sub-facies 2a usually begins after a cycle of Facies 1, and has a thickness between 50-100 metres. The beginning of sub-facies 2b usually starts after the end of cycle 2a with the thickness of each cycle being approximately 30-40 metres

4.4.5 Sandstone Facies 3

This facies has 10 cm thick beds of interlayered fine-grained light grey sandstone and dark grey siltstone. The sandstone often occurs in fine parallel laminations. The contact between the two layers is sharp and grading within either of the layers is rare (Figure 4.2 d). The unit commonly occurs above and below facies 1b, although contacts are never visible. Facies 3 has an average thickness of 10 metres and a maximum thickness of 40 metres. Facies 1b and 3 frequently occur interlayered together throughout the range.

4.5 Stratigraphy

A generalised stratigraphy for the Sideling Range is shown in Figure 4.3. Plotting the observed positions of the facies and their relationships onto a fact map (Appendix 2) and then projecting them onto a structural cross section (Figure 4.4) has produced the stratigraphy. The estimated thickness for the Sideling Range sediments, as calculated from the cross section is 1500 metres.

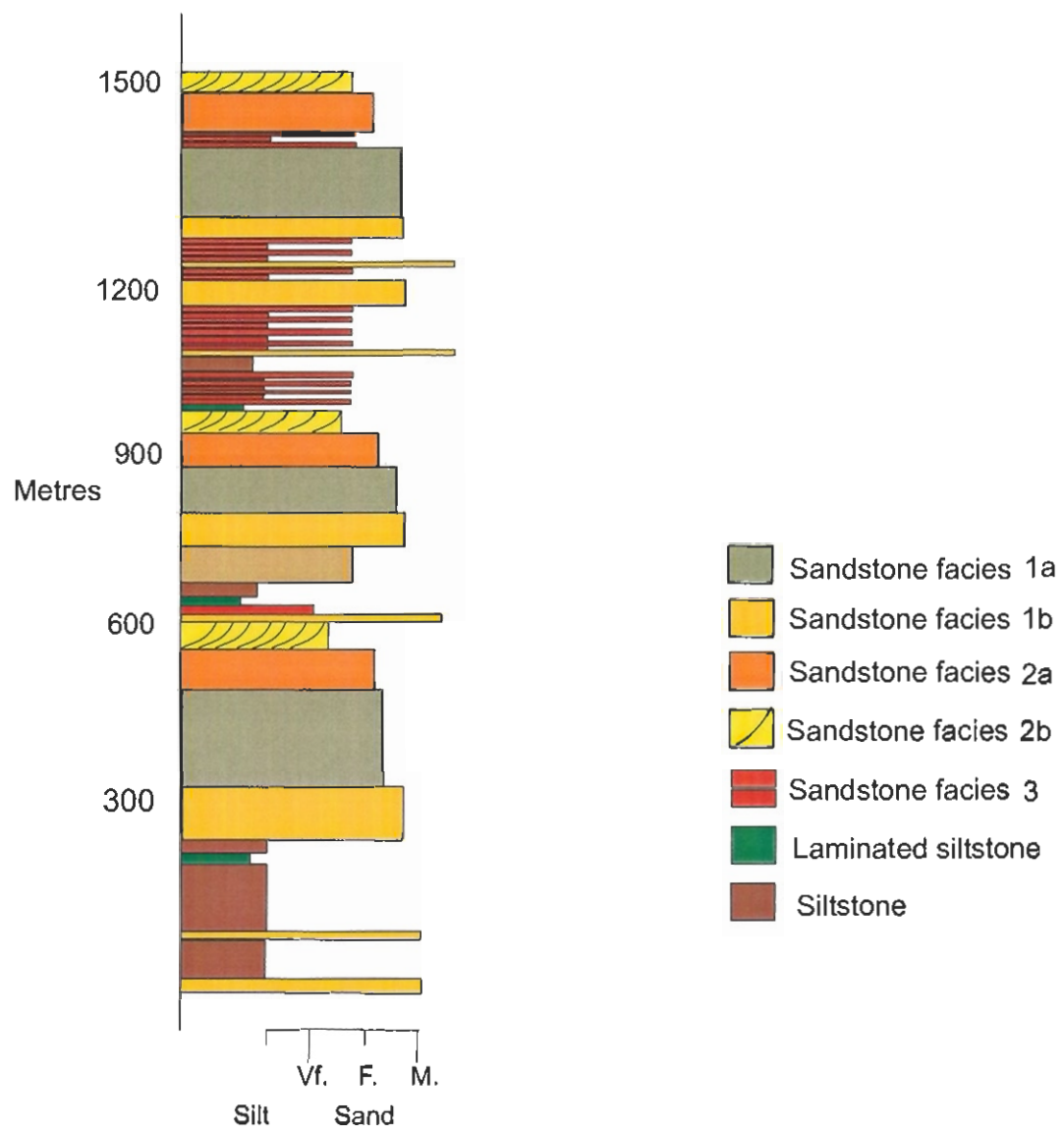


Figure 4.3 : A generalised stratigraphy of the Sideling Range. The stratigraphy shows three thinning and fining upwards cycles of Facies 1 overlain by Facies 2. The intervals consist of variations of siltstone and sandstone. Towards the top of the section siltstone is largely absent from the intervals and Facies 3 and sandstone facies 1a dominate.

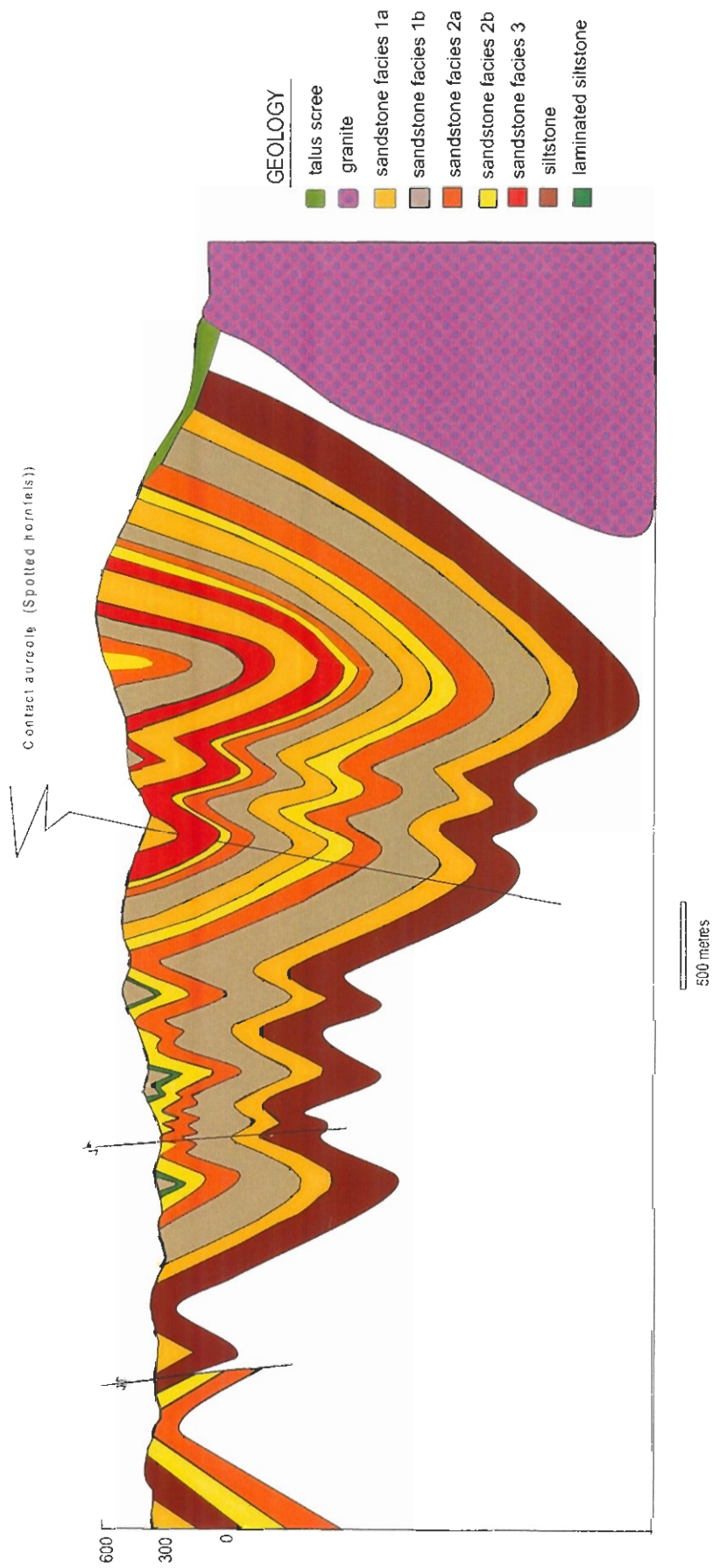


Figure 4.4 : A sedimentological cross section for Cross Section A-A' drawn from field data. The cross section illustrates the cyclical nature of the facies arrangement with sandstone Facies 1a and 1b overlain by Facies 2. This association occurs three times in the cross section and is punctuated by either siltstone or sandstone Facies 1a and 3.

The base of the stratigraphy is a 250 metre thick siltstone that is punctuated by a few fine-grained sandstone beds of Facies 1.

The dominant facies association in the stratigraphy is composed of facies 1 and 2 with beds that thin upwards and also show a decline in the sandstone/siltstone ratio. Minor proportions of siltstone and facies 3 intervals occur infrequently throughout the association.

At the base of the association are the thickest sandstone beds of sub-facies 1a. Sub-facies 1b overly 1a and although the transition is never clearly evident, it appears that the beds around the transition are up to 2 metres thick with silt partings less than 1 cm thick. Further up the section beds of sub-facies 1b thin to less than a metre and the siltstone parting thickens. Clearly evident in outcrop is a transition from sub-facies 1b to the more classic turbidite beds of sandstone facies 2. Sandstone sub-facies 2a is overlain by sub-facies 2b. No transitional features such as bedding thickness changes occur between 2a and 2b and therefore it is assumed that the transition is sharp. The facies association is calculated to be approximately 250 — 350 metres thick and has a marked cyclical pattern throughout the range. Sandstone facies 1 dominates the majority of the association and is between 200 — 250 metres thick.

In between the cycles intervals of interlayered sandstone sub-facies 1a, facies 3 and siltstone occur. The intervals are between 150 — 250 metres thick and towards the top of the stratigraphy thick siltstone beds are absent which indicates an overall coarsening upwards trend throughout the stratigraphy.

4.6 Discussion

The framework grains of the sandstones consist mainly of high quantities of monocrystalline quartz, chert and resistant accessory minerals such as tourmaline, zircon and apatite. The fine grain size, the presence of resistant minerals and minor feldspar and the absence of lithic fragments suggest that the sandstone is mineralogically mature and probably sourced from a recycled sedimentary environment. The large quantity of quartz grains displaying undulose extinction and

the presence of chert in the Sideling sandstones is typical of low-rank metamorphic source rocks (Boggs 1995). The possible tectonic setting for the source rocks based on these mineral compositions is either a continental block or recycled orogen type provenance (terminology as defined by Dickinson *et al.*, 1983). The poorly sorted nature of the quartz grains and the high proportion of matrix is typical for turbidite deposits (Boggs 1995).

The transportation of the sand and siltstone was via several different types of sediment grain flows that deposited the sediment in successive cycles. The siltstone was transported by suspension sedimentation and deposited by a slow settling of the grains. This slow settling probably occurred continuously throughout the depositional life of the succession.

The sandstone was transported either by debris flows or turbidity currents that interrupted the siltstone deposition during periods of increased submarine fan development. A lack of grading within Facies 1 suggests that it was transported either by debris flows or high-density turbidity currents. The graded bedding and cross laminations that define Facies 2 are indicative of turbidity current transport and Facies 3 has tractional as well as suspension sedimentation features that indicate transportation by low-density turbidity currents as well as periods of suspension sedimentation.

The relative position within the fan environment in which the Sideling Range sediments were deposited is difficult to determine because patchy outcrop does not allow large-scale features to be identified. However general observations and the constructed stratigraphy does provide evidence for the nature of the ancient environment (See Appendix 1 for deep-sea fan models and their associated environments).

Absence of any mudstone within the Sideling Range suggests that the depositional environment was proximal to the source (Haines pers comm. 2000). The generalised stratigraphy reveals three thinning and fining upwards sequences and associated intervals that are indicative of channelised sequences and overbank deposits (Mutti and Ricci Lucchi, 1972; Walker 1984). Channel fill sequences display distinct

thinning and fining-upwards cycles as a result of abrupt abandonment of the channel and commonly associated with these sequences are intervals of silt and thin-bedded turbidite sands that accumulate as a result of current overbanking from adjacent active channels (Mutti and Ricci Lucchi 1975).

Other evidence that supports a channelised sequence is the high sand to silt ratio throughout the Sideling, the presence of thick and ungraded sandstone beds and the large proportion of beds with silt partings. However the lack of any visible channels throughout the Sideling Range and the absence of coarse-grained sandstones is problematic.

4.7 Regional Comparisons with the Bellingham Formation

Drown (1984) mapped an arenaceous and argillaceous sequence of rocks at Bellingham and Sandy Point. He defined the sandstone lithology as quartzose subgreywacke and greywacke and the petrographic analysis of the sandstone and siltstones show a mineralogy of poorly sorted quartz in a fine-grained micaceous matrix that is virtually identical to the Sideling Range mineralogy.

Drown (1984) describes the rocks as being of proximal and possibly distal aspect with regards to the submarine fan environment and with a sand to silt ratio of 4.8. He logged a continuous section typical of the arenaceous section and many of the beds are fine-grained classic type turbidites consisting of variations of Bouma divisions Ta-Te. No cyclical patterns are apparent and the bed thicknesses are typically thin, ranging between 0.3-0.5 m.

Powell et al. (1993) logged two continuous sections along Bridport Rd. within the Bellingham Formation. The sections consist of thin siltstone and sandstone couplets interbedded with thin to thick-bedded fine-grained sandstones defined as quartzose sublitharenite. The sandstones consist of a base of fine-grained parallel laminated sandstone that grades upwards into a thin layer of cross laminations. Massive fine-grained sandstone beds appear towards the top of the section with five large beds between two to five metres thick which Powell et al. (1993) interpret as the beginning

of a channelised sequence. The overall sand to silt ratio of the sections is less than one.

The Sideling Range sediments have different bedforms to those described by both Drown (1984) and Powell *et al.*, (1993) although they are mineralogically the same. However the bedding sizes documented by Drown (1984) and Powell *et al.*, (1993) are typically smaller than the beds found in the Sideling Range with lower sand to silt ratios. Facies 2 sandstone at the Sideling Range is similar to the Bellingham sediments but the dominance of thick-bedded massive sandstones at the Sideling Range distinguishes them from the sediments of the Bellingham Formation.

Thinner bedforms are often indicative of a more distal environment (Mutti and Ricci Lucchi 1972). The Bellingham Formation stratigraphically underlies the sandstone of the Sideling Range and the sediments have the same mineralogy. Palaeocurrents measured by Powell *et al.*, (1993) reveal north-east directed currents which is also the general direction of younging. Therefore it can be interpreted that the transition of the Bellingham Formation to the thicker sandstone of the Sideling Range reveals the northeastwards progradation of a submarine fan. This has been suggested by Powell *et al.*, (1993).

Powell *et al.*, (1993) defined the Sideling Sandstone as consisting of massively bedded sandstones and Facies C and D classical turbidites (terminology as defined by Mutti and Ricci Lucchi 1972). The massively bedded sediments (Facies 1a & 1b) are the most abundant bedform of the Sideling Range occurring in bedforms 0.3-4 metres thick. Facies C and D classical turbidites are the equivalent of this reports Facies 2 and 3 sandstones. Therefore the entire area of this study correlates with the Sideling Sandstone and the boundaries created by Powell *et al.*, (1993) need to be extended to include the Sideling Range within the Sideling sandstone unit rather than the Bellingham Formation.

New boundaries have been created for the Sideling Sandstone on Figure 4.6. The boundary is extended to include the Sideling Range. The extension and the shape of the boundary beyond the range is based on the structural information from the previous chapter as well as various sources compiled by Mc Clenaghan and Calver

(1994) that indicates the Sideling Sandstone is exposed within the hinge region of a gently plunging regional syncline. The extension of the boundary is limited in the north-west so that it does not transgress the sandstone shale division of Banks (1962).

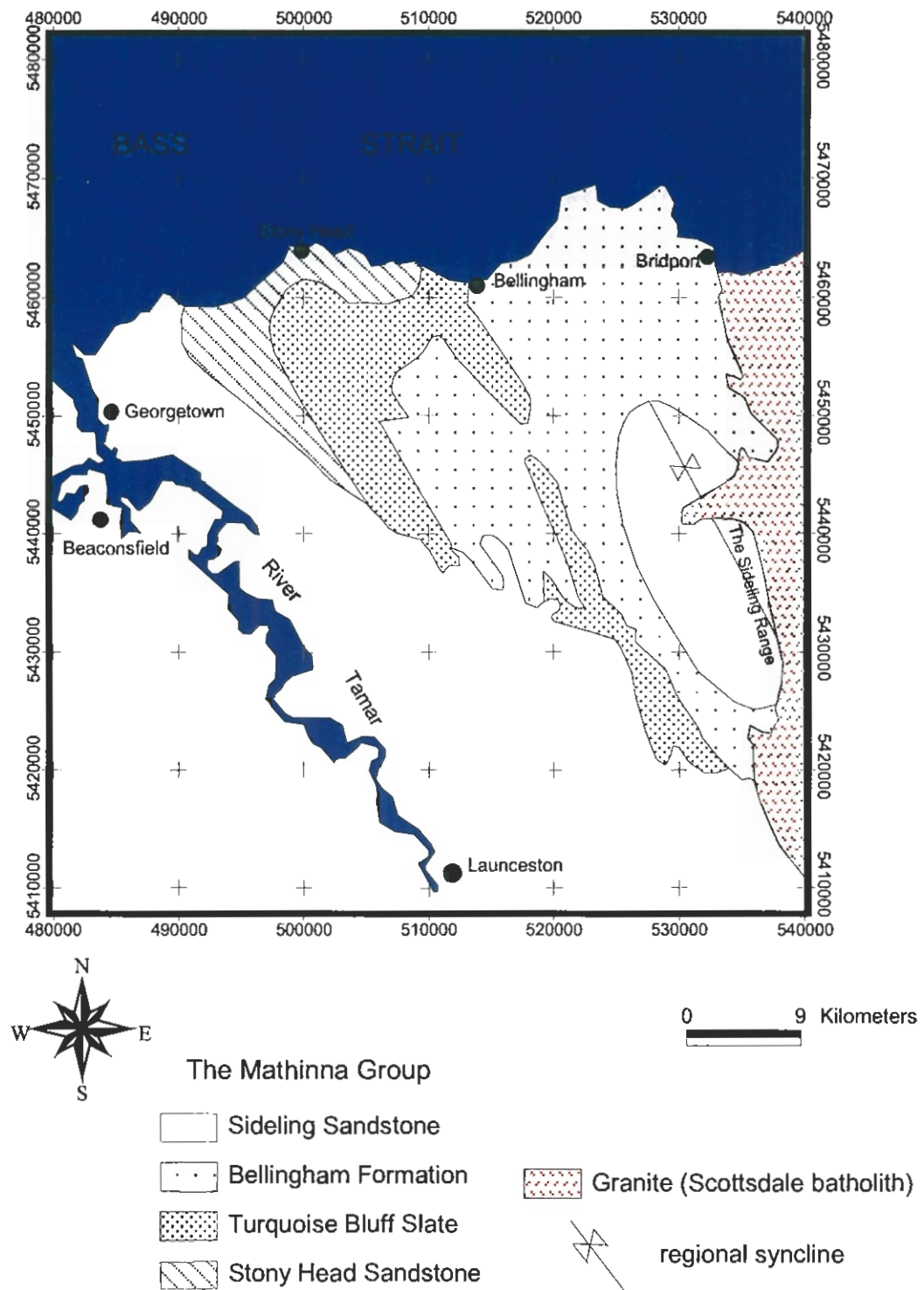


Figure 4.6 : A modified regional sedimentological map of the Mathinna Group west of the Scottsdale batholith. The boundary of the Sideling Sandstone has been extended from the boundaries set by Powell et al., (1993).

Chapter 5 Gold Mineralisation

5.0 Previous Work

Gold mineralisation on the Sideling Range has recently been discovered following a prospecting trip by Mr. Frank Bardenhagen and Mr. Russell Fulton. The mineralisation occurs in veins of auriferous comb quartz sulphide and quartz breccia (\pm sulphides) that are up to half a metre wide (Fulton pers. comm. 2000). The mineralisation is within the Mathinna Group sediments in the contact aureole on the western margin of the Scottsdale Batholith (Figure 5.0).

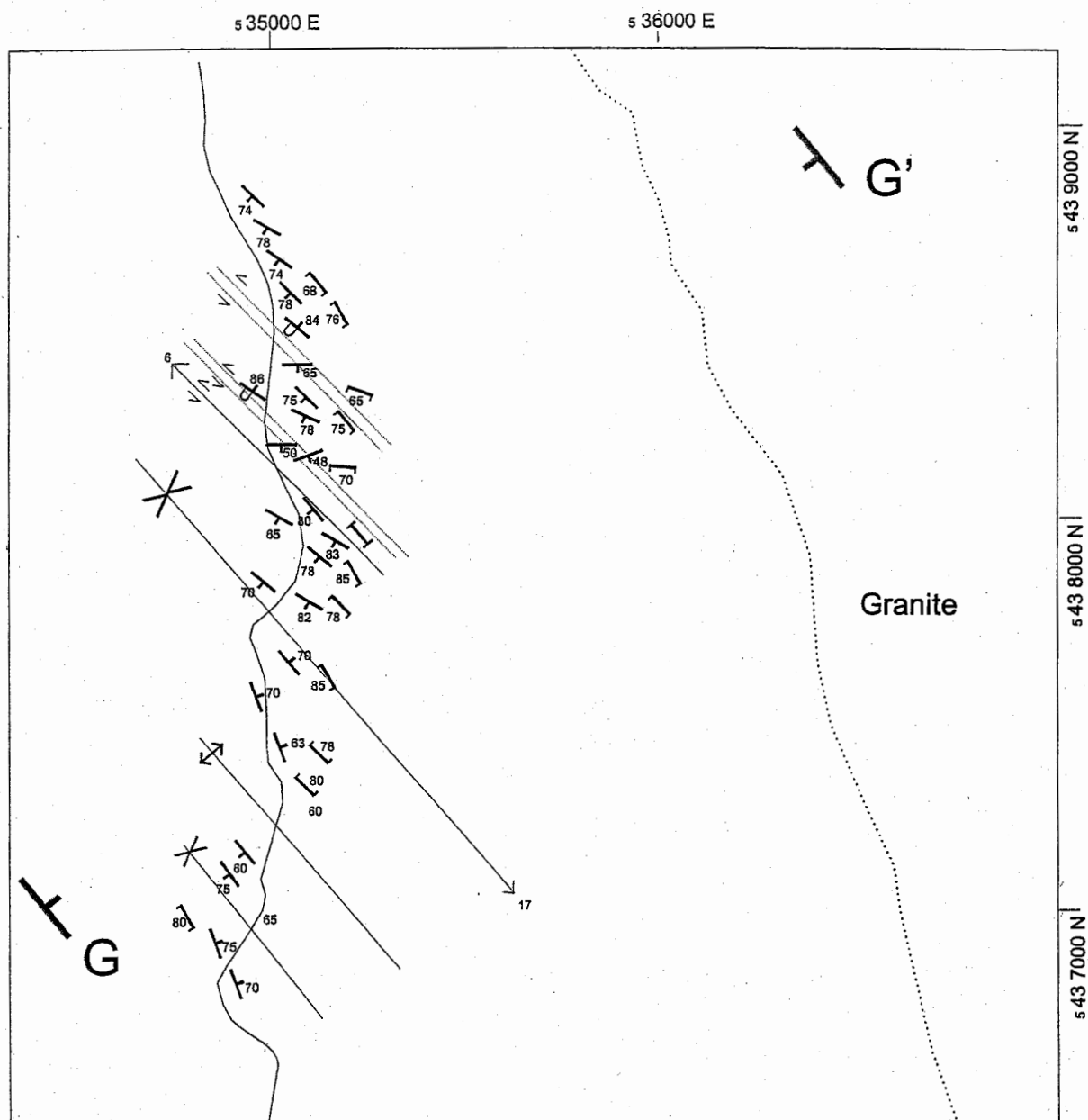
The spatial association of the gold with the contact aureole opens the possibility the gold is related to the granite intrusion rather than a typical turbidite hosted mesothermal gold vein style. Granite related gold has been discovered at the nearby goldfields of Lisle, Golconda and Panama. At these fields gold bearing veins have been discovered within the roof of the Lisle granodiorite and the contact metamorphosed sandstones (Marshall 1969). However no gold bearing veins have yet been reported within the Scottsdale Batholith.

5.1 Lithology of the Mineralised Area

The lithology in the mineralised area consists of spotted psammites and pelites that have been overprinted by silicification that gives the rocks a creamy to pale brown colour. Iron staining is also quite evident overprinting the rocks with a greeny-grey appearance. The original sedimentary features are still visible and all the three sandstone facies reported in Chapter 4 are recognised in this zone. The facies arrangement consists of facies 1 with small interlayers of facies 3 overlain by facies 2.

5.2 Structure of the Mineralised Area

The bedding surfaces are well defined despite the intense hornfels spotting. Stratigraphic facing can be determined from cross laminations in facies 2 sandstone



- | | |
|----------------------------------|--------------------------|
| α^{65} Overturned bedding | Syncline |
| γ^{70} S0 strike/dip | Anticline |
| δ^{80} S1 cleavage | Cross section boundaries |
| Strike slip fault | Granite boundary |
| Sinistral shear zone | |



(All measurements taken to true north)

Figure 5.0: The location and structural data for the area of gold mineralisation. The western margin of the Scottsdale Batholith is approximately one kilometre to the east. Structural data has been taken from along a recently built forestry road.

and from the facies 1 sandstone beds with fine silty tops. Bedding is very steep with two small areas of overturned beds dipping to the NE.

No fold closures were exposed within the area. The statistically calculated fold plunge and interlimb angle are 17° — 140° and 47° respectively (Figure 5.1a). The folds are cylindrical, upright and close with symmetrical fold profiles and the dominant structure is a large syncline (Figure 5.2).

A fine and continuous S1 cleavage (Twiss and Moores 1992) that appears to be axial planar to the folds is evident in the siltstone division of the beds. The cleavage strikes to the SE and is dominantly subvertical to steeply SW dipping (Figure 5.1b).

One known fault and two areas of bedding and cleavage rotation inferred to be a result of faulting and shearing are evident in the area. A sinistral strike-slip fault parallel to the bedding and dipping gently to the NW was located 250 metres NE of the major synclinal hinge. Ten metres north of this fault, bedding and S1 cleavages are anomalous. Anticlockwise strike rotations of between 30° — 90° and slightly shallower bedding dips to the S and SW occur for 15 metres. The bedding orientation returns to its typical strike and dip for approximately forty metres before a recurrence of the anomalous beds again for approximately ten metres along the road to the north (See Figure 3.6 b for illustration).

5.3 Veins

Very little veining is visible in the outcrop although a large proportion of blocky white massive quartz float and silicified country rock is scattered throughout the mineralised area. Previous work by Russell Fulton (pers comm. 2000) identified veining from trenches that have since been refilled. The majority of the veining is located in the two inferred NW striking shear zones in which intense veining occurs. The veins are thin and discontinuous, less than 0.5 m thick and less than 3 metres, occurring sporadically over a strike length of approximately 600 metres. The majority of the veins are orientated subparallel to the bedding (Figure 5.1c) and occur on lithological contacts i.e. sand and silt contacts.

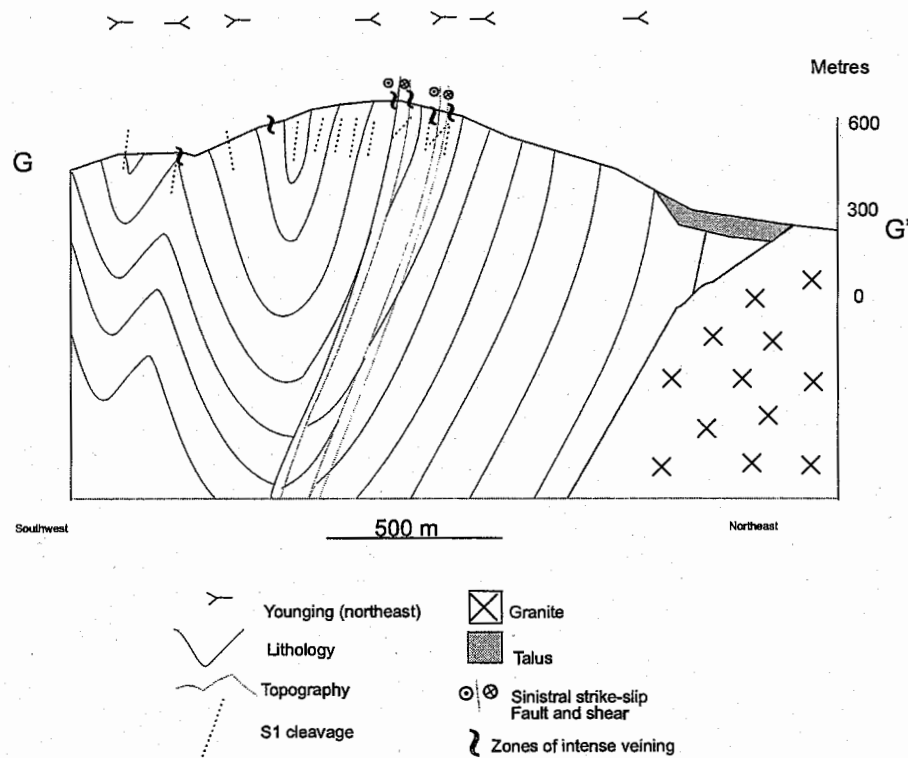
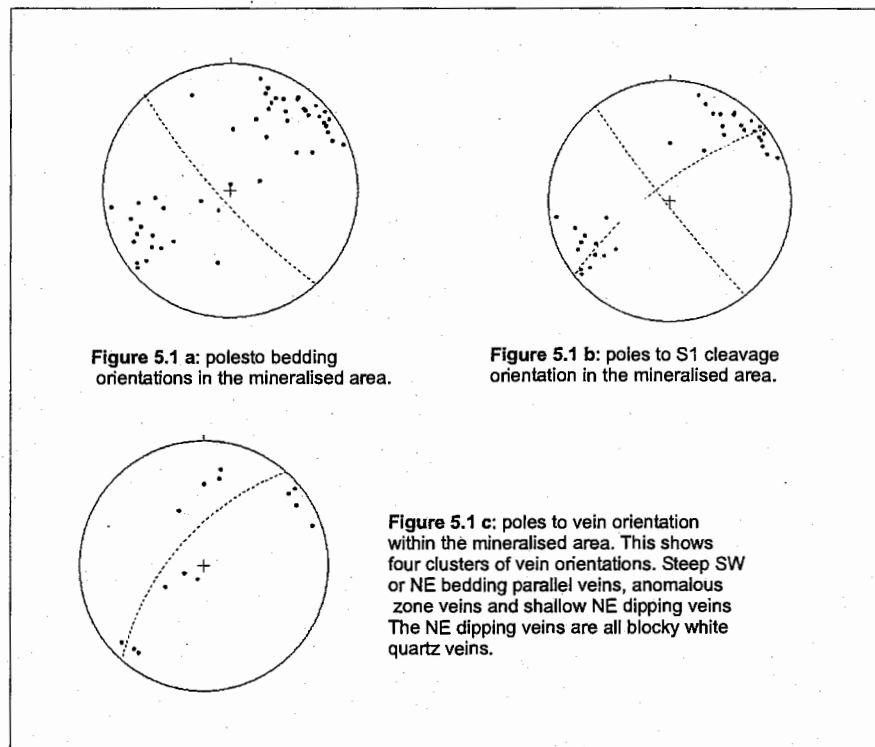


Figure 5.2: A cross section of the area of gold mineralisation G-G'. The entire cross section lies within the contact aureole and the lithology consists of spotted psammmites.

Four different types of quartz veins are identifiable in the outcrop; comb quartz veins, brecciated quartz veins, thin laminated veins, and massive blocky quartz veins. The blocky quartz veins are the only veins that appear to deviate from a bedding parallel orientation. No gold was visible within any of the veins examined.

5.3.1 Quartz-comb and related intra-vein cross-cutting quartz-sulfide networks

The quartz comb veins are fibrous and coarse grained with quartz crystals up to 0.5 cm long. The crystal growth is syntaxial and oriented perpendicular to the vein wall, terminating in cavities near the centre of the vein. In some cases the vein growth occurred in two different phases with smaller crystals on the periphery of the vein and larger quartz crystals in the centre of the vein (Figure 5.3). The larger quartz crystals display oscillatory zoning and are either a white colour or variably translucent. Thin selvages of chlorite micas finely aligned parallel to the vein boundary are visible. All of the comb quartz veins are thin, typically less than 10 cm and commonly occur parallel to bedding and in between lithological contacts.

A quartz comb vein found in the float next to the shear zone displays the effects of a later strain in the form of multiple fractures cutting from vein boundary to vein boundary. On one of the boundaries of the comb vein a cross-cutting vein consisting of a fine-grained matrix of equigranular quartz with aggregates of acicular pyrites is apparent (Figure 5.3). The equigranular quartz and pyrites transgress the comb-quartz-vein boundary around the fractures infilling the fractures and cavities (Plate 6).

5.3.2 Laminated quartz veins

Laminated veins that are composed of bands of fine to medium grained clear quartz oriented parallel to the vein wall occur rarely throughout the outcrop (Fulton pers comm. 2000). A couple of the samples in outcrop displayed 1-2 cm bands of pyrite (Fulton pers comm. 2000). The veins are between 1-5 cm thick and oriented parallel to the bedding plane (Fulton pers comm. 2000).

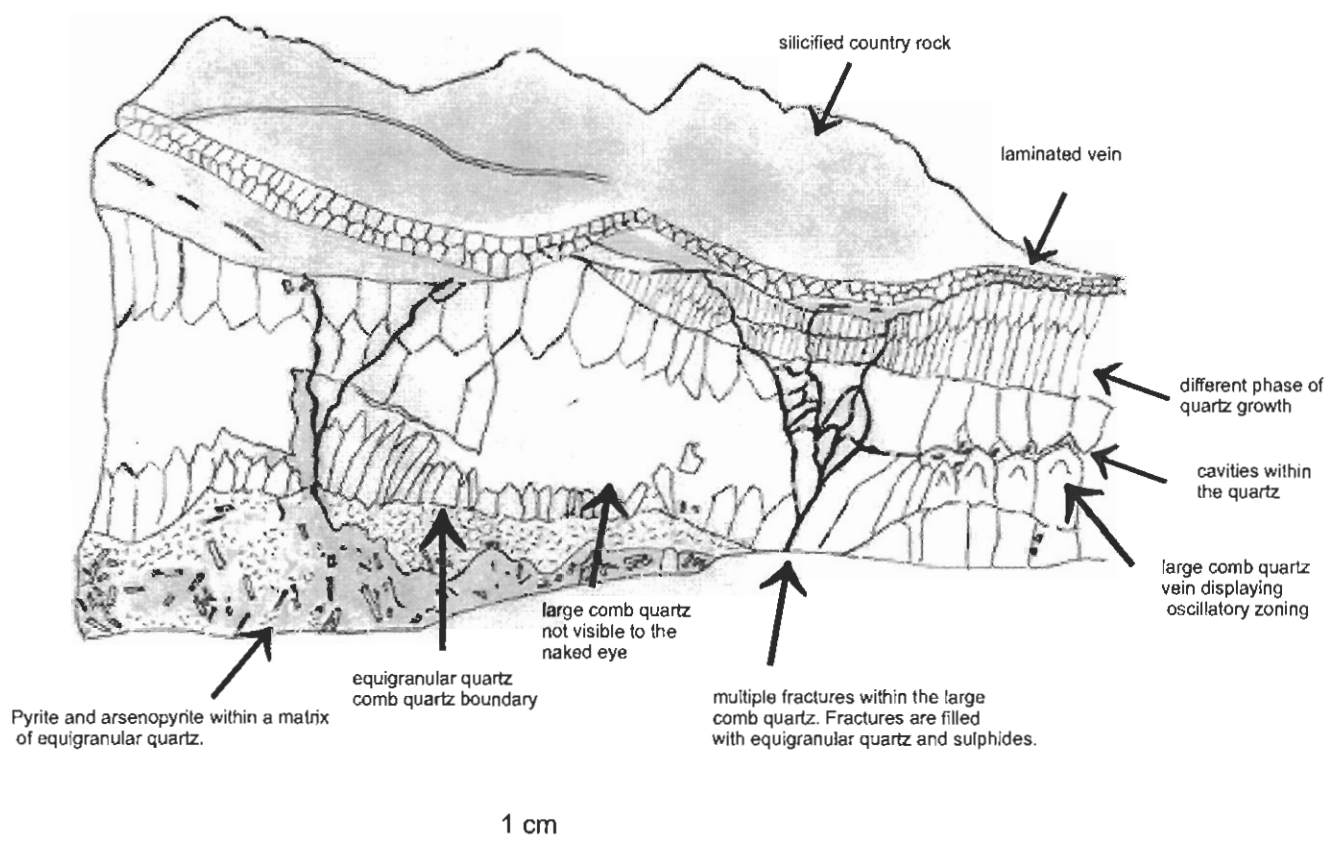


Figure 5.3: A sample of a sulphide bearing comb-quartz-vein. The majority of the sulphides are associated with the cross-cutting quartz vein composed of small equigranular quartz situated at the bottom left hand corner of the specimen (See Plate 6). Specimen 1(a) D.T.

5.3.3 Quartz breccia veins

The brecciated veins consist of angular and tabular fragments of highly limonitised and silicified hornfels wall rock lying in a matrix of coarse-grained anhedral quartz that is a milky white colour. Very minor proportions of very fine-grained cubic pyrites occur within the quartz matrix. The brecciated veins are parallel to the plane of bedding.

5.3.4 Blocky white quartz veins

Blocky quartz is the most commonly encountered quartz along the zone of mineralisation. It has a vitreous lustre, iron-stained fractures and a milky white colour. The quartz crystals are medium and coarse grained and closely packed without any visible cavities. These veins are typically thin, commonly less than 0.2 m. The veins are barren and in some cases crosscut bedding.

5.4. Paragenesis of the quartz veining and relationship to gold mineralisation

The quartz veining relationships observed involved blocky quartz veins crosscutting all other vein types and sulphide bearing veins crosscutting the comb-quartz vein. Therefore the paragenetic sequence is:

1. comb quartz vein (brecciated vein?)
2. sulphide bearing quartz veins (brecciated vein?)
3. blocky white quartz veins.

Although no gold was visible within any of the veins, assays of the rock chip sampling from Fulton pers comm. (2000) reveal that gold mineralisation is associated with veins containing visible pyrite.

5.5 Sulphide chemistry

Petrographic studies of the sulphides within the comb quartz and quartz breccia veins revealed large proportions of acicular shaped sulphides composed of a core of pyrite rimmed with dog tooth shaped arsenopyrite (Plates 7 & 8). The pyrite and

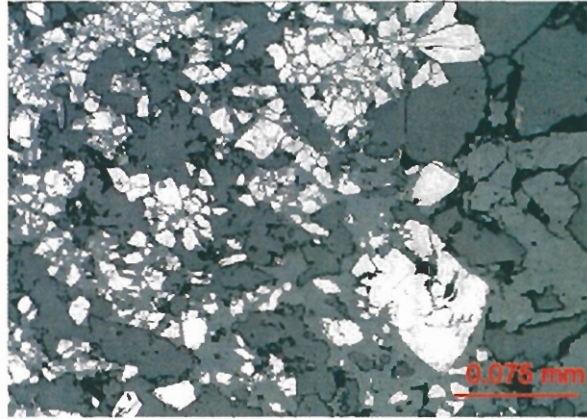


Plate 6: Small subhedral pyrites and equigranular quartz residing within the fractures between the large comb-quartz veins and arsenopyrite. Specimen 1 (a) D.T.

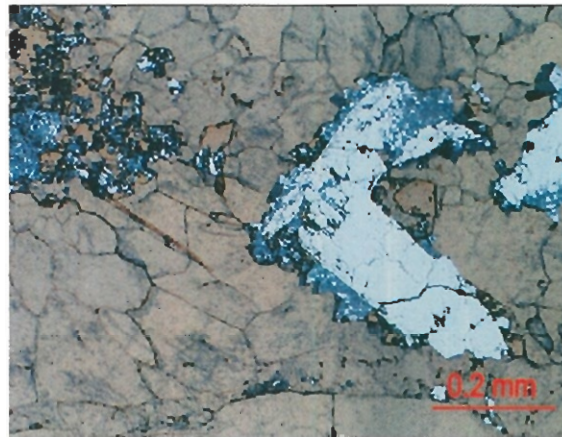


Plate 7: A photomicrograph of an acicular shaped pyrite with dog-tooth edges of arsenopyrite surrounded by fine-grained equigranular quartz. Specimen 1 (a) D.T.

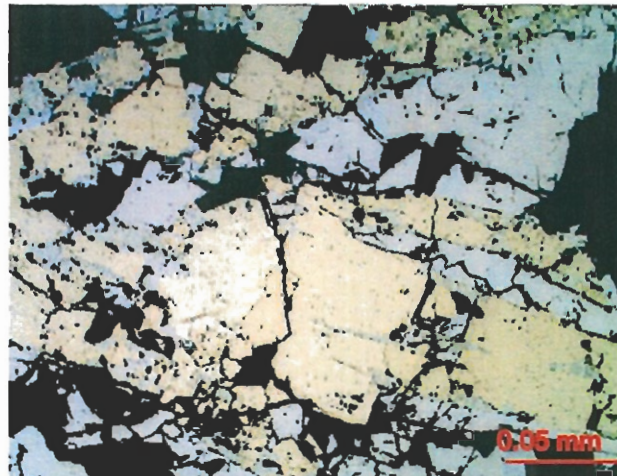


Plate 8: A photomicrograph displaying pyrite (yellow) and arsenopyrite (white/yellow). Specimen 1 (a) D.T.

arsenopyrite grains were analysed by electron microprobe. The analysis defined the average composition and were used to check for variation from the cores to the rims (Table 1 and Table 2).

The pyrites are extremely close to the pure end member pyrite. Ni, Cu, Co, Zn and As were all below detection limits. Se content was uniform at about 0.03% and the S/Se ratio is ≈ 2000 (Figure 5.4). No variation in elemental composition was noted between the rims or the cores of the pyrite. The arsenopyrites are also very pure. Ni, Cu, Co, and Zn are below detection limits for the analyses. The Se content in the arsenopyrite grains was slightly greater than the pyrites with an average content of 0.26 % which is about 0.005 anions in the structural formula (Figure 5.4). The arsenopyrite has As at 0.82 to 0.88 in the structural formula. No systematic variation was detected. The As content is 28-29 atomic % and suggests temperatures of equilibrium below 350°C for coexisting pyrite and arsenopyrite based on the phase relationships reported by Kretschner and Scott (1976).

Kitto (1997) compiled trace element compositions of a large range of pyrites. Pyrites associated with Devonian granites from western Tasmania were found to have very low Co and Ni contents in comparison to Cambrian VHMS deposits. The values determined here are consistent with the granite veins system but are much lower than typical VHMS related pyrites. The very low values of trace elements found in these pyrites are typical of high temperature vein systems where coexisting pyrite and arsenopyrite grow at equilibrium (Huston *et al.*, 1995). Studies by Huston *et al.*, (1995) and Rowins *et al.*, (1997) have shown that pyrites of magmatic hydrothermal origin have S/Se ratios less than 20 000. The value of 2000 for the Se/S ratio of pyrites determined for this study suggests a very high magmatic component to the fluid.

Gold associated with pyrite and arsenopyrite occurring in equilibrium is also observed at Golden Gate at Mathinna and at Beaconsfield in northeastern Tasmania (Burrett and Martin 1989). Gold occurs in a vein system in the contact aureole of an Upper Devonian granite in Maldon, central Victoria. The gold at Maldon also contains pyrite and arsenopyrite but the existence of a range of typical Bi containing minerals

Pyrite											
Label	core	int	rim	core	int	rim	core	rim	core	rim	sm py
Weight percent											
Fe	46.57	46.46	46.75	47.14	46.86	46.58	46.73	46.56	46.29	46.20	46.44
Co	0.000	0.000	0.000	0.000	0.000	0.000	0.000	0.000	0.000	0.000	0.000
Ni	0.000	0.004	0.006	0.000	0.000	0.001	0.000	0.000	0.001	0.000	0.000
Cu	0.002	0.006	0.000	0.000	0.002	0.001	0.000	0.007	0.000	0.006	0.011
Zn	0.004	0.000	0.001	0.000	0.000	0.002	0.000	0.000	0.000	0.000	0.000
S	54.09	53.74	53.93	54.14	54.24	54.21	53.95	54.14	54.22	53.95	54.29
As	0.000	0.008	0.000	0.000	0.147	0.000	0.000	0.022	0.000	0.013	0.079
Se	0.028	0.032	0.019	0.031	0.024	0.028	0.033	0.033	0.022	0.016	0.026
Total	100.69	100.25	100.70	101.31	101.27	100.83	100.71	100.76	100.54	100.19	100.84
Structural formula (cations)											
Fe	0.988	0.992	0.995	1.000	0.991	0.987	0.995	0.987	0.980	0.983	0.981
Co	0.000	0.000	0.000	0.000	0.000	0.000	0.000	0.000	0.000	0.000	0.000
Ni	0.000	0.000	0.000	0.000	0.000	0.000	0.000	0.000	0.000	0.000	0.000
Cu	0.000	0.000	0.000	0.000	0.000	0.000	0.000	0.000	0.000	0.000	0.000
Zn	0.000	0.000	0.000	0.000	0.000	0.000	0.000	0.000	0.000	0.000	0.000
Structural formula (anions)											
S	2.000	1.999	2.000	2.000	1.997	2.000	1.999	1.999	2.000	2.000	1.998
As	0.000	0.000	0.000	0.000	0.002	0.000	0.000	0.000	0.000	0.000	0.001
Se	0.000	0.000	0.000	0.000	0.000	0.000	0.001	0.001	0.000	0.000	0.000

Table 1: Average composition of pyrite. The pyrites were probed from the cores to the rims. The results reveal very clean pyrites with most trace elements below the detection limit. No variation is observed between the cores and the rims.

Arsenopyrite									
Label	rim	asp	asp	rim	rim	asp	rim	rim	asp
Weight percent									
Fe	35.36	35.81	34.76	35.41	35.23	35.47	33.28	34.67	34.59
Co	0.000	0.000	0.000	0.000	0.000	0.000	0.000	0.000	0.000
Ni	0.003	0.000	0.000	0.005	0.000	0.003	0.003	0.000	0.000
Cu	0.011	0.003	0.008	0.009	0.000	0.003	0.013	0.003	0.002
Zn	0.000	0.000	0.000	0.006	0.000	0.000	0.004	0.000	0.002
S	22.31	23.60	23.35	22.56	23.15	23.32	21.88	22.69	22.57
As	41.33	38.70	38.86	40.28	39.13	39.51	40.41	40.77	40.66
Se	0.315	0.238	0.258	0.262	0.258	0.264	0.225	0.272	0.257
Total	99.33	98.35	97.23	98.53	97.77	98.57	95.82	98.41	98.08
Structural formula (cations)									
Fe	1.012	1.021	0.996	1.019	1.011	1.010	0.973	0.989	0.991
Co	0.000	0.000	0.000	0.000	0.000	0.000	0.000	0.000	0.000
Ni	0.000	0.000	0.000	0.000	0.000	0.000	0.000	0.000	0.000
Cu	0.000	0.000	0.000	0.000	0.000	0.000	0.000	0.000	0.000
Zn	0.000	0.000	0.000	0.000	0.000	0.000	0.000	0.000	0.000
Structural formula (anions)									
S	1.112	1.172	1.165	1.131	1.157	1.156	1.114	1.127	1.127
As	0.882	0.823	0.830	0.864	0.837	0.838	0.881	0.867	0.868
Se	0.006	0.005	0.005	0.005	0.005	0.005	0.005	0.005	0.005

Table 2: Average composition of arsenopyrite. The arsenopyrites were probed from the core to rims with no variation observed. The arsenopyrites are also very clean and have a greater Selenium content than the pyrite.

(Berlein *et al.*, 1998) is very distinct from any vein system yet found on the Sideling Range.

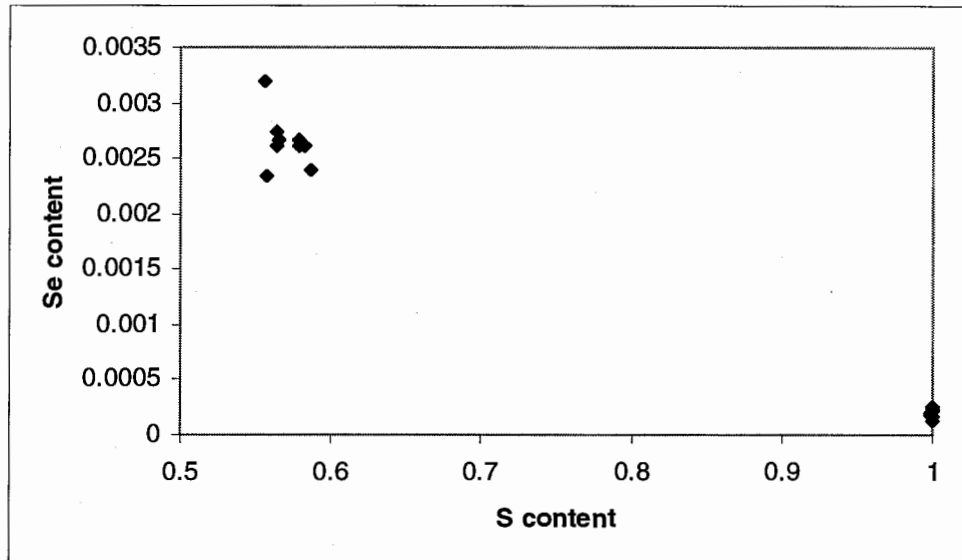


Figure 5.4: Selenium vs. Sulphur content for pyrite and arsenopyrite. Arsenopyrite plots in the upper left-side corner whereas pyrite plots in the lower right-side corner.

5.6 Summary

Gold mineralisation at the Sideling Range occurs in a post D1 probable sinistral shear zones in the contact aureole of the Scottsdale Batholith. The gold is associated with thin and discontinuous quartz veins that lie within and subparallel to spotted psammities. Three or four generations of quartz veining are apparent within the sediments and the gold mineralisation is associated with laminated and equigranular type quartz veins that intrude the comb quartz with aggregates of pyrite and arsenopyrite. Microprobe analysis of the sulphides show they contain low levels of most trace elements but elevated levels of Selenium. The level of As in arsenopyrite coexisting with pyrite suggests the temperature of the fluid was below 350°C. The Selenium levels in pyrite suggest a magmatic component to the fluid which formed the veins.

Chapter 6 Conclusion

One main phase of NNW trending and predominantly SE plunging folds are recognised within the Sideling Range. An axial planar S1 cleavage is evident in the siltstone but is rarely found in the sandstone. Spatial evidence suggests that rare crenulating S2 cleavages, fold tightening and a small clockwise rotation of the fold trend within the aureole is associated with the intrusion of the Scottsdale granodiorite.

Faulting at the Sideling Range is rare, small scale and commonly reverse dip-slip faulting that occurs close to the hinges of the folds. The deflection of bedding and cleavages on the reverse dip-slip faults provides some evidence of a post D1 deformation that tightens pre-existing folds outside of the aureole.

Regionally the fold trend of the Sideling Range is conformable and the beds are stratigraphically the youngest beds on the limb of a large regional syncline that possibly has its hinge situated within the contact aureole at the Sideling Range.

The Sideling Range sandstones are medium to fine-grained, poorly sorted and texturally immature quartz greywackes. The most common sandstone throughout the range is a thickly bedded and ungraded, medium to fine-grained sandstone that has a thin silt top. This sandstone facies occurs interlayered with siltstone and thinly bedded sandstones that have sedimentary structures such as graded bases, cross laminations and parallel laminations that are typical of the classic turbidite deposit. The facies associations observed at the Sideling Range indicate that the most likely depositional environment for the sediments was a deep-sea channelised fan and channel overbank environment.

The Sideling Range sediments have been categorised within the Sideling sandstone unit as defined by Powell *et al.*, (1993), and not the Bellingham Formation. The sediments are mineralogically the same as the Bellingham Formation but the sandstone beds of the Sideling Range are thicker and comprise greater ratios of sand to silt which suggests that the Sideling sandstone is from a comparatively more proximal submarine fan environment than the Bellingham Formation. The stratigraphy mapped at the Sideling Range indicates that the Sideling sandstone has a

thickness of approximately 1500 metres. Therefore the Sideling sandstone is a distinct lithological unit within the Mathinna Group.

Gold mineralisation at the Sideling Range occurs in thin and discontinuous comb quartz and laminated quartz veins within a post D1 probable shear zone. Pyrite and arsenopyrite are associated with the mineralisation and the level of As in the arsenopyrite suggests that the temperature of the gold mineralising fluid was below 350° C . Selenium levels in the pyrite suggest a magmatic component to the fluid.

References

- Banks, M.R., (1962). Mathinna Beds, in Spry, A.H and Banks, M.R. (eds) The Geology of Tasmania. J. Geol. Soc, Aust. 9(2): 182-184.
- Banks, M.R., and Smith, A., (1968), A graptolite from the Mathinna Beds northeast Tasmania: Australian Journal of Earth Sciences, v. 31, p. 118-119.
- Berlein, F.P., Fuller, T., Stilwe, K., Arne, D.C. and Keays, R.R. (1997). Wallrock alteration associated with turbidite-hosted gold deposits. Examples from the Palaeozoic Lachlan Fold Belt in Central Victoria, Australia. Ore Geology Reviews 13 (1998) pp. 345-380.
- Boggs S.R. Jr. (1995). Principles of Sedimentology and Stratigraphy. Prentice and Hall. U.S.A.
- Kitto, P.A (1997). Trace Element Investigation of Pyrite: a discriminator for Cambrian and Devonian mineralisation and fault histories. CODES: AMIRA Project P.291A – Structure and Mineralisation of Western Tasmania.
- Burrett, C.F. and Martin, E.L., (1989). Geology and Mineral Resources of Tasmania. Geological Society of Tasmania.
- Drown, C.G., (1984), Structure of the Mathinna Beds: Unpublished BSc(Hons) thesis, University of Tasmania, Hobart.
- Fulton, R., (2000). Closed File Report on the Sideling Range exploration lease. Mineral Resources Tasmania.

Gee, R.D. and Groves, D.I., (1971), Structural features and mode of emplacement of part of the Blue Tier Batholith in northeastern Tasmania: *Journal of the Geological Society of Australia*. v. 18, part 1, p. 41-46.

Goscombe, B.D., McClenaghan, M.P, and Everard, J.L., (1992), Contact metamorphism of the Mathinna Beds and the depth of crustal residence during mega-kinking in northeast Tasmania: Tasmania Department of Mines Report, 1992/42.

Goscombe, B. D., Findlay, R.H., McClenaghan, M.p & Everard, J. (1994). Multi-scale kinking in north-east Tasmania; crustal shortening at shallow crustal levels. *Journal of Structural Geology* 16: 1077-1092.

Haines, P. (2000) Personal Communication. University of Tasmania.

Huston, D.L., Suter, G.F., Sie, S.H., Cooke, D.R., and Both, R.A. (1995). Trace Elements in Sulfide Minerals from Eastern Australia Volcanic-Hosted Massive Sulfide Deposits: Part 1. Proton Microprobe Analyses of Pyrite, Chalcopyrite, and Sphalerite, and Part 2. Selenium Levels in Pyrite: Comparison with $\delta^{34}\text{S}$ Values and Implications for the Source of Sulfur in Volcanogenic Hydrothermal Systems. *Economic Geology*. Vol. 90, pp. 1167-1196.

Keele, R., (1994). Structure and veining in the Devonian-aged Mathinna-Alberton Gold Lineament, northeast Tasmania. *Tasmania Development and Resources*.

Kitto, P.A., (1997). Trace element Investigation of Pyritew: a discriminator for Cambrian and Devonian mineralisation and fault histories. *Structure and Mineralisation of Western Tasmania*. CODES: AMIRA Project P. 291A.

Marshall B. Geological Survey Explanatory Report Pipers River. (1969) Report for the Tasmania Department of Mines No. 31.

Mc Clenaghan, M.P. (1989). Mid-Palaeozoic granitoids. In Burrett, C.F. and Martin, E.L (eds) *Geology and Mineral Resources of Tasmania*. Special Publication Geological Society of Australia 15, 253-270.

Mc Clenaghan, M.P., and Calver, C.R. (comp)., (1994), *Geological Atlas 1:250 000 digital series. Geology of northeast Tasmania: Geological Survey of Tasmania*.

Mutti, E., Parea, G.C, Ricci Lucchi, F., Sagri, M. Zanzucchi, G., Ghibaudo, G., and Iaccarino, S. (1975). Examples of Turbidite Facies and Facies Associations from Selected Formations of the Northern Apennines. IX International Congress of Sedimentology. Field Trip A11.

Mutti, E and Ricci Lucchi, F. (1972). " Le torbiditi dell' Appennino settentrionale: Introuzione all' analisi di facies. " *Memoirie della Societa Geologica Italiana*, 1972, p. 161-199. Translated by Nilsen, T.H 1978. *Internatinal Geology Review*, V. 20, No. 2.

Patison, N.L., Berry R.B., Davidson G.J., Taylor B.P., Botrill R.S., Manzi B., Ryba J. and Shepherd R.E. (2000). Regional metamorphism of the Mathinna Group, northeast Tasmania. In Press.

Powell,C.McA., Baillie, P.W, Conaghan,P.J and Turner, N.J. (1993). The mid-Palaeozoic turbiditic Mathinna Group, northeast Tasmania. *Australian Journal of Earth Sciences* 40, 169-196.

Powell,C.McA., Baillie, P.W, (1992). The tectonic affinity of the Mathinna Group in the Lachlan Fold Belt. *Tectonophysics* 214, 193-209.

Reed, A.R., (1998), Structural controls on mesothermal turbidite-hosted lode-gold mineralisation in northeast Tasmania: Unpublished draft report, Mineral Resources Tasmania.

Rickards, R.B. and Banks, M.R. (1979). An Early Devonian monograptid from the Mathinna Beds. *Alcheringa* 3, 307-311.

Rowins, S.M., Groves, D.I., McNaughton, N.J., Palmer and Eldridge M.R. (1997). A Reinterpretation of the Role of Granitoids in the Genesis of Neoproterozoic Gold Mineralisation in the Telfer Dome, Western Australia. *Economic Geology and the Bulletin of the Society of Economic Geologists*. Vol. 92 No. 2.

Roach, M.J. (1994). The regional geophysical setting of gold mineralisation in northeast Tasmania. Unpublished Ph.D thesis, University of Tasmania: Hobart.

Taheri, J. & Findlay, R.H., (1992). Northeast Goldfields: A summary of the Tower Hill, Mathinna and Dans Rivulet Goldfields. *Mineral Resources Tasmania*. 1992/10.

Turner, N.J. (1980). Composite geological profile across Tasmania. Report Tasmania Department of Mines 1980/38.

Turner, N.J., Black, L.P. and Higgins, N.C. (1986). The St Marys Porphyrite and related dykes – a Devonian intracaldera ignimbrite and its feeder. *Australian Journal of Earth Sciences* 33, 201-218.

Twiss, R.J and Moores, E.M. (1992). *Structural geology*. W.H. Freeman and Company, New York.

Varne, R. and Fulton, R. (1994). The role of Devonian granodiorites and the influence of Tabberabberan tectonism in Tasmania-North Victoria Land (Antarctica) correlations. In Cooke, D.R and Kitto, P.A. (eds) *Contentious issues in Tasmanian geology*, Geological Society of Australia 39, 61-62.

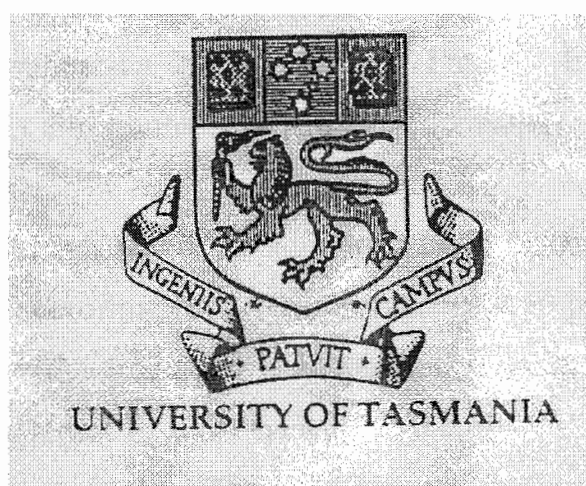
Walker, R.G., (1984). *Facies Models: Second Edition*. Geoscience Canada. Reprint Series 1.

Williams, E.,M. McClenaghan, M.P. and Collins, P.L.F. (1989). Mid-Palaeozoic deformation, granitoids and ore deposits. In Burrett, C.F. and Martin, E.L. (eds) *Geology and Mineral Resources of Tasmania*. Special Publication Geological Society of Australia 15, 238-292.

APPENDICES

Deep-water systems: Models, Concepts and Turbidites.

David Thompson, B.Sc.



A literature review submitted in partial fulfillment of the requirements for the degree of Bachelor of Science with Honours

Department of Geology,
University of Tasmania,
2000

ABSTRACT

Deep water sand systems have been studied a great deal because they are considered important hydrocarbon exploration targets. They vary a great deal from system to system and it is increasingly obvious that facies and fan models that have been created will never entirely cover the wide spectrum of deposits that are being discovered. Many disagreements exist over terminology, models and turbidite concepts and their usage in interpreting the vast variety of deep-water sand systems. This paper reviews the processes important for deep-sea sedimentation, the formation of ideas and the disagreements that have arisen.

CONTENTS

Chapter 1	Introduction	1
Chapter 2	Depositional Processes	3
2.1	Environment of Deposition	3
2.2	Sediment gravity flows	3
2.2.1	Turbidity currents	3
2.2.2	High and Low Density flows	5
2.2.3	Fluidised flows	6
2.2.4	Grain flows	6
2.2.5	Debris flows	6
Chapter 3	Depositional Models	8
3.1	Grain flow Model	8
3.2	Debris Flow Model	9
3.3	Liquefied flow Model	10
3.4	The Bouma sequence	10
3.5	High and Low Density turbidites: The Lowe Model	11
3.6	Turbidite Facies	13
3.6.1	Facies A: Arenaceous-conglomeratic facies	14
3.6.2	Facies B: Arenaceous facies	14
3.6.3	Facies C: Arenaceous-pelitic facies	14
3.6.4	Facies D: Pelitic arenaceous facies	14
3.6.5	Facies E: Pelitic-arenaceous facies 2	14
3.6.6	Associated Facies	15
3.7	Modified Facies Model	15
3.8	Shanmugam et al. (1995) Depositional Facies	15

Chapter 4	Submarine Fan Models	17
4.1	The General Model	17
4.2	Outcrop Data from Ancient Systems	18
4.3	Shallow Penetration Geological and Geophysical Data from Modern Systems	19
4.4	Deep Penetration Seismic Reflection Data	19
4.5	Summary	21
Chapter 5	Conclusion.	22

LIST OF FIGURES

Figure No.	Title
1	Experimental turbidity current
2	A Dynamic Debris Flow Sequence
3	Grain Flow Model
4	Debris Flow Model
5	Liquefied Flow Model
6	The Bouma Sequence
7	Idealised High Density Turbidite Deposit
8	The General Fan Model
9	Mutti and Ricci Lucchi Ancient submarine fan environment
10	Shallow penetration and sidescan sonar derived perspective of the Monterey fan
11	Seismic Reflection Profile
12	Walkers preliminary fan model

LIST OF TABLES

Table 1:	Shanmugam et al. Facies scheme for the North Sea
----------	--

CHAPTER 1

Introduction

“Before the Bouma sequence varied interpretations were offered for individual beds or groups of beds (Walker 1984).”

A large body of information has been compiled on deep-water sand systems because they are potentially important hydrocarbon reservoirs. Facies and deep-water submarine fan models have been recreated from fieldwork on ancient outcrop, modern and ancient drill core, and seismic reflection and sidescan sonar. The models have been useful tools for field geologists uncovering mostly ancient but also modern successions. They are helpful because they give a basis for identification, and at the same time an interpretation of the environment and depositional patterns of the sediment.

As the knowledge base has increased, the huge complexity of depositional patterns characterising modern and ancient deep-water sand systems has been realised and it is very unlikely the full extent will ever be explored. Therefore a limitation in using a model exists in that it is unlikely that any two deep-water sand systems could have formed in *exactly* the same way.

Because observation and description of deep-water sand systems can quite easily deviate from the standard models, a broad range of disagreements have arisen regarding their terminology, facies models and concepts (Bouma et al. 1985, Shanmugam 1997). A central issue is the meaning of “turbidite.” The term was originally used to describe how sand and mud sediment loads were transported through water and deposited in deep environments (turbidity currents; Kuenen and Migliorini 1950 from Walker 1968), and has since been experimentally defined and represented by the Bouma Sequence. Turbidite is commonly used in a general sense to refer to any submarine fan system with sand and mudstone (turbidite system; Walker 1967, Mutti and Ricci Lucci 1972, Normark et al. 1993 etc.). Shanmugam (1997) argues that many of the submarine fans are mainly composed of debris flow deposits and calling them turbidite systems is misleading.

This paper reviews the depositional processes of deep-water sand systems, turbidite concepts, facies and fan models and the terminology that is related. A critical review of the literature should lead to objective and informed observation as well as proper description and interpretation of deep-sea sand systems.

CHAPTER 2: Depositional Processes

2.1 Environment of Deposition

Deep-water sands and muds generally accumulate in sedimentary basins on the ocean side of where the land meets the sea. Deep-sea basins that have been investigated vary a great deal in size and shape and sediment fill. This is because these sedimentary basins can form on mature passive margins, active rifting margins, arc or trench systems, basins on continental shelves, transform margins and ocean basins flanked by ridges and seamounts (Bouma et al. 1985).

The tectonic setting of the basin influences all aspects of the system including basin geometry, sediment type and the frequency and volume of the sediment gravity flows feeding the basin (Bouma et al. 1985).

2.2 Sediment gravity flows

The main depositional processes that act to transport sediment into the deep-sea basin have been given the broad term of sediment gravity flows (Haines 2000). The principal subaqueous sediment gravity flows have been classified as debris flows, grain flows, turbidity currents and liquefied sediment flows on the basis of fluid rheology and sediment support mechanisms (Dott 1963; Lowe 1979, 1982 from Shanmugan 1997). This basis distinguishes the four flows by their fluid properties (shear resistance of fluids), fluid motions (laminar or turbulent flow) and grain to grain interaction.

2.2.1 Turbidity currents

Storms that initiate slope failure, and land derived underwater rivers that flow onto the continental slope are largely responsible for turbidity currents (Haines 2000). They can also be initiated as flows during eruption of air-fall ash (Normark and Piper 1991, from Boggs 1995). The sediment-laden water is denser than the surrounding water column and travels down slope as a uniform steady flow or as a surge under the force of gravity.

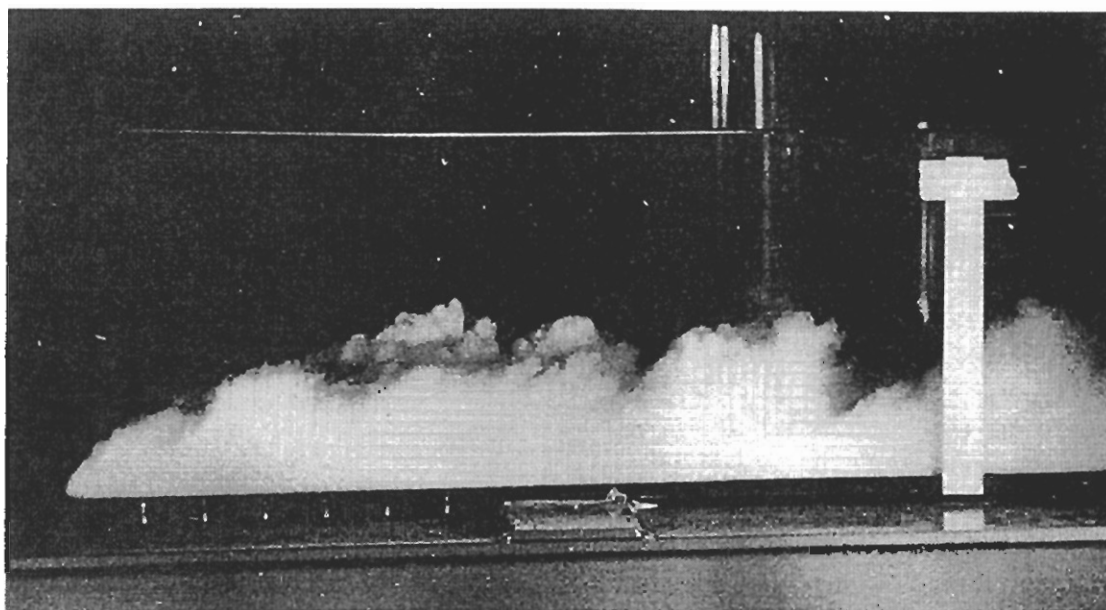


Figure 1
Experimental turbidity current in a flume at Caltech. Water depth is 28 cm. Note characteristic shape of the head of the current, and

eddies behind the head. Sediment is thrown out of the main flow by these eddies - the main flow is only about half of the height of the head.

Experimental turbidity current (from Walker 1992).

Deposition from turbidity currents occurs when the sediment falls out of the turbid state of suspension. The first grains to settle out of suspension and onto the sea-floor are the largest and the heaviest of the grains in the flow, and the subsequent grains that settle out of suspension become progressively lighter (Bouma *Ta* division). Once the flow strength reaches a critical level the grains are deposited by traction sedimentation (*Tb* and *Tc* divisions; Lowe 1982). This mode of transport and deposition is where sand-sized grains get pushed a short distance along a bed in a downcurrent direction due to current forces and the impact of other moving grains (Boggs 1995). As the current directed flow slows down and the grain impacts subside, sediment is deposited by suspension due largely to the gentle pull of gravity (*Td* and *Te* divisions).

The nomenclature of the turbidity current classifies it as fluidal in rheology (Dott, 1963; Lowe, 1979; Nardin et al., 1979; from Shanmugam 1997), and two phase flow of both water and solids that are fully turbulent in state (Middleton 1993 from Shanmugam 1997). They are mainly concentrated in water (~ 74-99% by volume; Middleton 1967, 1993 from Shanmugam 1997).

2.2.2 High and Low Density Flows

The concentration of sediment in the flow has introduced the idea of high density and low density turbidity currents (Lowe 1982). Low density turbidity currents are similar in description and nomenclature to the general turbidity current but are more precisely defined. They are made up of clay to medium sized sand grains and their deposition begins with traction sedimentation rather than direct suspension (Lowe 1982).

High density turbidity currents remain largely conjectural, but the gross similarity between ancient deep-sea deposits and deposits formed by small-scale experimental high-density flows (Middleton, 1967 from Lowe 1982) suggest that they are effective in transporting and depositing sediment in the deep sea (Lowe 1982).

High density flows have higher sediment concentrations than the general turbidity current (Boggs 1995). They are subdivided by Lowe (1982) into sandy flows and gravelly flows. The sandy flows are dominated by a range of grain sizes from clay through to small pebble sized gravel, and the gravelly flows consist of pebble and cobble sized clasts (Lowe 1982). The sandy high-density flows are supported by turbulence and hindered settling, whereas the gravelly flows are supported by dispersive pressure and matrix buoyant lift (Lowe 1982). In experiments on gravelly high density turbidity currents the basal laminar flow that deposited the traction carpet was initially fully turbulent, but during the depositional stage the turbulent flow was transformed into quasi-plastic laminar flow (Shanmugan 1997).

A high density turbidity current is a density stratified flow composed of a lower layer (high concentration, plastic, laminar) and an upper layer (low conc., fluidal, turbulent).

Shanmugan (1997) argues that because sediment gravity flows are classified according to their fluid properties and fluid flow type, you cannot have a single flow defined as both fluidal and plastic in rheology and laminar and turbulent in flow type.

2.2.3 Fluidised Flows

When loosely packed subaqueous sands and muds are put under pressure or subject to shocks from earthquakes, the increased pore pressure causes the water to move and to try to escape upwards. The sediment is forced apart and becomes fully supported by the fluid (Prothero and Schwab 1996). When the sediment is only partially supported by fluid the term liquefied flow has been used (Lowe 1982). Deposition occurs by freezing as the grains settle out of the fluid and reestablish grain to grain contact. Freezing occurs from the base of the flow upward (Boggs 1995).

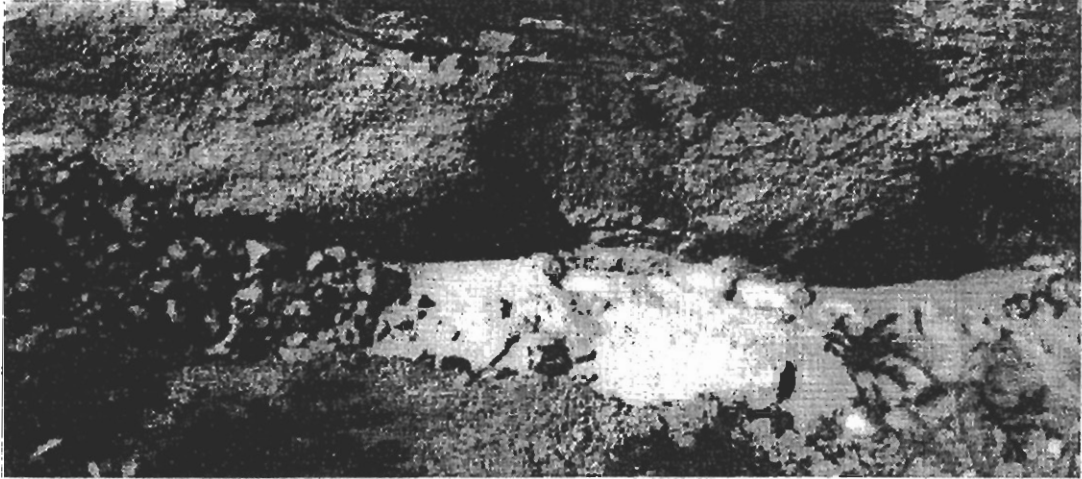
2.2.4 Grain flows

Subaqueous grain flows occur in the deep-sea when sand avalanches down the side of steep submarine canyons (Prothero and Schwab 1996). The cohesionless sediment moves down slopes under the pull of gravity and the flow is sustained by grain to grain collisions (Prothero and Schwab 1996). Plastic flow behaviour and laminar flow character. Deposition of grain-flow sediment occurs quickly and en masse by sudden freezing owing primarily to the reduction of slope angle (Boggs 1995).

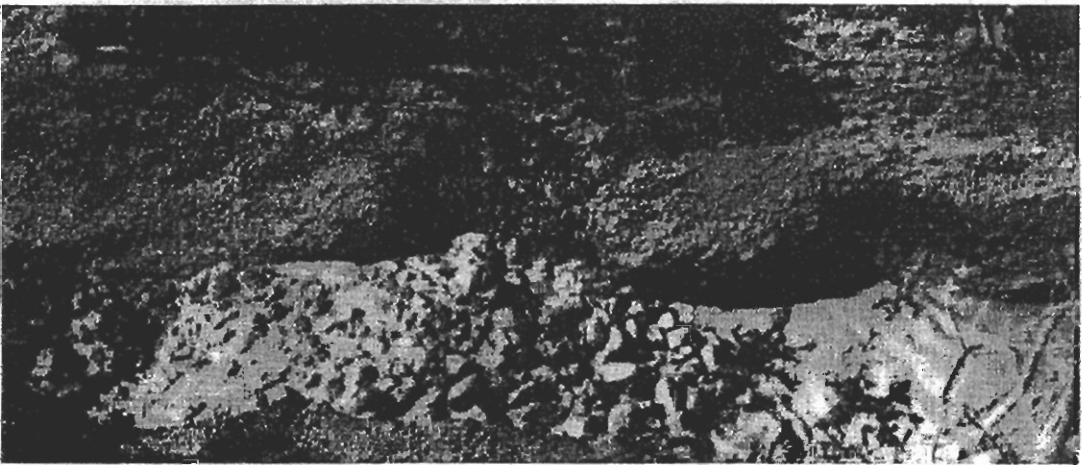
2.2.5 Debris flows

Debris flows are believed to occur in subaqueous environments as a result of mixing at the downslope ends of subaqueous slumps (Boggs 1995). They are plastic in rheology, one phase flow (solid) and the whole mass undergoes large and continuous deformation (Coussot and Meunier from Shanmugan 1997). They are laminar in state, supported by matrix strength, dispersive pressure and buoyancy and have high sediment concentrations (50-90%). Debris flows deposit sediment as the applied shear stress drops below the yield strength of the moving material. The flows freeze inward either en masse or from the corners (Einsele et al. 1991).

Figure 2: A Dynamic Debris Flow Sequence shows a debris flow moving along a canyon bottom near Utah. The steep bouldery front advances from left to right at about 1.3 m/s (from Prothero and Schwab 1996).



A



B

CHAPTER 3 Depositional Models

“The characteristics of a facies reflect as a rule only the mechanism of deposition (Mutti and Ricci Lucci 1972).”

Depositional models have been created from experimental studies and direct outcrop observation and description. All that can be inferred from the outcrop is the flow rheology and state of the sediment as it forms different patterns and structures during the final moments of its deposition, and the experimental studies show how these outcrop patterns and structures form. Experiments also show that transformation in flow rheology can take place during sediment transport through deep water, and that one flow can have both laminar and turbulent, plastic and fluidal flow rheologies. A flow however, can only have separate fluid rheologies at different moments in time and positions in space. This is believed to be a major constraint on the usefulness of some depositional models (E.g. high density models; Shanmugam 1997). I believe that it is not a problem because each grain of sediment is also deposited at different moments in time and positions in space.

Generalised depositional models have been described for all the sediment gravity flows.

3.1 Grain Flow Model

Grain flow deposits are massively bedded with little or no internal laminations and possible reverse grading at the base. Reverse grading is assumed to occur during grain flow as a result of smaller particles filtering down through larger particles while they are in the dispersed state (Boggs 1995).

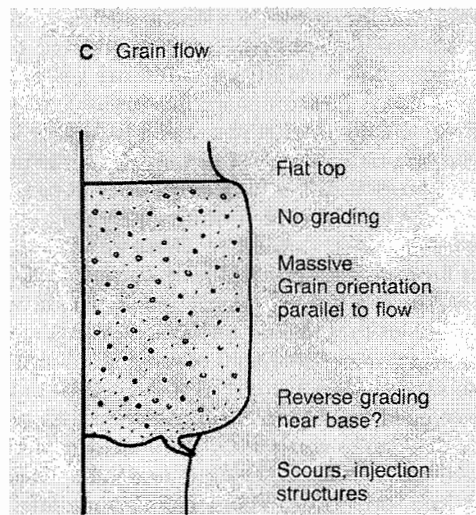
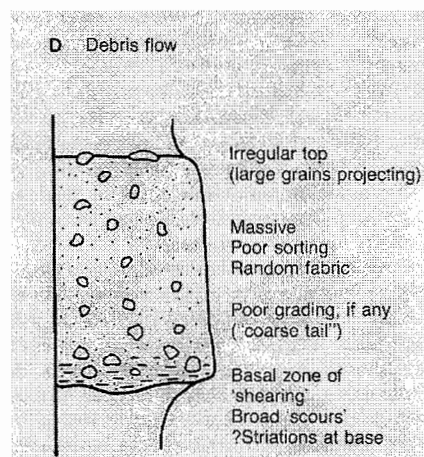


Figure 3: Grain Flow Depositional Model (from Prothero and Schwab 1996)

3.2 Debris Flow Model

Debris flow deposits consist of medium to fine grained matrix and a varying proportion of matrix-supported clasts (Einsele 1991). They are thick, poorly sorted units that lack internal layering and typically consist of chaotic mixtures of particles that may range in size from clay to boulders. They are generally poorly graded but grading may be present as reverse or normal grading (Boggs 1995). **Figure 4:** Debris Flow Depositional Model (from Prothero and Schwab 1996)



3.3 Liquefied Flow Model

Liquefied flow deposits are thick, poorly sorted and graded sand units especially characterised by fluid escape structures such as dish structures, pipes and sand volcanoes at the top (Boggs 1995).

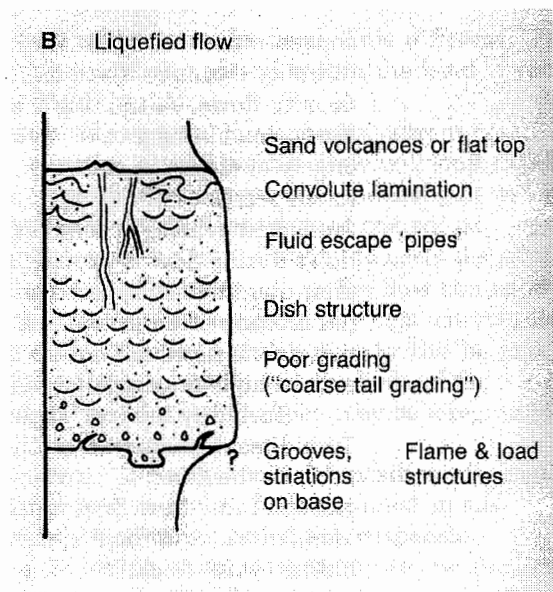


Figure 5: Liquefied Flow Depositional Model (from Boggs 1995).

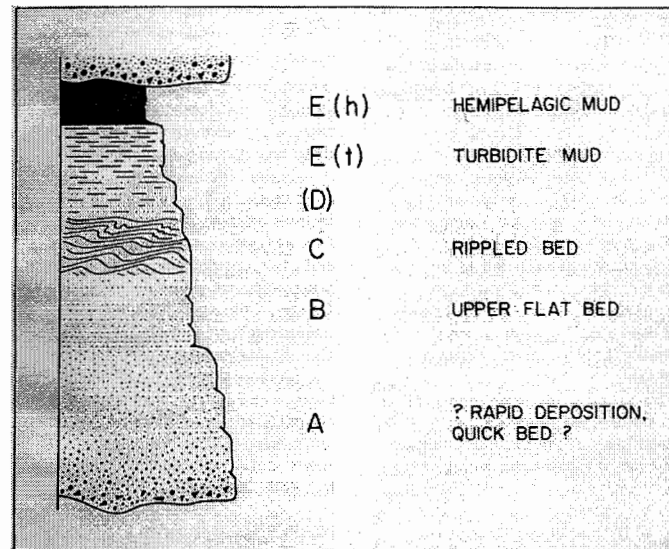
3.4 The Bouma sequence

The Bouma sequence was created as a model for a bed deposited by a short-lived waning turbidity current (Mutti and Ricci Lucchi 1972). The ideal sequence consists of five structural units that record the decline of the flow strength of the turbidity current with time and the progressive development of different sedimentary structures as the flow wanes (Boggs 1995).

The sequence is (Ta) a graded interval that grades upward into (Tb), an interval of plane-parallel laminae, (Tc) an interval of oblique and/or convolute laminae, (Td) upper interval of plane parallel laminae and finally (Te) a homogenous pelitic interval (Mutti and Ricci Lucchi 1972). The general method of using the model in fieldwork is

to assign each part of the bed being examined to either of the five sequences. The field notation is *Ta*, *Tb*, *Tc*, *Td* and *Te*.

Figure 6: The Bouma Sequence (from Walker 1984)



Bouma established the model from his study of 1061 beds in the Maritime Alps of southern France (Shanmugan 1997). In the type area less than 10% of the beds had the complete Bouma sequence (Walker 1965 from Shanmugan 1997). Most are top-absent, middle absent or base-absent (Walker 1965 from Shanmugan 1997). According to Shanmugan (1997), Bouma's turbidity current interpretation is valid only if the bed is normally graded.

3.5 High Density and Low Density Turbidites: The Lowe Model

The sedimentation waves of high density flows are subdivided by Lowe (1982) into a low density turbidity flow, a high density sandy flow and a high density gravelly flow. The grain populations of each of the flows are; 1) clay to medium grained sand; 2) coarse sand to small gravel and 3) pebble and cobble sized clasts. Lowe (1982) uses the notation R1-R3 for the individual structural divisions formed from the gravel wave of deposition, S1-S3 for the sandy wave flow deposit, and Bouma notation for the low density flow deposit (Lowe 1982).

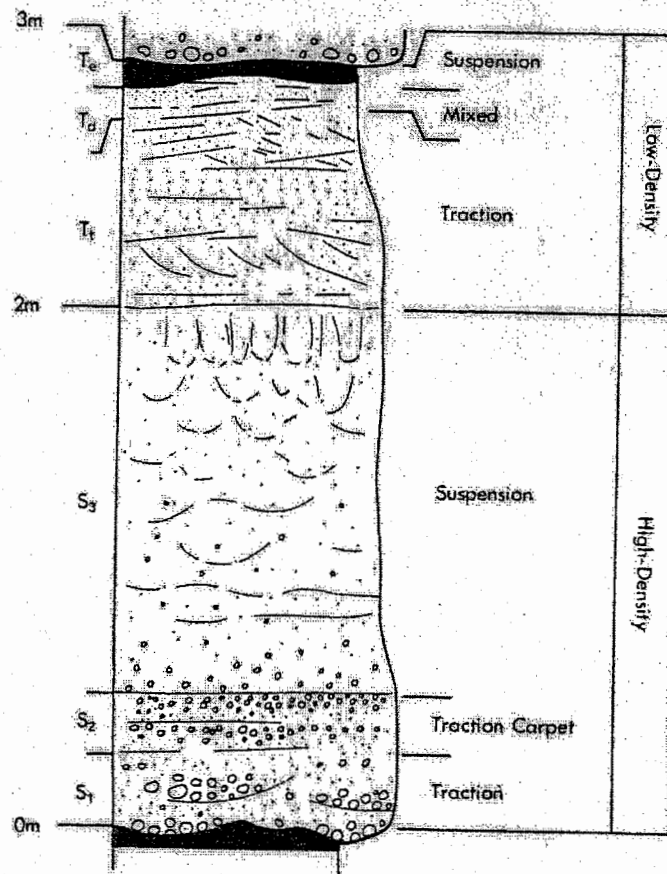
In a hypothetical case where all three grain populations are present in one flow, the gravelly population would be deposited by freezing of a traction carpet followed by direct suspension sedimentation (Lowe 1982). A traction carpet forms when a basal layer created through grain collisions is maintained by dispersive pressure (Lowe 1982). When turbulence is suppressed it becomes a traction carpet, and when forced by continued sediment fallout the traction carpet collapses and freezes instantaneously (Hiscott and Middleton 1979 from Lowe 1982). The deposit will be an inversely graded traction carpet layer at the base (R2) overlain by a normally graded suspension sedimentation unit (R3; Lowe 1982). This sequence coincides with Walkers (1975, 1977) inverse to normally graded conglomerate facies (Lowe 1982).

Once the gravel population is deposited the sandy flow begins to lose its turbulence and reworks the top of the gravel deposit. Sandy flow deposition begins with traction sedimentation and is followed by a traction carpet phase. Suspension sedimentation is the final stage of deposition from the high density turbidity current (Lowe 1982). The deposit will have flat laminations and oblique or cross-stratification at its base (S1) overlain by an inversely graded traction carpet (S2) and a graded sandstone top S3; Lowe 1982).

A low density turbidity current still remains, and as the flow wanes the sediment is deposited in the same way as the classic turbidite but without the Ta phase (Lowe 1982).

It is important to note that deposition of the sandy grains will occur independently of the gravel because the sand will completely bypass areas of gravel deposition (Lowe 1982).

Figure 7: Idealised High Density Turbidite Deposit (from Lowe 1982).



3.6 Turbidite Facies

Mutti and Ricci Lucchi (1972) introduced the concept of turbidite facies to simplify geologic understanding of deep-water sedimentation. They based the model on field observations from an ancient turbidite system in the northern Apennines and classified five main and two associated turbidite facies types. The depositional processes responsible for transport of each of the facies types is recognised as either grain flows or turbidity currents (Mutti and Ricci Lucchi 1972).

3.6.1 Facies A: Arenaceous-conglomeratic facies

This facies has a bed or strata thickness between one to two metres and is composed of medium to coarse grained sandstone with locally sparse pebbles and conglomerates. The sand/shale ratio is very high and grading is often limited to the coarser fraction of the bed. Grading can also be completely lacking but is usually associated with distinct contacts at the base and the top of the bed. At the base, structures such as large channels, small scour and fill features, tool marks and intraformational pelitic clasts are present. This facies is deposited by grain flow (Mutti and Ricci Lucchi 1972).

3.6.2 Facies B: Arenaceous facies

This is similar to Facies A but has a finer grain size (medium to fine sand), better sorting, thinner strata, more parallelism and areal continuity of stratification. It is more developed in pelitic intercalations, and the presence of broadly undulating thick and parallel laminae is the most diagnostic feature. Sedimentary structures include dish deformation structures, erosional channels, and pelitic inclusions. Grain flows are thought to be at least a part of the depositional process (Mutti and Ricci Lucchi 1972).

3.6.3 Facies C: Arenaceous-pelitic facies

This is the classic lithologic alternation that led to the original definition of turbidites (Mutti and Ricci Lucci 1972). The beds are 50 to 150 cm in thickness and distinguishable by their more regular and continuous nature. Sole markings are the most abundant structural feature in this facies. They are deposited by the classic turbidity current (Mutti and Ricci Lucchi 1972).

3.6.4 Facies D: Pelitic arenaceous facies

The beds of this facies are absolutely plane parallel and persist laterally for hundreds or thousands of metres. Each bed consists of a lithologic couplet as in Facies C but the pelitic part is of greater thickness and the arenaceous part is finer grained. The arenaceous part is entirely laminated and the sand/shale ratio ranges from 1:2 to 1:9 and the arenaceous thickness varies from 3-40 cm (Mutti and Ricci Lucci 1972).

3.6.5 Facies E: Pelitic-arenaceous facies 2.

This facies is different from facies D in having a higher sand-to-shale ratios (typically 1:1) and thinner, less regular, less continuous sandstone beds with frequent wedging and lensing. Facies E have coarser sandstone beds, more cross bedding and have ripples or dunes on the top. It was probably produced by liquefied grain flows and small currents (Prothero and Schwab 1996).

3.6.6 Associated Facies:

Facies F: Chaotic Facies

This facies is a vast category representing slumps, slides, olistostromes, mudflows or any other type of chaotic deposit (Prothero and Schwab 1996).

Facies G: Hemipelagic and pelagic Facies

These are usually massive but are vaguely stratified. They are generally grey, olive or bluish and often accompany turbidites both as intercalations between turbidite sequences and as distinct, laterally developed sedimentary bodies (Mutti and Ricci Lucchi 1972).

3.7 Modified Facies Model

Pickering et al. (1986; from Shanmugam 1988) presented a modified classification of deep-water facies for ancient deep-water facies composed of 40 distinct subfacies but the scheme is considered too complicated to apply within the field.

3.8 Shanmugam et al. (1995) Depositional Facies

The primary purpose of this facies scheme is to distinguish mass-transport deposits (i.e., slides, slumps and debris flows) from turbidity currents and bottom-current deposits (Shanmugam et al. 1995). This facies scheme has been recognised from 3600 m of core from basin floor fans in the North Sea (Shanmugam et al. 1995). The facies are based on lithological variations and physical sedimentary features (Shanmugam et al. 1995).

Facies 1 is a conglomerate and pebbly sand interpreted as deposits of gravelly slumps, slides and debris flows (Shanmugam et al. 1995). Facies 2 is a massive sand and the most widespread lithofacies (80-100% of all core examined), believed to be deposited by sandy slumps, slides and debris flows (Shanmugam et al. 1995). Facies 3 is a

contorted mudstone interpreted as deposition from muddy slumps, slides and debris flows (Shanmugam et al. 1995). Facies 4 is a rippled sand and silt interpreted as a product of bottom-current reworking (Shanmugam et al. 1995). Facies 5 is a normally graded sand and silt deposited by turbidity current and facies 6 is a laminated mudstone deposited by suspension sedimentation (Shanmugam et al. 1995).

Table 1: Shanmugam et al. Facies scheme for the North Sea (from Shanmugam et al. 1995)

Facies	Sedimentary Features*	Depositional Process
1	Gravel and pebbly sand (coarse to medium grained), amalgamated units, contorted bedding, floating clasts	Gravelly slump, slide, debris flow (mass transport)**
2	Fine- to medium-grained sand, amalgamated units, massive appearing, sharp top, basal (primary) glide planes, internal (secondary) glide planes, slump folds, contorted bedding, steep layers, shear zones, floating clasts, planar clast fabric, inclined dish structures, brecciated zones, clastic injections, synsedimentary faulting	Sandy slump, slide, debris flow (mass transport)**
3	Mudstone, sharp top, contorted bedding, steep layers, slump folds, shear zones, floating clasts, brecciated zones, planar clast fabric, clastic injections	Muddy slump, slide, debris flow (mass transport)**
4	Fine-grained sand and silt, current ripples, horizontal lamination, mud offshoots	Bottom-current reworking (traction transport)
5	Fine-grained sand and silt, sharp base, gradational top, normal size grading, Bouma divisions	Turbidity currents (suspension and traction transport)
6	Mudstone, horizontal lamination, shell fragments, bioturbation, glauconite	Pelagic and hemipelagic (suspension settling)

Hiscott et al. (1997) in a direct reply to Shanmugam et al. (1995) suggest that they have established the absence of turbidites in North Sea successions by defining the high-density turbidity currents out of existence. Shanmugam et al. (1995) achieve this by using a variety of features to indicate either debris flows or contour currents when they might equally be indicative of turbidity currents (Hiscott et al. 1997).

CHAPTER 4 Submarine Fan Models

General models for submarine fan sedimentation have been developed from outcrop observation of ancient systems and also from seismic and sidescan sonar of modern and ancient systems. This has produced different scales of observation because of the resolution differences between the three data sets. Some key terms such as lobe are being used to describe completely different features (Shanmugam and Moiola 1991).

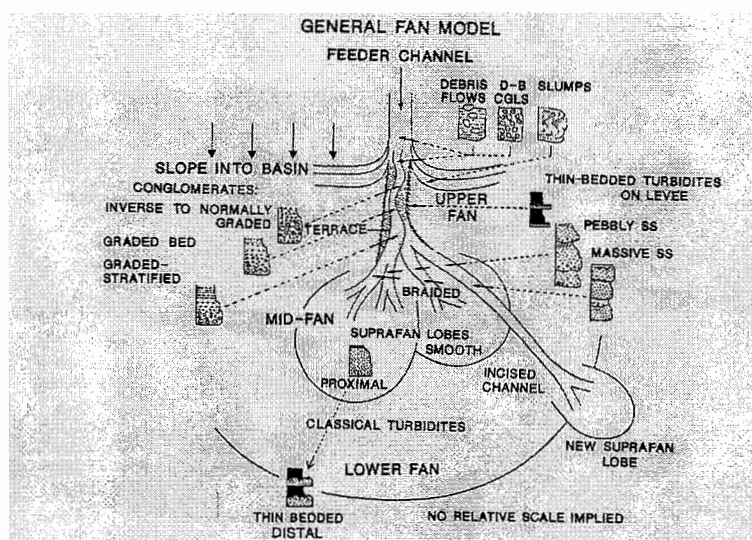
The shapes, size and sediment-fill of deep-sea fans are greatly variable due largely to their tectonic positioning and a tremendous complexity of depositional patterns exists from fan to fan, so any generalised model has its limitations (Normark et al. 1993). For these reasons the number of fan models created is almost the same as the number of fans studied (Normark et al. 1993).

4.1 The General Model

Mutti and Ricci Lucchi (1972), Normark (1978) and Walker (1978) developed similar models that divided the system into a slope, upper fan, middle fan, lower fan and basin plain. The slope has a canyon running through which branches off in the upper and middle fans into valleys and channels. Radiating out from the channels are lobes (Normark, 1970, 1978 from Shanmugam and Moila 1991).

Figure 8: The General Fan Model (Walker 1978 from Shanmugam and Moiola 1991)

SS-sandstone; D-B CGLS-debris flow.



4.2 Outcrop Data from Ancient Systems

Ancient submarine-fan environments are identified using characteristic associations of turbidite facies (Mutti and Ricci Lucci 1972). The characteristics of an association of turbidite facies express variations of depositional processes in time and space, and provide the most diagnostic information for environmental interpretation of ancient submarine fans (Mutti and Ricci Lucci 1972).

The slope and inner fan are composed of thick sequences of facies G pelagic muds that have been cut by slumps, olistostromes, and thick fan channels filled with facies A and B conglomerates and sandstones (Prothero and Schwab 1996). The middle fan is characterised by smaller lenticular channels filled with facies A and B, carved into planar laminated turbidites of facies C, D and E (Prothero and Schwab 1996). In the outer fan the channels disappear so the sequence is planar and composed of mainly facies C and D turbidites with great lateral continuity (Prothero and Schwab 1996). The deep-sea plain is thinner and finer grained and is dominated by fine-grained facies D turbidites alternating with facies G hemipelagites (Prothero and Schwab 1996).

The spatial configuration of the facies associations is shown in (figure 9 ;Mutti and Ricci Lucchi 1972 from Prothero and Schwab 1996). Mutti and Ricci Lucchi (1972) also described two types of succession, those in which the individual beds thicken upwards or thin upwards. Thickening upwards successions were compared with prograding delta lobes and thinning upward successions were compared with fills of submarine channels (Walker 1992).

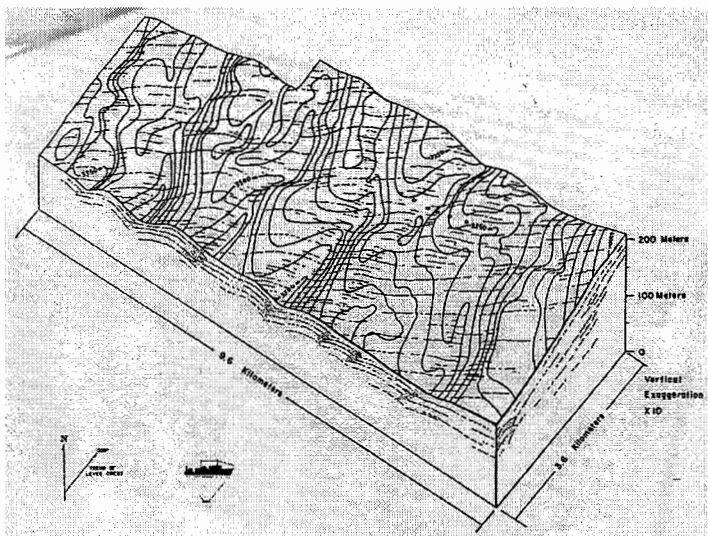
The facies association is an elegant and simple method of describing and interpreting ancient systems and is widely used by geologists. Powell and Baillie (1993) used the facies association to describe the Mathinna Group of northeastern Tasmania, as did Mackinnon and Howell (from Bouma et al. 1985) to describe the ancient Torlesse submarine fan in a subduction complex in New Zealand.

This fan model however is purely sedimentological and does not incorporate the effects of relative sea level fluctuations, changes in the grain size of sediment supplied and basinal tectonics (Walker 1992). Shanmugam et al. (1985) regards the use of this model as tentative because modern fans in many cases are large enough to contain entire ancient fan systems and it is difficult to believe that all submarine fans will develop identical subenvironments.

4.3 Shallow Penetration Geological and Geophysical Data from Modern Systems

This unique data enables the understanding of the morphology and map distribution of the systems. High resolution shallow penetration seismic data and side scan sonar yields a clear two dimensional and sometimes three dimensional view of the deep-water sand system (Figure 10; Normark et al. 1993). This gives an unparalleled picture of near surface submarine fan features (Normark et al. 1993). The shortcoming of this approach however is that the core data required for ground truthing is very short ($<10\text{m}$) and therefore the information may not necessarily apply to the more distant geological past (Normark et al. 1993).

Figure 10: Shallow Penetration and sidescan sonar derived perspective drawing with superposed bathymetric contours of sediment waves on the main western levee of the Monterey fan (from Normark et al. 1993).

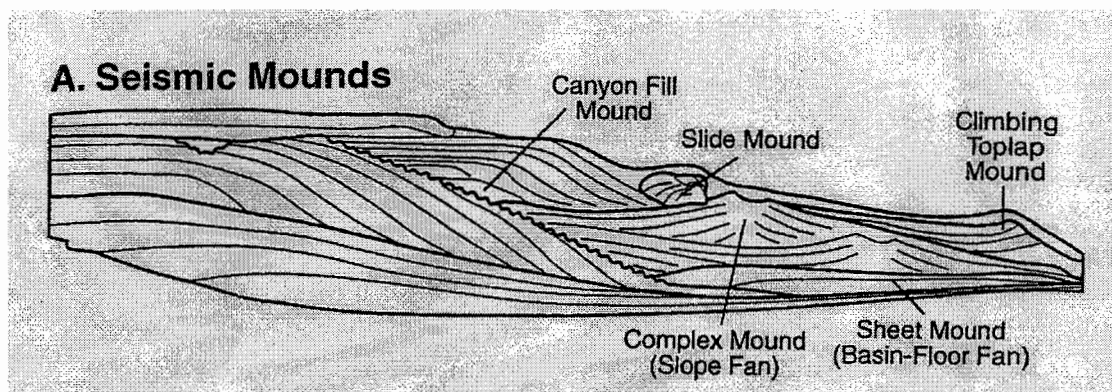


4.4 Deep Penetration Seismic Reflection Data

Multichannel seismic reflection data permit the study of ancient and modern fans that are buried beneath the strata (Normark et al. 1993). Seismic data emphasises the external geometry and the stratal patterns within the systems as inferred from reflection configurations (Shanmugam et al. 1988). Seismic reflection profile resolutions are typically restricted to a 10-25m vertical scale and therefore there is no definite seismic criteria to delineate mud-rich lobes from sand-rich lobes.

Sand-rich lobes form important hydrocarbon reservoirs in the North Sea, California and other areas and therefore this is an important restriction to note (Shanmugam and Muiola 1988). The profiles do however provide information regarding the lateral continuity of significant geologic continuities generally unavailable from scattered outcrops and therefore provide valuable insights regarding regional palaeogeographic setting and temporal relationships (Normark et al. 1993).

Figure 11: Seismic Reflection Profile showing stratal patterns and mounded forms within a depositional sequence of the conceptual sequence stratigraphical model (Shanmugam et al. 1988).



The characteristics of the seismic signals and their mutual relationships are categorised by Walker (1992) into four large scale facies associations common to modern fans. These are:

1. extensive channel-levee systems
2. Continuous, unchannelised, sheetlike deposits
2. mass-transport complexes
3. slumps and debris flows associated with levee failures.

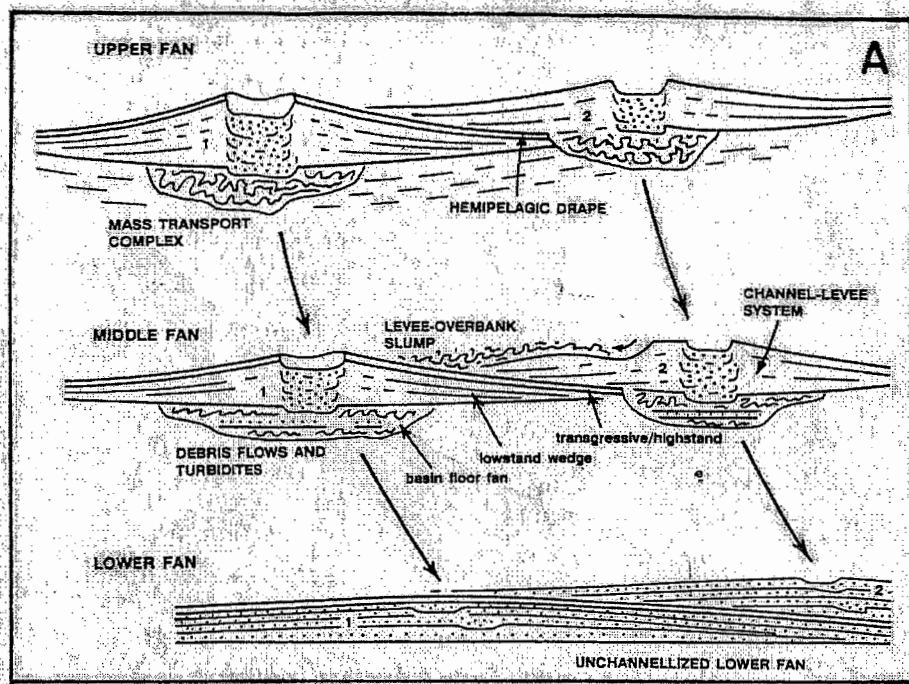


Figure 12: Preliminary fan model in which fan deposition begins with a Mass Transport Complex overlain by a channel-levee system (From Walker 1992)

4.5 Summary

Fan models based on or biased toward one or the other of these data bases will be weaker than fan models based on an integrated assessment. Seismic models should be refined using outcrop data and vice versa (Normark et al. 1993).

Local and regional tectonic setting, relative sea-level variations and their interactions should be carefully evaluated in future studies on a case by case basis in order to obtain a significant number of well-studied examples that may lead to the formulation of depositional models with predictive value (Normark et al. 1993).

CHAPTER 5 Conclusion

The variability in depositional processes, sediment fill and basin geometries that occurs between different deep water sand systems is tremendous, and for this reason alone all deposition and fan models should be subject to great scrutiny if they are used in the field. The depositional models are very powerful tools for identifying and interpreting the system. If the models however are used to describe the rocks, they carry with them an in-built interpretation that may not be appropriate. For example if you were to describe a bed using the *Ta* notation of the Bouma sequence then you have already interpreted the deposit as a turbidite when it is just as likely the deposit may have come from a debris flow.

Therefore I suggest that when fieldwork is carried out a premium should be placed on a pure description of the rocks without using a depositional model. Once the description has been done then it is time to compare this to the models and an interpretation may be arrived at. A pure descriptive undertaking that has been done correctly will never be wrong, but an interpretation of the description is somewhat arbitrary and may always be altered when new information about the system is discovered.

I agree with Shanmugams' (1997) assessment that the term turbidite system should not be used as a name for all deep-water sand systems, because the term turbidite clearly means a deposit from a turbidity current. It is misleading to call a system that is generally agreed by all workers to be a result of all four sediment gravity flow deposits by a name referring to only one of the gravity flow processes. Throughout this paper it was extremely difficult not to refer to the systems as turbidite systems because the term is so entrenched within the literature.

I disagree with Shanmugam et al. (1995) when they deny the existence of high-density turbidites as they have been experimentally defined and increasing the spectrum of flows is probably a good step. It is a positive step because it is obvious from the study of the literature that the exact processes involved in deep-sea sedimentation have not been completely constrained. Experimental studies although useful in simulating deep-sea sedimentation, cannot replicate the vast and still unknown complexity of depositional patterns involved. Further studies are required to increase knowledge of the possible spectrum of deposits.

References

- Boggs, S Jnr. 1995. Principles of Sedimentology and Stratigraphy. Second Edition. Prentice-Hall Inc.
- Bouma, A.H., Normark, W.R. and Barnes, N.E. (editors). 1985. Submarine Fans and Related Turbidite Systems. Springer-Verlag New York, Inc.
- Einsele, G., Ricken, W. and Seilacher, A. 1991. Cycles and Events in Stratigraphy. Springer-Verlag.
- Haines, P., 2000. "Lecture 12; Deep Sea Fans." KEA 338 Sedimentary Environments. University of Tasmania, School of Earth Sciences.
- Hiscott, R.N., Pickering, K.T., Bouma, A.H., Hand, B.M., Kneller, B.C., Postma, G., and Soh, S. 1997. "Discussion and Reply: Basin-Floor Fans in the North Sea: Sequence Stratigraphic Models vs. Sedimentary Facies: Discussion." AAPG Bulletin, V.81, No. 4 (April 1997), P. 622-655.
- Kneller, B. 1995. "Beyond the turbidite paradigm: physical models for deposition of turbidites and their implications for reservoir prediction." From Hartley, A.J. & Prosser, D.j. (eds), 1995, Characterisation of Deep Marine Clastic Systems, Geological Society Special Publication No. 94, pp. 31-49.
- Kneller, B.C., and Branney, M.J. 1995. "Sustained high-density turbidity currents and the deposition of thick massive sands." Sedimentology (1995) 42, p. 607-616.
- Lowe, D.R., 1982. "Sediment Gravity Flows: 2. Depositional Models with Special Reference to the Deposits of High-Density Turbidity Currents." Journal of Sedimentary Petrology, Vol. 52, No. 1, March 1982, p. 0279-0297.
- Mutti E. and Lucchi F. 1972. "Le torbiditi dell' Appennino settentrionale: Introduzione all' analisi di facies." Memoirie della Societa Geologica Italiana,

1972, p. 161-199. Translated by Nilsen, T.H 1978. *International Geology Review*, V. 20, No. 2.

Powell, C.McA., Baillie, P.W, Conaghan, P.J., and Turner, N.J. 1993 "The mid-Palaeozoic turbiditic Mathinna Group, northeast Tasmania." *Australian Journal of Earth Sciences* 40, 169-196.

Normark, W.R., Posamentier, H. and Mutti, E. 1993. "Turbidite Systems: State of the Art and future Directions." *Reviews of Geophysics*, 31, 2 / May 1993.

Prothero, D.R. and Schwab, F. 1996. *Sedimentary Geology: Introduction to Sedimentary Rocks and Stratigraphy*. W.H. Freeman and Company New York.

Shanmugam, G., Bloch, R.B, Mitchell, S.M., Beamish, G.W.J, Hodgkinson, R.J, Damuth, J.E., Straume, T., Syversten, S.E., and Shields, K.E., 1995. "Basin-Floor Fans in the North Sea: Sequence Stratigraphic Models vs. Sedimentary Facies." *AAPG Bulletin*, V.79, No. 4 (April 1995), p. 477-512.

Shanmugam, G. 1997. "The Bouma Sequence and the turbidite mindset." *Earth Science Reviews* 42 (1997) p. 201-229.

Shanmugam, G. and Moiola, R.J. 1988. "Submarine Fans: Characteristics, Models, Classification, and Reservoir Potential." *Earth Science Reviews*, 24 (1988) P. 383-428.

Shanmugam G. and Moiola, R.J. 1991. "Types of Submarine Fan Lobes: Models and Implications." *The American Association of Petroleum Geologists Bulletin*, V 75, No. 1 p. 156-179, 21.



Shanmugam G., Damuth, J.E. and Moiola, R.J. 1985. "Is the turbidite facies association scheme valid for interpreting ancient submarine fan environments?" *Geology*, v. 13, p. 234-237, April 1985.

Walker, R.G. 1967. "Turbidite Sedimentary Structures and their relationship to proximal and distal depositional environments." *Journal of Sedimentary Petrology*. Vol. 37, No.1, pp. 25-43. March 1967.

Walker, R.G. 1984. *Facies Models: Second Edition*. Geoscience Canada. Reprint Series 1.

Walker, R.G. and James, N.P. (eds) 1992: *Facies Models :response to sea-level change*. Geological Association of Canada.

[illegible]


 fine laminae, even finer grey/dark grey silt intervals
 & mud chert intervals → this repeats itself for 40m.
 little darkened mud bits in grey silt/sand.  small bands
 of coarser grained
 (brown) sandstone
 white-grey fine grained
 highly cleaved

x little darkened mud
 in grey silt/s
 x white grey fine grained
 highly cleaved

Small bands
of coarser grained
(brown) sandstone

657

1. 1998-1999

20

Page 2

مجلسه ۱۲۸

APPENDIX 3

Rock sample no.	UTAS catalogue no.
-----------------	--------------------

1 D.T	145614
2b.	145615
7 D.T	145616
13 D.T	145617
14 D.T	145618
20 D.T	145619
1(a) D.T	145620
2 D.T	145621.